UPC
Universitat Politècnica de Catalunya

Doctoral Thesis

A Multimode Solid-State Quantum Memory for Single Photons

Author:
Alessandro SERI

Supervisor:
Prof. Dr. Hugues DE RIEDMATTEN

Co-Supervisor:
Dr. Margherita MAZZERA

A thesis submitted in fulfilment of the requirements for the degree of Doctor of Philosophy

in the

QPSA - Quantum Photonics with Solids and Atoms *group,*
ICFO - The Institute of Photonic Sciences

May 28, 2019

A scientist in his laboratory is not only a technician:
he is also a child placed before natural phenomena
which impress him like a fairy tale.

Marie Sklodowska Curie

Abstract

Quantum memories (QMs) for light represent a fundamental ingredient for the development of a quantum internet. Among other applications, they are a building block for the distribution of entanglement on large scale, i.e. for the realization of a quantum repeater architecture.

Rare earth doped crystals (REDCs) are a promising candidate towards this goal. In my thesis I use a Pr^{3+}:Y_2SiO_5 crystal. The longest storage time and the highest retrieval efficiency for a solid-state memory measured so far, were demonstrated with this system (in the classical regime). However, the main advantages of solid-state platforms are their suitability for miniaturization and integration as well as their inhomogeneous broadening, which enables broadband storage and spectral multiplexing.

In this thesis we demonstrate an on-demand solid-state QM for real single photons. Moreover we study new platforms for integrated QM based on the same material. We employ the atomic frequency comb (AFC) technique, which is the most promising storage protocol in terms of temporal multiplexing up to now.

Until the start of my PhD there was still no demonstration of storage of a real quantum state of light with an on-demand readout in REDCs. We achieved this in the course of this thesis, measuring also for the first time (and only, at the time of writing) non-classical correlation between a single spin wave in a solid-state QM and a telecom photon.

After proving the suitability of Pr^{3+}:Y_2SiO_5 crystals for on-demand QMs, we demonstrated novel types of integrated optical memories based on the same system. We studied the spectroscopic and coherence properties of the ions in laser-written waveguides fabricated by fs-laser micromachining. These projects were developed in collaboration with Dr. R. Osellame and Dr. G. Corrielli at Politecnico di Milano, who fabricated the waveguides and analysed their guiding properties. In a first kind of waveguide, called type II, we performed the first storage with on-demand retrieval ever done in solid-state integrated optical memories (with classical light).

We continued analysing a so-called type I waveguide, in which the mode-size is comparable with the mode guided in a single-mode fiber at the same

wavelength. Here we showed storage of heralded single-photons for a pre-programmed time. The demonstrated storage time, 5.5 μs, is the longest quantum storage demonstrated in any integrated waveguide up to now.

Finally, we performed in the same waveguide storage of the whole spectrum of a frequency-multiplexed heralded photon, spanning a range of frequencies of about 4 GHz. The photon is naturally multiplexed due to the generation method used, namely cavity-enhanced SPDC. The possibility of storing such a broad spectrum comes from the intrinsic inhomogeneous broadening present in REDCs. Together with the 15 frequency modes constituting the multiplexed photon, 9 temporal modes were stored thanks to the intrinsic temporal multimodality of the AFC protocol.

The method used to fabricate our waveguides, fs-laser micromachining, is the only one to our knowledge that allows for direct 3D fabrication in the substrate. In the future, this will yield matrices of fiber-pigtailed waveguide-based QMs, thus enabling a high degree of spatial multiplexing, which nowadays is mostly exploited in atomic clouds, where temporal and spectral multiplexing are more difficult to achieve.

The crystal, the protocol and the waveguide fabrication technique employed in this thesis, represent all together a very promising system, opening the way for a future quantum repeater architecture based on scalable highly multiplexed QMs.

Resum

Les memòries quàntiques (MQs) per a la llum constitueixen un ingredient fonamental per al desenvolupament d'un Internet quàntic. Entre altres aplicacions, són un element bàsic per a la distribució de l'entrellaçament a llargues distancies, és a dir, per a la realització d'un repetidor quàntic.

Els cristalls dopats amb terres rares (REDC) són candidats prometedors cap a aquest objectiu. En la meva tesi uso el cristall Pr^{3+}:Y_2SiO_5. Amb aquest sistema (en el règim clàssic) es va demostrar el temps d' emmagatzematge més llarg i la major eficiència d'una memòria d'estat sòlid. No obstant això, els principals avantatges de les plataformes en estat sòlid són la possibilitat de miniaturització i integració, així com la ampliació inhomogènia dels seus perfils d'absorció, que permet emmagatzemar fotons amb banda ampla o multiplexats en freqüència. En aquesta tesi demostrem una MQ d'estat sòlid amb lectura on-demand per a fotons únics reals. A més, estudiem noves plataformes per a MQs integrades basades en el mateix material.

Utilitzem la tècnica de pinta de freqüència atòmica (AFC), que és el protocol d'emmagatzematge més prometedor per a multiplexació temporal fins ara.

Al començament del meu doctorat no hi havia cap demostració d' emmagatzematge d'un real estat quàntic amb una lectura on-demand del fotó en REDC. Ho hem aconseguit en el curs d'aquesta tesi, mesurant també per primera vegada (i única, en el moment d'escriure), una correlació no-clàssica entre una única ona de spin en una MQ d'estat sòlid i un fotó de telecomunicacions.

Després de demostrar la idoneïtat dels cristalls Pr^{3+}:Y_2SiO_5 com MQs, vam demostrar nous tipus de memòries òptiques integrades basades en el mateix sistema.

Vam estudiar les propietats espectroscòpiques i de coherència dels ions en guies d'ones escrites amb làser fabricades amb la tècnica del fs-làser micromachining. Aquests projectes van ser desenvolupats en col·laboració amb el Dr. R. Osellame i el Dr. G. Corrielli del Politècnic de Milà, que

van fabricar les guies d'ones i van analitzar les seves propietats orientadores. En un primer tipus de guia d'ona, anomenada tipus II, vam realitzar el primer emmagatzematge amb lectura on-demand mai realitzada en memòries òptiques integrades en estat sòlid (amb llum clàssica).

Després vam analitzar un altre tipus de guia d'ondes anomenada tipus I, en la qual la mida del mode és comparable amb el mode guiat en una fibra monomode a la mateixa longitud d'ona. Aquí vam mostrar l'emmagatzematge de fotons simples durant un temps preprogramat. El temps d'emmagatzematge demostrat, de 5.5 μs, és fins ara l' emmagatzematge quàntic més llarg demostrat en qualsevol guia d'ones integrada.

Finalment, es va realitzar en la mateixa guia l'emmagatzematge de tot l'espectre d'un bi-fotó multiplexat en freqüència, abastant un rang de freqüències de ~ 4 GHz. El fotó és multiplexat de forma natural gracies al mètode de generació utilitzat, és a dir, el SPDC millorat per cavitat. La possibilitat d'emmagatzemar un espectre tan ampli prové de l'ampliació intrínseca de l'absorció inhomogènia present en els REDC. Juntament amb els 15 modes de freqüència que constitueixen el fotó multiplexat, s'han emmagatzemat 9 modes temporals gràcies a la multimodalitat temporal intrínseca del protocol AFC.

El mètode utilitzat per fabricar les nostres guies d'ona, fs-làser micromachining, és l'únic que coneixem que permet directament fabricar en 3D en el substrat. En el futur, això donarà matrius de MQs basades en guies d'onades integrades con fibres, que permetran un alt grau de multiplexació espacial, que avui en dia s'explota sobretot en núvols atòmics, on el multiplexatge temporal i espectral és més difícil d'aconseguir.

El cristall, el protocol i la tècnica de fabricació de guies d'ona utilitzats en aquesta tesi, representen tots junts un sistema molt prometedor, obrint el camí per a una futura arquitectura de repetidors quàntics basada en MQs escalables i altament multimodales.

Acknowledgments

I want to thank Hugues and Margherita for their great supervision during these 'short' ~ 5 years, for answering my too-many questions, for explaining me once, twice, *trice*, ... *Nice* times the same things and for guiding me along all these projects. Thanks for the huge amount of corrections on reports/papers/thesis, for the fruitful and detailed discussions and explanations on the whiteboard and for being always available for any doubt. It was a great opportunity and pleasure to work with you.

At the beginning 4.5 years seemed to be an infinitely long time but I would have definitely continued to stay in the lab tranquillamently if UPC or Jelena would not kick me out (not your fault, Jelena)! This is only thanks to many great people that made/make my stay so guay!

Darío, the weirdest best/worst labmate ever! Thanks for destroying my self-estím... and for your enthusiasm, sincerity, determination and professionality, lab-singing, your strange questions and topics of discussion in the lab, for the tressette! I loved to work with you! Thanks to the other people from which I daily learned: Margherita again, also for the italian grammar, the *congiuntivi* that I definitely stopped to use again and for teaching me how not to approach professors; Master Andreas, with your miles of anegdota and 90s songs; Kutlu/er, I do not know how many times I disturbed you, asked you questions, used your lab-bed... uch ashell beshu kara many times; Ema, both for your too-clever-questions, for the pizza-footballs (scusa per continuare ad accostarti alla pizza, è piú forte di me) and for the beach! A superbig thanks to the whole QPSA amazing group, I apprendiated a lot from all of you and I also felt to work within a group of friends: Nicolas (I already miss your messages), Pau (gràcies també pel *resum* i les calçotades), Bernardo boluudooo, Auxi, *old-me* Mustafá, Chetan Jumanji, Estefáno Righeeti, Lukas, Georg, Chiara, Marco, Daniel, Eliza, Boris, Patrick! Thank you veryck... Much!

And to the *new-me* Jelena and Sam good luck, I am sure you will have a great time and amazing results (warning bad eye), continue to speak to the experiment as you perfectly learned!!! I should also thank Jelena for your constant help with english and for explaining me all those things you know about REDCs and Sam, thanks a bunch for the corrections of the

thesis and for the discussions on those super-pignols interesting details you find! Dai dai dai chicos!

I want to separately ringraziate my first officemate David and Fede for adopting me in their family when I arrived! Thanks for your naturality, warmness and enthusiasm! Siete bbelli!

Acknowledgements to Dr. R. Osellame and Dr. G. Corrielli for the samples and for the great collaboration. Thanks Giacomo for your always deeply scientifically super-long audio messages!

During the PhD there are days which seem infinitely long and problems that seem unsoluxionatable and unarreglatable... but in the corridor or caffettería there was always some friend to appoggiate me or to sfogate with: Marchetto, Nicola, Carloota, i guaiottoni, Alex, Nat, Lorella and a lot of others! Thank you and thanks to all the very important non-listed friends that made my Barcelona-time tanto great and kept my mental equilibrium kind of stable!

Finally I want to thank my former boss Prof. Gianni from Camerino, I would have never started this experience without your pressure and support; un grande grazie alla mia famiglia che mi ha sempre motivato e appoggiato prima e durante il dottorato and, last but most important, to Cate for your constant and necessary presence, motivation, support, help, love and positiveness!

Akheysh

List of publications

1. Giacomo Corrielli*, Alessandro Seri*, Margherita Mazzera, Roberto Osellame and Hugues de Riedmatten, *An Integrated Optical Memory based on Laser Written Waveguides*, Phys. Rev. Applied **5**, 054013 (2016) (Chapter 6).

2. Alessandro Seri, Andreas Lenhard, Daniel Rieländer, Mustafa Gündoğan, Patrick Ledingham, Margherita Mazzera and Hugues de Riedmatten, *Quantum Correlations between Single Telecom Photons and a Multimode On-Demand Solid-State Quantum Memory*, Phys. Rev. X **7**, 021028 (2017) (Chapter 5).

3. Alessandro Seri*, Giacomo Corrielli*, Dario Lago-Rivera, Andreas Lenhard, Hugues de Riedmatten, Roberto Osellame and Margherita Mazzera, *Laser-written integrated platform for quantum storage of heralded single photons*, Optica **5**, 934 (2018) (Chapter 7).

4. Alessandro Seri*, Dario Lago-Rivera*, Andreas Lenhard, Giacomo Corrielli, Roberto Osellame, Margherita Mazzera and Hugues de Riedmatten, *Quantum Storage of Frequency-Multiplexed Heralded Single Photons*, arXiv:1902.06657 (2019) (Chapter 8).

Publication not included in the thesis

5. Carlos Abellán and the BIG Bell Test Collaboration, *Challenging local realism with human choices*, Nature **557**, 212 (2018).

Abbreviations

QI	**Q**uantum **I**nformation
QC	**Q**uantum **C**ommunication
QR	**Q**uantum **R**epeater
QM	**Q**uantum **M**emory
REDC	**R**are-**E**arth **D**oped **C**rystal
REI	**R**are-**E**arth **I**on
OD	**O**ptical **D**epth
AFC	**A**tomic **F**requency **C**omb
SW	**S**pin **W**ave
CP	**C**ontrol **P**ulse
CSPDC	**C**avity-enhanced **S**pontaneous **P**arametric **D**own-**C**onversion
BTC	**B**ow-**T**ie **C**avity
DFG	**D**ifference **F**requency **G**eneration
PPLN	**P**eriodically-**P**oled **L**ithium **N**iobate
QFC	**Q**uantum **F**requency **C**onversion
DLCZ	**D**uan **L**ukin **C**irac **Z**oller
FSR	**F**ree **S**pectral **R**ange
FC	**F**ilter **C**rystal
FCav	**F**ilter **C**avity
TPE	**T**wo-pulse **P**hoton **E**cho
SPE	**S**timulated **P**hoton **E**cho
FWHM	**F**ull **W**idth at **H**alf **M**aximum
SNR	**S**ignal-to-**N**oise **R**atio
EOM	**E**lectro-**O**ptic **M**odulator
AOM	**A**cousto-**O**ptic **M**odulator
APD	**A**valanche **P**hoto**D**etector
SPD	**S**ingle **P**hoton **D**etector
CW	**C**ontinuous **W**ave
FLM	**F**emtosecond **L**aser **M**icromachining

Table of Contents

Chapter 1

Introduction

Fast communication on large scales is becoming a necessity in our society. Huge quantities of data are shared through the internet each day. Most of the smartphones are synchronised with the cloud and photos, music and files in general are sent continuously around the world using internet. We process daily bank transfers online to people and websites in the most different places around the world. Moreover many new realities are growing around the presence of internet, like *domotics* (automation of the *smart home* which can be controlled remotely), self-guided cars, *remote* jobs and many others. To sustain all of this, internet connections are getting faster and faster and have to deal with a continuously growing amount of data that people share and save online.

In this context cryptography plays an increasingly important role. The cryptographic algorithms used nowadays are based on a high mathematical complexity, meaning that they are computationally secure but theoretically solvable. In parallel with the traditional methods, possible solutions to this problem are given by quantum cryptography, a field of research that uses the laws of quantum mechanics to establish new cryptographic protocols provably more secure than the classical ones discussed before. Quantum laws find also other applications in the broader field of quantum information science, opening new possibilities, like teleportation of quantum information and dense coding, which would not be possible in the classical regime.

In this chapter I will explain the concepts at the basis of a branch of quantum information science, called quantum communication, and I will place the work of my thesis in the context of this research field.

1.1 Quantum Communication

Quantum information (QI) science is the field of research that studies the information present in a quantum system, how to encode this information and how to process it or share it by developing techniques based on quantum phenomena. The fundamental ingredients at the basis of QI science are:

• **Qubit -** It is the quantum equivalent of a classical bit. But while a bit can either be 0 or 1, a quantum bit (qubit) is associated to the state of a quantum object and, as a consequence, it can be 0, 1 or a superposition of both of them. For example, we can associate to 0 the quantum state of a single photon polarized horizontally (we will write it $|0\rangle$), and 1 to that of a single photon polarized vertically ($|1\rangle$). The state $|\psi\rangle$ of a photon generated in a superposition of them would be described by:

$$|\psi\rangle = \alpha|0\rangle + e^{i\phi}\beta|1\rangle$$

with $\alpha^2 + \beta^2 = 1$ and ϕ the phase between the horizontal and vertical components. When the qubit is measured along the same basis, it will randomly give as a result $|0\rangle$ or $|1\rangle$ with probabilities α^2 and β^2, respectively. In other words, the qubit will lay in a superposition state until the measurement. When we measure it we project it into a classical state.

• **Entanglement -** Two or more qubits can be in a superposition state in which they are mutually dependent (in mathematical terms, their state is not factorable). An example of entangled state for two qubits is:

$$|\psi\rangle = \alpha|0_A 0_B\rangle + e^{iAB}\beta|1_A 1_B\rangle,$$

A and B being the two quantum systems in which the qubits are encoded. Independently, both A and B can randomly be measured to be either $|0\rangle$ or $|1\rangle$, but once we measure one of them the other one is instantaneously projected into the same state, no matter the distance that separates them.

• **No-Cloning theorem -** In quantum mechanics a quantum state cannot be cloned, e.g. it is not possible to measure a qubit and to generate a second identical one. While this is a limitation for the transmission of quantum

information, the no-cloning theorem becomes a fundamental resource in quantum cryptography.

Quantum communication (QC) science [1] is a branch of QI that aims at distributing quantum resources between remote parties. In QC, usually, information is carried from one place to another encoded in degrees of freedom of photons (polarization, time-bin, spatial, optical-angular momentum, frequency, ...), our quantum carriers. This is mostly because of their high speed and of their low decoherence when they travel in free-space or through optical fibers at specific wavelengths.

In the last years a considerable effort is being made towards the creation of a large-scale quantum network [2, 3, 4, 5, 6, 7, 8]. This would be composed of quantum nodes, i.e. stations where qubits are generated, stored, processed, teleported, etc., and quantum channels, through which quantum information is sent from one node to another [9]. The ability to share entanglement between arbitrary nodes of this quantum network is an essential requirement for most QC protocols. This long term goal is the most direct application of the work I did during my PhD thesis.

Even if research is going both in the direction of free-space [4, 10, 11] and fiber-based QC, I will focus on the second scenario, a fiber-based quantum network. As optical fibers already provide the infrastructure for the classical internet, QC could be based on the same. The lowest achievable losses in the present fiber network are > 0.2 dB/km at about 1550 nm[1]. In a direct configuration, where two entangled photons are generated in an intermediate station and then sent through different fibers, entanglement has been demonstrated up to a maximal distance of 300 km [12]. After a few hundred km, in fact, losses become too high. For two points 1000 km apart, for example, even in the best conditions, the photon would experience an attenuation of 10^{-20}.

In the optical classical internet, this problem has been solved by measuring the optical signal and reamplifying it each few tens of km. This solution cannot be adopted in the quantum regime due to the no-cloning theorem.

[1] The lowest losses in fiber nowadays are about 0.16 dB/Km at about 1550 nm (Corning SMF-28 ULL optical fiber), but the fibers installed are old, thus exhibiting higher attenuation.

Nevertheless, a new architecture was introduced to solve this issue, the so-called quantum repeater.

1.2 Quantum Repeaters

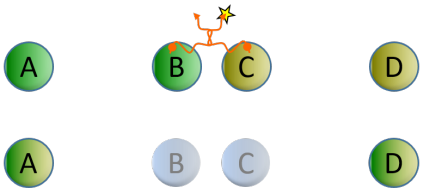

Figure 1.1: Sketch of the swapping process: A (C) is entangled with B (D); destroying the two pairs of entangled states by performing a Bell measurement between B and C (e.g. mixing them with a beam splitter), one can create an entangled state between A and D.

Most quantum repeaters (QR) are based on a quantum process called entanglement swapping [13] that works as follows: let's consider four quantum states, A, B, C and D, entangled in pairs (A with B and C with D, as represented with colours in fig. 1.1). After performing a Bell measurement (i.e. a measurement that projects a quantum state into a Bell state) between B and C, an entangled state would be generated between A and D. The Bell measurement can be performed by mixing the quantum states with a beam splitter, to erase the information on the origin of the measured photon/s. In this way, at the cost of two entangled states (the ones between A and B and between C and D), we have an heralded entanglement between two quantum states that never communicated directly between each other.

To understand how a QR would work, let's now consider two quantum nodes, A and Z, separated by a distance d (fig. 1.2(a)). These two could be entangled by sharing a pair of entangled photons, generated in a middle station. As discussed in the previous section though, the photons would experience an exponential loss along the channel and, for d higher than a few hundreds of km, the process would be extremely inefficient.

Let's now split the distance in many small intervals (fig. 1.2(b)) such that we can entangle the neighboring quantum nodes, A and B, C and D, ... and Y and Z, respectively. These pairs of neighboring nodes are called QR

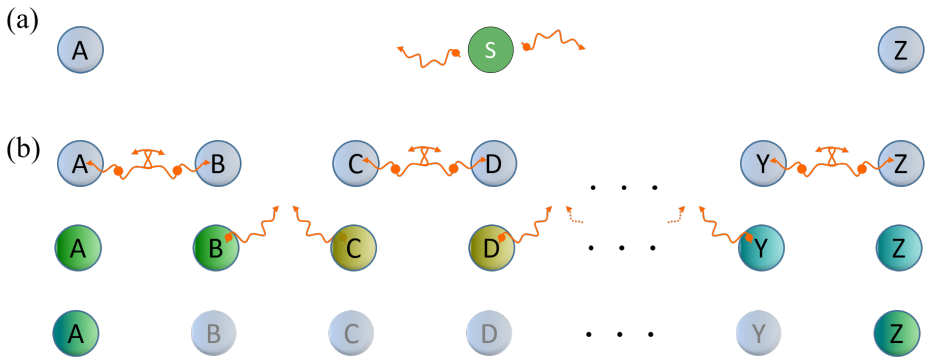

Figure 1.2: (a) Direct way to entangle two quantum nodes A and Z by sending two entangled photons (orange arrows) generated by a photon-pair source S. (b) Sketch of the quantum repeater scheme: Many intermediate nodes are added between A and Z (B, C, ..., Y). Each neighboring pair is entangled: A with B, C with D, ... Y with Z, as shown with colors. Entanglement swapping is used in all the intermediate stations (B, C, .., Y) to transfer the entanglement to A and Z.

links. We then perform entanglement swapping in the intermediate states (B and C, ..., X and Y). In this way, if all the Bell measurements succeed, we destroy the intermediate entangled states previously created and we herald the generation of an entangled state between A and Z.

If the success of each QR link is independent of the others, while the losses would still scale exponentially within the subintervals, they would only increase polynomially with the number of nodes, making it possible to share entanglement between any two quantum nodes over much longer distances than possible with direct transmission [2]. To make these links independent and also to synchronize them, as most of the times they are based on probabilistic processes, each node is provided with a quantum memory, i.e. a device able to store a quantum state with the possibility of retrieving it on-demand[2].

1.2.1 Quantum Memories

In this thesis I will focus on quantum memories (QMs) for quantum states of light, which are light-matter interfaces in which a photon is mapped into an atomic excitation and can be read out on demand. QMs are important

[2]Some new generation all-photonic QR schemes do not need QMs [3, 14].

for different QI applications [15, 16], for example they can be used to synchronize probabilistic events (e.g. in the QR scheme, or in linear-optical quantum computation), they are studied for quantum metrology and magnetometry and, in some cases, they allow interaction between qubits, i.e. they can be used as quantum gates [17]. The QR application is the one that received the highest attention so far.

The necessary figures of merit for a QM to succeed in a QR scenario are:

• **Efficiency -** The storage efficiency of a QM (in the case of storage of an external state of light) is given by the probability to absorb the state of light to be stored times the probability to read it out in the expected time window. The distribution rate of the entanglement scales exponentially with the QM efficiency [17].

• **Storage time -** The required storage time of the QM depends on the task it has to face. In the case of the QR, each link has to wait for all the others to succeed. The storage time, then, if the entangling mechanism of each link is probabilistic, has to be usually much longer than the time needed to cover the distance d between the first and the last node of the QR[3].

• **Multimodality (or multiplexing) -** In a single-mode scenario, when the nodes of a QR link become entangled, its QMs have to wait for the adjacent links to succeed in order to repeat the process. This would heavily decrease the rate of entanglement sharing. Moreover, in many QR schemes the phase between all of the entangled states has to be kept stable during the whole QR attempt. A possible, although not very scalable, solution would be to have many parallel QR infrastructures. Another one is to have multimode (or multiplexed) QMs, i.e. QMs able to simultaneously store many different quantum states and to retrieve them in a distinguishable way [19]. In this situation, for N modes stored, the QR protocol would be N times faster [19]. Moreover, the stability requirements for the QR protocol would be reduced [19]. In addition, for a high degree of multiplexing (apart from temporal multiplexing), a QR scheme could be built using QMs with a fixed storage time [18]. Nowadays, several approaches to

[3]This condition can be relaxed in some protocols, provided a high degree of multimodality to compensate for photon losses and finite storage efficiencies, i.e. provided that the success of each QR link per trial is almost deterministic [18].

multiplexing are being pursued, exploiting different degrees of freedom. For optical QMs the main ones are: **temporal** [20, 21, 22, 23, 24, 25, 26, 27, 28, 29, 30, 31]; **spatial**, that can involve different optical paths [32, 33, 34, 35] and/or different spatial distributions of the phases of the photons (along the same optical path), like orbital-angular momentum states [36, 37, 38, 31]; **frequency** [18, 39, 31, 40]; **polarization**, even if this degree of freedom is usually used for encoding qubits [41, 42, 43, 44]. In this thesis we will focus mostly on temporal, frequency and spatial multiplexing, even if, in our kind of system, all the mentioned degrees of freedom could be in principle achieved at the same time. In [31], for example, temporal, spatial (in the form of optical-angular momentum) and frequency multiplexing are demonstrated simultaneously in the same QM system that I used in my thesis, a Pr^{3+}:Y_2SiO_5 crystal.

• **Fidelity -** The fidelity, F, quantifies the similarity between the quantum state before the storage, ρ_{in}, and the one retrieved after the storage in a QM, ρ_{out}. We define it as $F = \mathrm{Tr}(\rho_{in}\,\rho_{out})$. If the state is encoded in a single photon, the maximum fidelity achievable with a measure-and-copy classical approach is 2/3 (it is (N+1)/(N+2) if it is encoded in N photons or N degrees of freedom of the same photon) [45]. This is defined as the classical limit. An higher value, then, would demonstrate that our QM works in the quantum regime. To preserve the non-local nature of the entanglement, F after the storage should be higher than 85.4% [17]. In the context of QMs, in general, we are interested in the *conditional* fidelity, i.e. the fidelity conditioned on the re-emission of the photon.

• **Robustness and integrability -** Implementing devices with guided-wave optics has several advantages, such as compactness, scalability, efficiency due to enhanced light-matter interaction (which increases with the confinement), and improved mechanical stability [46]. The possibility of interconnection with other integrated quantum devices, i.e. single photon sources, photonic circuits, and detectors, enables the implementation of complex integrated quantum architectures. In addition, the compatibility of these devices with fiber optics and with telecom photons would, possibly, lead to the interconnection between QMs and the current fiber networks [17]. To have correlations between a telecom photon and a state stored in a QM we could either use QMs working at telecom wavelength [47, 39], quantum frequency converters [48] or non-degenerate photon-pair sources

with one photon resonant with the QM and one at telecom wavelength [28] (further discussion in sec 1.2.2).

1.2.1.1 State of the art on quantum memories

To have efficient and reversible mapping of photons onto long lived atomic coherences it is necessary to have a strong interaction between light and matter. Unfortunately the interaction between a single photon and a single atom is in general very weak. Possible solutions to this problem include placing the atom into a high finesse cavity [49] or in a confined environment [50]. Another way relies on using a collection of atoms: having an ensemble of N atoms, in fact, enhances the light-matter interaction by a factor $\sqrt{N}$.

Even if the first quantum storage experiments have been demonstrated in atomic gases [51, 52, 53], there are many solid state systems which offer interesting perspectives for light storage, as color-vacancy centers in diamond [54, 55], phonons in diamond [56], quantum dots [57, 58] or rare earth doped crystals (REDCs), that will be the subject of this thesis. The advantages of working with solid-state systems are the compactness and simplicity of the optical system, the absence of atomic motion and the prospect of integrated devices. All these aspects make these kinds of systems good candidates for the development of large-scale quantum networks.

Many different storage protocols have been proposed. These techniques can be separated into two main groups, depending on whether they provide an emissive QM, in which the QM generates a quantum state of light correlated with a stored atomic excitation [2, 59, 29, 30], or an absorptive one, in which an external quantum state is absorbed, stored and retrieved on-demand.

Throughout my thesis I will focus only on absorptive QMs. In this context, very important results have been obtained with electromagnetically induced transparency (EIT) [60, 61], off-resonant Raman schemes [62], spectral-hole memory (SHoMe) [63] and photon-echo based techniques, such as gradient-echo memory (GEM) [64, 65], revival of silenced echo (ROSE) [66, 47], hybrid photon echo rephasing (HYPER) [67] and atomic frequency comb (AFC) [68]. Protocols like EIT rely on controlling the

transparency of the medium. Photon-echo protocols, otherwise, are based on a reversible absorption of the light in inhomogeneously broadened systems. Here the state of a photon is mapped onto a collective excitation of atoms such that, after a certain time, the atoms experience a collective rephasing, leading to a coherent re-emission of a photon-echo (this concept will be analyzed in detail in Chapter 3).

The highest storage efficiency demonstrated up to now is 92% for classical pulses [69] and $> 85\%$ for polarization-qubits encoded in real single photons [70] and have been both demonstrated in cold-atom experiments using EIT. In a similar system, the EIT protocol has been used to store classical light for more than 16 seconds [71]. The longest storage time measured so far, longer than 1 minute, was also demonstrated with classical pulses using EIT [72] but in a REDC, namely Pr^{3+}:Y_2SiO_5, the same kind of the one used along my thesis.

Remarkably high efficiencies (up to 87%) have been measured also using GEM, both in cold-atom experiments [73] and in warm vapours [74]. This protocol demonstrated very high efficiencies also for storage at the single photon level, namely 73% in cold atoms [73], and the highest efficiency ever measured in a solid-state memory, namely 69% with weak coherent states in a Pr^{3+}:Y_2SiO_5 REDC [65].

The SHoMe protocol was used to demonstrate the highest spin-wave storage efficiency so far measured in a solid-state system at the single photon level ($> 30\%$). This was realized by our group in a Pr^{3+}:Y_2SiO_5 REDC [63].

The first light-matter interface in solid state working at the single-photon level was demonstrated with the AFC protocol [75], the one used in this thesis. This realization was performed for only pre-programmed storage times in the excited state. In 2011, also, two groups measured light-matter entanglement between a telecom photon and a collective atomic excitation, using the same technique [22, 23]. The first solid-state quantum memory, at the single photon level with an on-demand readout, was demonstrated in our lab before the start of my PhD using the same protocol, storing time-bin qubits as a spin wave in a Pr^{3+}:Y_2SiO_5 REDC [24]. In my thesis, I continued demonstrating the first (and only, thus far) absorptive QM for real single photons in a REDC [28] (see Chapter 5). The best

efficiency shown with the AFC protocol until now is 56%, measured with classical light by embedding a low-absorptive crystal in an impedence-matched cavity [76]. This is still lower than the best storage efficiencies discussed, but has prospects for increase [77]. Nevertheless, the importance of the AFC relies mostly on its intrinsic temporal multimodality [68]. In fact, while the multimodality of EIT-based and Raman protocols scales as $\sqrt{\text{OD}}$[4], where OD is the optical depth of the transition, and in protocols like GEM it scales linearly with the OD [78], AFC-based protocols are the only ones in which the multimodality is independent from the OD of the system, depending only on the spectral bandwidth of the memory and on the storage time (a longer discussion can be found in sec. 3.3). Temporally-multimode storage for a pre-programmed time of 64 optical modes at the single-photon level was reported with the AFC protocol already in 2010 [20], followed by a demonstration with 1060 classical pulses [21] and, more recently, a storage with on-demand retrieval of 50 classical pulses for more than 0.5 ms [27]. Storage of time-bin qubits multiplexed over 26 frequency modes and with selective readout was demonstrated with weak coherent states [18] and, in another paper, storage of 6 frequency modes of an heralded single photon [39]. This protocol is mostly used in REDCs, and all the demonstrations I referred to are implemented in such systems.

While 51 orbital-angular momentum (OAM) modes and OAM-based entanglement have been stored in solid-state devices [38], spatial-path multiplexing has not be highly exploited in these systems yet. The most important demonstrations thus far, in fact, are performed in emissive quantum memories based on atomic clouds [33, 34], although this is a degree of freedom very suitable for solid-state integrated platforms.

Many quantum information schemes are dependent on a high ratio between the storage time and the duration of the stored pulse. This is related to the maximal multimode-storage capacity for temporally and/or spectrally multiplexed photons, while the photon duration dictates the maximal experimental rate. The related figure-of-merit is called time-bandwidth product (TBP) and it is the product between the storage time and the bandwidth. A TBP of ~ 5000 was demonstrated with efficiencies up to 30% using far off-resonant Raman transfer in warm atomic vapour [79]. This protocol may be particularly suitable for high-bandwidth on-demand single-photon

[4] A modified version of Raman was shown to scale linearly with the OD [78].

sources and for heralded multiphoton generation rates from parametric down-conversion sources. The AFC protocol also has proved high TBPs, 800 in [39] (extendable to 25000 in the same system), but this demonstration was for only pre-programmed storage times.

1.2.1.2 State of the art on integrated optical memories

Two approaches have been explored towards integrated rare-earth QMs so far. The first one is to integrate rare earths in already available waveguide systems [80, 81]. Quantum light storage has been performed in a Ti^{4+}:Tm^{3+}:$LiNbO_3$ waveguide fabricated by Ti^{4+} in-diffusion [23], where also an integrated processor has been implemented [82], and, more recently, in an Er^{3+}:Ti^{4+}:$LiNbO_3$ waveguide [83]. Another remarkable example is represented by weakly-doped erbium silica glass fibers [39], where spectral and temporal multiplexed quantum storage of heralded single photons at telecom wavelength was demonstrated. All these demonstrations were limited to the mapping of light field into optical atomic excitations. The drawback with $LiNbO_3$ matrix and the glass host is that they degrade the coherence properties of the rare-earth ions [23, 84] and they need to be cooled down to much lower temperatures [39, 85, 83].

The second approach consists in realizing waveguides in crystals already used for demonstrating bulk QM and suitable for long term storage of quantum information, e.g. Y_2SiO_5. Photonic crystal waveguides and cavities have been fabricated in Nd^{3+}:Y_2SiO_5, Nd^{3+}:YVO_4 and Er^{3+}:Y_2SiO_5, using focused ion beam milling [86, 87]. It was shown that the coherence properties of the rare-earth ions are preserved during the fabrication process. Moreover, in this system, storage of time-bin qubits was demonstrated at the single photon level. This fabrication technique is however challenging to extend to mm-long waveguides, which may be useful to achieve high storage and retrieval efficiencies. Also, the ions used so far possess only two-fold ground states, which restricts the storage of light to the excited state, strongly limiting the achievable storage times (more details in the next chapter).

In order to attain spin-wave storage, which enables long term storage and on demand read out, ions with a three-fold ground state, such as Eu^{3+} or Pr^{3+}, should be used [88, 89, 90, 24]. Apart from our realizations, only one

integration attempt has been done with Pr^{3+} ions so far, consisting of a TeO_2 slab waveguide deposited on a Pr^{3+}:Y_2SiO_5 crystal. The coherence properties of Pr^{3+} ions in this device have been measured to be consistent with those of bulk ions [91], which is promising for the implementation of integrated rare-earth based quantum devices. Nevertheless, in such a hybrid system the active ions are only evanescently coupled to the waveguide, and the effective power in the substrate is just 7.2% of the total power in the guided mode.

In this thesis I show the possibility to build a waveguide directly in the bulk of a Pr^{3+}:Y_2SiO_5 crystal with femtosecond laser micromachining (FLM) [92, 28], preserving optical and coherence properties of the material, strongly increasing the light-ions coupling and demonstrating the first spin-wave storage in waveguide and the longest storage times and efficiencies in integrated optical memories so far.

1.2.2 Possible implementation of a quantum repeater

There are many different proposals for the realization of a QR [15, 2, 19, 3, 93, 4, 5, 6]. Common to most of them is the ability to perform entanglement swapping, i.e. one photon from each QR link has to meet a photon from the neighboring one in an intermediate Bell-measurement station[5]. To enable low loss transmission in optical fibers, these photons should be in the telecom window, which, in most of the cases, is different from the operational wavelength of a QM.

The QR scheme proposed by Duan, Lukin, Cirac and Zoller, called DLCZ protocol [2], is based on emissive QMs, in which the QM generates entangled states between a single photons and a stored atomic excitation. This would be a perfect solution for multimode QMs operating at telecom wavelength, such as Erbium based REDCs [39]. However, the most promising results in terms of efficiencies and storage times up to date are demonstrated in QMs operating at wavelengths far from the telecom window. It becomes necessary, then, to use quantum frequency converters [48] which, by introducing new loss channels, further decrease the success probability

[5] This is not true for all-photonic QR architectures, in which the entanglement swapping is performed at the beginning of the protocol within the single-photon qubits present in the same node [3, 14]

of entanglement distribution. The proposal investigated in our laboratory, inspired by that described in [2], relies on multimode absorptive QMs (in which an external quantum state is absorbed, stored and retrieved on-demand) and entangled photon-pair sources, in which one of the photons is at the QM frequency and the other at telecom wavelength [19]. This solution gives greater flexibility on the choice of both the photon-pair source and the QM [15].

In our lab we use quantum sources of entangled photon pairs based on spontaneous parametric down-conversion (SPDC) and solid state quantum memories based on the atomic frequency comb technique [68] (details on the QM system will be given in Chapter 3).

The SPDC is a probabilistic process in which pairs of photons, the signal and the idler, are generated from a pump laser interacting with a non-linear crystal. The photon pair generated is a two-mode squeezed state. For low generation probability p, proportional to the pump laser, it can be written as:

$$\Psi \propto |0\rangle_s |0\rangle_i + p^{1/2} |1\rangle_s |1\rangle_i + O(p^{n/2}) \tag{1.1}$$

where s (i) refers to the signal (idler) photon. If we keep p low enough we can neglect the higher order contributions [94].

Let's consider now two different SPDC sources, S_1 and S_2, able to generate a state of the form of eq. 1.1, with $p \ll 1$. If the two sources are coherently excited, the pair is generated in a superposition of the two sources [19]. The generated idler fields are sent through a fiber and, then, mixed at a beam splitter (BS) which erases the information about the origin of the photon, provided that the two idler modes are indistinguishable. This

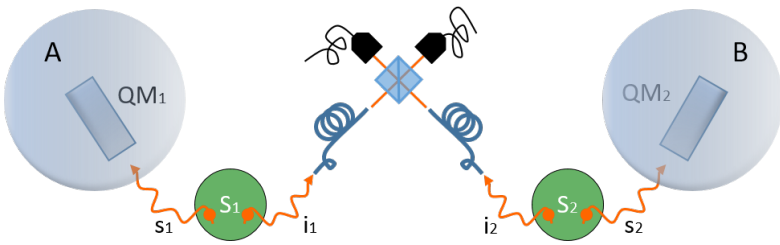

Figure 1.3: Sketch of half of the QR link that we want to realize.

detection would result in the entanglement swapping, i.e. it would herald

the generation of an entangled state between the two signal fields, s_1 and s_2. The entangled state would be of the form:

$$\Psi_{s_1,s_2} = \frac{1}{\sqrt{2}} \left(|1\rangle_1 |0\rangle_2 \pm e^{i\Delta\phi} |0\rangle_1 |1\rangle_2 \right), \tag{1.2}$$

where the $\pm$ sign depends on the output of the BS where the photon is detected and the phase $\Delta\phi = \phi_{i_1} - \phi_{i_2}$ refers to the phase difference acquired by i_1 and i_2 before they arrive to the BS. In each quantum node, A and B, we map the two signals in two different quantum memories, QM_1 and QM_2. Each detection click after the BS, then, heralds the generation of an entangled state between QM_1 and QM_2, i.e. between A and B.

The device shown in fig. 1.3 is half of a QR link [6] [2].

1.2.2.1 State of the art on quantum repeaters

The first important results towards the QR architecture came after the DLCZ proposal [2]. In 2005, a first realization demonstrated an heralded entanglement between two cesium atomic ensembles $\sim 3\,\text{m}$ apart [95]. In the same lab, in 2007, the full QR link was demonstrated, with two pairs of emissive QMs, one pair per node, again $\sim 3\,\text{m}$ apart [96]. A pair of QMs per node, in fact, is required in order to reduce the scaling of the vacuum component per swapping (i.e. per QR link) [15]. The vacuum component can be reduced even further combining the DLCZ and the Briegel, Dur, Cirac and Zoller (BDCZ) [97] protocol. In this case only two QMs are required, but it is necessary to measure two detections in the Bell-measurement stage. This was demonstrated using cold atomic clouds of ^{87}Rb, separated by 300 m of fibers [98][7].

In more recent years a QR link has been demonstrated even in solid state. The two most important results, shown using nitrogen-vacancy (NV) centers, are the demonstration of entanglement between two electron spins placed 1.3 km apart (the best result in terms of nodes-distance for QR

[6] In the DLCZ proposal, each node of a QR link is composed of two DLCZ-QMs [2]. This reduces the vacuum component increase per swapping operation [15]. In our case, each node would be composed of two QMs and two photon-pair sources.

[7] In this realization, with respect to the DLCZ one, there is no need of phase stabilization of the travelling photons and the vacuum component can be highly reduced. The drawbacks are the need of on-demand sources and the lower rates achievable [15].

links nowadays) [99] and, very recently, the demonstration of deterministic entanglement shared between two NV centers 2 m apart [5].

The main limitation to the distance reached in all these realizations is given by the wavelength of the heralding photons traveling through the fibers, which is not in the telecom window. For this reason, quantum frequency converters (QFCs) from the QM wavelength to telecom have been developed for different platforms: for single photons generated by NV centers [100]; for trapped ions, where, as a result, light-matter entanglement could be demonstrated between an emissive QM and a photon detected after 50 km of fiber [6]; for cold atomic ensembles [101, 48, 102]. In the last paper, published during the writing of this thesis, two QMs separated by up to 50 km of optical fiber have been entangled [102]; the heralding photons generated in the two quantum nodes are converted to telecom using QFCs and, then, are sent to a detection station located in a different place, through 11 km long fibers.

A QR link has not been realized with rare-earth ions yet. Nevertheless, since the AFC protocol proposal, many building blocks have been demonstrated towards this goal. In 2011, entanglement between a telecom photon and a collective atomic excitation has been measured by two different groups [22, 23]. One year afterwards, heralded entanglement between two centimeter-spaced REDCs was demonstrated [103], although the technique used cannot be extended to long distances. Among other important results, the state of a telecom photon was teleported to an AFC excitation [104] and a 3D photonic entangled in the OAM degree of freedom was stored [38]. The main limitation of all these demonstrations is the fact that storage has been performed only in the excited state of the ions (limited storage time) and only for a pre-programmed storage time. The first (and so far only) demonstration of correlations between a telecom photon and a single solid-state spin wave [28] is reported in this thesis in Chapter 5. The demonstrated storage time, limited to $\sim 30\,\mu$s, was still too short to be used in a real QR link demonstration, but it could be increased in the same system up to the minute regime [72]. Very important results have been demonstrated very recently also for emissive QMs based on REDCs. In particular, entanglement between a quantum state of light and a spin-wave has been demonstrated with the rephased amplified spontaneous emission (RASE) protocol [59]. Moreover, the DLCZ scheme has

been extended to solid-state memories [29, 30] demonstrating non-classical correlations up to the ms regime [30] and entanglement between a photon and a spin wave, allowing the violation of a Bell inequality [105].

1.3 State of the art in our lab

In our lab, before the start of my PhD, quantum storage of polarization qubit in the excited state [41] was demonstrated with weak coherent states using the AFC scheme. An ultra-narrowband source of spectrally-multiplexed photon pairs had already been developed, with one photon of the pair matching the operating wavelength of Pr^{3+}:Y_2SiO_5 [106] and the other at telecom wavelength. Then, storage of heralded single photons in the excited state [107] was demonstrated. The best storage time achieved for AFC storage of single photons was 4.5 μs with an efficiency comparable to 1%. This efficiency was increased to about 15% for the same storage time and we could demonstrate AFC storage up to 12 μs (measured with the same photon-pair source, the results are reported in Chapter 5).

Spin-wave storage of weak coherent states with less than one photon per pulse [24] had been shown using the same crystal demonstrating the first quantum memory for time-bin qubits in solid state. The average efficiency was about 6% at 5 μs of pre-programmed storage time in the AFC and 3% after the spin-wave storage (total storage time of 13 μs). We reached a slightly higher SW efficiency with heralded single photons and we could demonstrate a SW-QM with real quantum states of light. This will be the subject of Chapter 5.

1.4 Photon statistics analysis

In the QR link realization reported in sec. 1.2.2, we described the photon-pair source we want to use. We will analyze the generated photon pairs, the signal (s) and the idler (i) photons, by means of the second-order cross-correlation function, $g^{(2)}_{s,i}$, the unconditional autocorrelation function, $g^{(2)}_{s,s}$ ($g^{(2)}_{i,i}$), and the heralded autocorrelation function, $g^{(2)}_{i:s,s}$. Part of this section has been taken from [108, 109].

1.4.1 Second-order cross-correlation function, $g^{(2)}_{s,i}$

The second-order cross-correlation function, $g^{(2)}_{s,i}$, is a measure of the correlations between two photons, the signal (s) and the idler (i) photon. It can be expressed as:

$$g^{(2)}_{s,i}(\tau) = \frac{\langle E^{\dagger}_s(t) E^{\dagger}_i(t+\tau) E_i(t+\tau) E_s(t) \rangle}{\langle E^{\dagger}_i(t+\tau) E_i(t+\tau) \rangle \langle E^{\dagger}_s(t) E_s(t) \rangle},$$

where $E^{\dagger}_x$ (E_x) is the creation (annihilation) operator of the electric field of a photon x. This expression can be written as:

$$g^{(2)}_{s,i} = \frac{P_{s,i}}{P_s \cdot P_i}, \tag{1.3}$$

where $P_{s,i}$ is the probability to detect a coincidence between idler and signal photons, while P_i and P_s are the uncorrelated probabilities to detect each photon [110].

To get an intuition, if the signal and the idler photons are generated in pairs, each time that we measure one of them the probability to detect the other photon at the same time should be very high. On the other hand, as we work in a condition in which the generation probability of photons p is very low (see eq. 1.1), both P_s and P_i will be low. We expect then the $g^{(2)}_{s,i}$ at time 0 (0-delay between the two photons detected) to be much higher than 1. The lower p, the higher we expect the $g^{(2)}_{s,i}$ to be: namely, for an ideal two-mode squeezed state, $g^{(2)}_{s,i} = 1 + 1/p$ [111].

In our experiments we will not give the value of $g^{(2)}_{s,i}$ at 0 delay, but we will measure it in a limited time window. This lowers the $g^{(2)}_{s,i}$ but avoids the need to make any extra assumption, e.g. to fit the correlation function. In this way the value can be directly calculated from the raw measured data.

The $g^{(2)}_{s,i}$ can be used as a figure of merit to assess the compatibility with the classical theory, but, in order to do that, we have to define also the autocorrelation function $g^{(2)}_{x,x}$.

1.4.2 Unconditional autocorrelation function, $g^{(2)}_{x,x}$

The autocorrelation function of a photon x, $g^{(2)}_{x,x}$, measures the self-correlation of that photon. This quantity is measured by splitting the photon that we want to analyse with a BS, in the so-called Hanburry-Brown and Twiss configuration [112]. The coincidences between the detections measured at the two output ports of the BS have to be studied unconditionally on the detection of the other photon of the pair (in case of a photon-pair source).

We now can make a distinction depending on the outcome of such a measurement. We consider three different possibilities: bunched light ($g^{(2)}_{x,x}(0) > 1$), coherent light ($g^{(2)}_{x,x}(0) = 1$) and anti-bunched light ($g^{(2)}_{x,x}(0) < 1$) [8]. The anti-bunching is the only effect that cannot be explained in a classical vision, so that, measuring $g^{(2)}_{x,x}(0) < 1$, already tells that the light we are measuring is a quantum state of light.

Each of the photons generated by an SPDC source is a thermal state and follows the bunched-light statistics. For an ideal thermal state, $g^{(2)}_{x,x}(0) = 2$ [94]. For a multimode thermal state, x_{N}, composed of N modes, we expect a $g^{(2)}_{x_{\mathrm{N}},x_{\mathrm{N}}}(0) = 1 + 1/\mathrm{N}$ [114]. When noise is added to the system, the autocorrelation value decreases (as the noise statistics is random, i.e. with autocorrelation value of 1). Moreover, as mentioned for the $g^{(2)}_{s,i}$, we will not extract the autocorrelation value at 0-delay, we will measure it in a time window, thus decreasing its value even more towards the value of 1.

1.4.3 R-parameter and quantum correlations

The unconditional autocorrelation and the second-order cross-correlation functions together can be used as a measure of non-classical correlations. In fact, one possible way to assess the nature of the correlation is by verifying the so called Cauchy-Schwarz inequality [110]. Let's consider a pair of photons, s and i. The measured correlation between the two photons is quantum if:

$$g^{(2)}_{s,i} > \sqrt{g^{(2)}_{s,s}\, g^{(2)}_{i,i}}. \tag{1.4}$$

[8] The correct definition is $g^{(2)}_{x,x}(0) > g^{(2)}_{x,x}(\tau)$ for bunched light, $g^{(2)}_{x,x}(0) = g^{(2)}_{x,x}(\tau)$ for coherent light and $g^{(2)}_{x,x}(0) < g^{(2)}_{x,x}(\tau)$ anti-bunched light [113]. In our case, for $\tau \gg \tau_C$, with τ_C the coherence time of photon x, we assume to measure only uncorrelated coincidences, i.e. that $g^{(2)}_{x,x}(\tau) = 1$ [108].

To prove quantum correlations we define the Cauchy-Schwarz parameter [110]:

$$R = \frac{\left(g^{(2)}_{s,i}\right)^2}{g^{(2)}_{s,s} \cdot g^{(2)}_{i,i}}. \tag{1.5}$$

This value is expected to be lower than 1 for classical fields. A value higher than 1 demonstrates non-classical correlations between s and i.

1.4.4 Heralded autocorrelation function, $g^{(2)}_{y:x,x}$

A last figure of merit, for a photon-pair source, is the heralded autocorrelation, $g^{(2)}_{y:x,x}$, i.e. the autocorrelation function of the photon x, heralded by the detection of its twin photon y. Let's consider again a photon pair with a state as the one of eq. 1.1 and let's focus on the case in which $g^{(2)}_{i:s,s}$ is measured, i.e. the autocorrelation function of the signal photon heralded on the detection of an idler photon. In the low generation probability regime ($p \ll 1$), a detection click on the idler arm would herald with high probability the presence of a single photon s. In this case, the measured $g^{(2)}_{i:s,s}(0)$ will approach the value of 0, as no coincidences will be measured between the two outputs of the BS. For higher values of p, when multi-photon generation becomes more probable, the $g^{(2)}_{i:s,s}(0)$-value grows. It can be demonstrated [113] that:

- if $g^{(2)}_{i:s,s}(0) < 1$, s is a quantum state;
- if $g^{(2)}_{i:s,s}(0) < 0.5$, s is a single photon.

1.5 Summary of the thesis

The memory that I worked on during my PhD thesis is a solid-state device based on Pr^{3+} ions, namely a Pr^{3+}:Y_2SiO_5 crystal. In the next chapter, Chapter 2, I will introduce the properties of rare-earth ions and rare-earth doped crystals, focusing mostly on Pr^{3+}:Y_2SiO_5.

Chapter 3 will be focused on light-matter interactions: after a first theoretical overview, I will explain the optical techniques that we use along the thesis and, finally, the storage protocol used, the atomic frequency comb.

The technical details about the setup and the experimental sequences used to implement the protocols are described in Chapter 4.

In Chapter 5 I report on the first solid-state spin-wave storage of telecom-heralded quantum states of light [28], where we demonstrated half a node of a QR link [28] (following the scheme described in sec 1.2.2).

In 2015, we started a collaboration with Dr. Roberto Osellame and Dr. Giacomo Corrielli of Politecnico di Milano with the goal of demonstrating integrated quantum memories fabricated with a technique called fs-laser micromachining [115]. We analysed two fundamentally different kinds of waveguide: type II waveguides, described in Chapter 6 and type I waveguides, described in Chapter 7. In type II waveguides we demonstrated the first storage with on-demand readout in an integrated solid-state device [92] (with classical optical pulses). In the type I waveguide we demonstrated storage for pre-programmed time of heralded single photons [116].

The photon pairs generated by our photon-pair source are intrinsically multimode in frequency. In Chapter 8, we proved that our memory, besides the temporal multiplexing capability shown in Chapter 5, can store the whole spectrum of the frequency multiplexed photon [40].

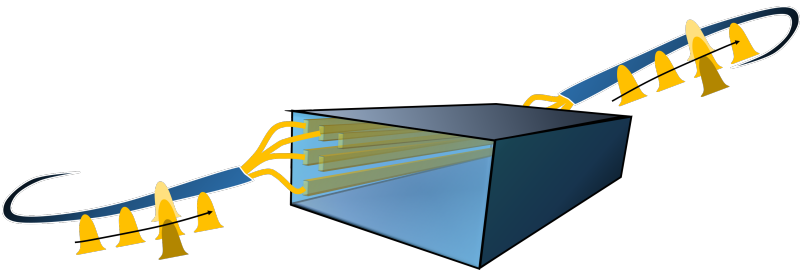

Figure 1.4: Sketch of a possible memory with spatial (waveguide matrix), temporal (4 different temporal modes) and frequency (three different colors in the third temporal mode) multiplexing.

Finally, I will conclude (Chapter 9) summarizing the main results achieved during my PhD and giving an outlook towards the realization of a highly multiplexed quantum memory based on Pr^{3+}:Y_2SiO_5.

Chapter 2

Rare-earth doped crystals

Our quantum memory is based on a crystal doped with a rare-earth ion (REI) called praseodymium (Pr^{3+}). In this chapter I will introduce the properties of these ions when doped into a solid-state matrix. This chapter is inspired by some books and theses [117, 118, 119].

2.1 Rare-Earth Ions

In the periodic table, fig. 2.1, the elements are divided in groups according to the occupation number of atomic orbitals. On the left (plus helium, He) there are the elements in which the s orbital is getting filled (yellow), on the right the p orbital (blue) and in the center the d orbital (green). The elements in which the electrons occupy the f orbitals (purple in the figure) are usually separated from the rest of the elements and written below. The first row of elements is usually called lanthanide series, named after the first element of the series (lanthanum). These elements have very similar chemical properties to scandium (Sc) and yttrium (Y) and, together with them, they are referred to as rare-earth elements. In the lanthanide series, the 4f shell is partially filled. Before filling the 4f orbital the electrons occupy the 5s and the 5p (the rare-earth atoms have even 2 electrons in the 6s orbital and sometimes one in the 5d, but these are lost in the trivalent ion [120]). As the fully filled 5s and 5p orbitals have bigger average radius than the 4f (see inset in fig. 2.1), the electrons in the 4f shell are provided with an electrical shielding from the outer environment. It is thanks to this chemical property that the rare-earth ions (REIs), after being doped in a crystal, show very sharp 4f-4f transitions.

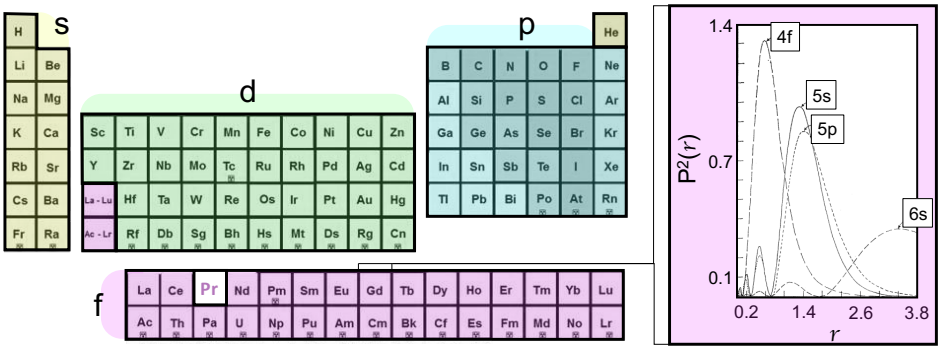

Figure 2.1: Periodic table of elements, with a color code identifying the orbital being occupied by the electrons. Inset: The radial charge density, $P^2(r)$ as a function of radius r, for the 4f, 5s, 5p, 6s orbitals of Gd^+ from ref. [121].

When we consider the magnetic properties of ions, we can divide them in two main groups: Kramers ions, with an odd number of 4f electrons, and non-Kramers ions, with an even number of them. This distinction is very important due to the strong correlations between pairs of electrons in the unfilled shells. Kramers REIs, for example, due to their unpaired electron, have stronger magnetic moments, which can induce decoherence via magnetic dipole-dipole interactions.

Among the REIs, we will be working with Praseodymium, Pr^{3+}. It is a non-Kramers ion, with 2 electrons in the 4f shell. In our experiments, Pr^{3+} ions are doped in a Y_2SiO_5 host. In the next section I will focus on the properties of the REI doped into crystals.

2.2 Rare-earth doped crystals

The electronic state of a REI when doped into a crystal is governed by the Hamiltonian:

$$H_{TOT} = H_0 + H_C + H_{SO} + H_{CF} + H_{HF} + H_Z \tag{2.1}$$

As discussed previously, REIs do not interact strongly with the environment. Therefore, to understand their level structure, we can start from the free ion case (first three terms of eq. 2.1) . Here, the degenerate levels are defined by the kinetic and potential energy of the electrons moving around

the nucleus, related to H_0. The first splitting happens due to Coulomb interaction between the 4f electrons (H_C), which separates ground and excited levels. These levels are named after their quantum numbers L and S (the total orbital angular momentum and the total spin angular momentum, respectively) as ^{2S+1}L and are called spectral terms. According to the first two Hund's rules [122], the level with the lowest energy is the one with higher S and the higher L. The orbital angular momentum of an electron in the 4f shell is $l = 3$. The lowest level configuration for Pr^{3+} ions, then, is the one in which the two electrons place themselves in $m_l = 3$ and $m_l = 2$ both with spin 1/2. This results in a total $L = |\sum m_l| = 5$ and $S = |\sum m_s| = 1$. The L quantum number is expressed by letters: $L = 0, 1, 2, 3, 4, 5, ... \equiv S, P, D, F, G, H, ...$. Then, in our case, the resulting lowest spectral term corresponds to $^{2S+1}L \rightarrow {}^3H$. This level is further split by the spin-orbit coupling, H_{SO}, i.e. the interaction between the electron spins and the magnetic field generated by the electrons orbiting around the nucleus. The consequent manifold is described also by a third quantum number, the total angular momentum J, as $^{2S+1}L_J$, where J can have the values J=L+S, L+S-1, ..., |L-S|. Each manifold is composed of 2J+1 degenerate levels. The third Hund's rule states that, for half or less than half filled orbitals, the lower state is the one where J is minimized [122]. Thus, for the free Pr^{3+} ion, with L=5 and two electrons in the shell, i.e. with J = 6, 5 or 4, the lowest manifold is $^3H_4$.

The crystal field interaction, H_C, in rare-earth doped crystals (REDCs), is smaller than the spin-orbit coupling. In fact, in most cases, the crystal matrix just acts as a perturbation within a single manifold. The crystal field levels in Pr^{3+} are defined as $^3H_4(n)$, with $n = 0, 1, ..$ up to a maximum value of 2J (depending on the crystal symmetry [117]). Thanks to the crystal field interaction the 4f-4f transitions become weakly allowed. When we cool the crystal to cryogenic temperature, the phonons do not have enough energy to excite the atoms to the higher levels of the ground manifold. The level in the manifold we refer to, then, is $^3H_4(0)$. In this thesis I will only consider the transitions between $^3H_4(0)$ and $^1D_2(0)$, because transitions involving levels with $n = 0$ show longer lifetimes and coherence times.

The next term, H_{HF}, represents the hyperfine interaction, i.e. the interaction between the nuclear spin, I, and the total angular momentum of the

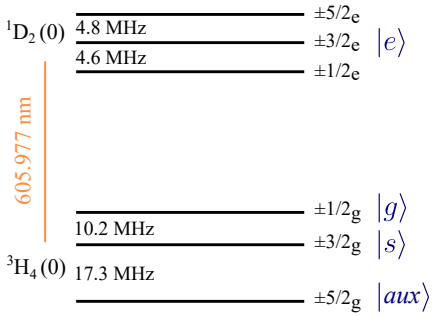

Figure 2.2: Energy level scheme of interest of Pr^{3+} ions site 1 doped in a Y_2SiO_5crystal, reporting the hyperfine separation of the lowest electronic sublevels (0) of the $^3H_4$ ground and $^1D_2$ excited manifolds.

electrons, J. In the only stable ion of Pr^{3+}, the nuclear spin is I=5/2 [123]. The first-order hyperfine interaction acts only on the crystal field doublets by splitting them into 2I+1 levels. As the levels in our transition of interest are all singlets, the first-order splitting does not happen. In second order, then, the hyperfine interaction splits each crystal field level into 3 new manifolds: $\pm 1/2$, $\pm 3/2$, $\pm 5/2$. The resulting energy level scheme of interest for this thesis, relative to Pr^{3+} doped into a Y_2SiO_5 matrix, is reported in fig. 2.2. Along the thesis I will mainly refer to the ground levels as the *ground* $|g\rangle$, the *spin* $|s\rangle$ and the *auxiliary* state $|aux\rangle$.

Each of these levels could be further splitted into two Zeeman levels by applying an external magnetic field. A more exaustive discussion of the whole derivation can be found in [117].

2.2.1 Pr^{3+}:Y_2SiO_5

The Y_2SiO_5 crystal is a widely used host for REIs thanks to the low nuclear magnetic moment of its constituents. It has a monoclinic biaxial structure. Being biaxial, three optical polarization axis can be defined: one is the crystallographic direction (b), the other two axis, D_1 and D_2, are perpendicular to b and between each other. The refractive index along b is n =1.76. In the unit cell, Y is present in two different sites, called site 1 and site 2 [124]. When a Y_2SiO_5 crystal is doped with Pr^{3+} ions, these substitute the Y^{3+} ions in both the crystallographic sites, but mostly in site 1. Moreover, the dipole moment of the 4f - 4f transitions is higher for atoms in the site 1. For these two reasons we will address Pr^{3+} ions in site

1 (in the thesis I will always refer to them, unless explicitly specified). Our transition of interest ${}^1D_2(0) \rightarrow {}^3H_4(0)$, for these specific ions, is centered at 605.977 nm. For maximum absorption, light will be polarized along the optical axis D_2.

2.2.2 Homogeneous Linewidth

Each atomic transition has an intrinsic absorption linewidth, called homogeneous linewidth, Γ_{hom}. It is called homogeneous because it is the same for each ion. The homogeneous linewidth of the 4f-4f transitions in REDCs is very small compared to other solid-state systems thanks to the screening effect provided by the 5s and 5p orbitals discussed previously. The coherence time, T_2, depends directly on Γ_{hom} as $T_2 = \frac{1}{\pi\Gamma_{\text{hom}}}$. A broadening of Γ_{hom} results in a shorter T_2.

The upper bound to the coherence time of a transition is fixed by twice its lifetime (or population decay time), $2T_1$ [125]. Nevertheless, there are many decoherence mechanisms that broaden Γ_{hom}. We can write:

$$\frac{1}{T_2} = \frac{1}{2T_1} + \frac{1}{T_2^{deph}},$$

where T_2^{deph}, called *pure dephasing*, accounts for all these processes [125]. Having the ions trapped in a crystal matrix removes the decoherence given by atomic motion, which is an important factor to take into account in atomic-cloud experiments. The stronger limiting factors to the coherence time in REDC are:

- Phonon-ion interactions, which represent the dominant effect at high temperatures but are negligible at cryogenic temperatures;
- Spin flips caused by magnetic fluctuations of the surrounding atoms [126]. This effect is reduced for non-Kramers ions (e.g. Pr^{3+}) and hosts with a low nuclear magnetic moment (e.g. Y_2SiO_5);
- Instantaneous spectral diffusion, i.e. the interaction between the dipole moments of different excited Pr^{3+} ions [126];
- Spectral diffusion, which represents a time-dependent shift in frequency caused by a local change of the electric or magnetic field in the position of the ion. This can be caused by interactions with

other neighbouring Pr^{3+} spins or by interactions of single Pr^{3+} ions with bistable two-level systems (TLS), being a dynamic fluctuation between nearly equivalent lattice configurations [84].

The last two decoherence effects, which depend on the presence of other Pr^{3+} ions, can be limited by using a REDC with low concentration of dopants. For example, the concentration of Pr^{3+} ions in the samples we use is $\sim 0.05\%$. Nevertheless, this results in a decreased optical depth (proportional to the absorption of the crystal) and inhomogeneous broadening. Other effects that can be highly reduced are the ones caused by magnetic fluctuations. By applying an external magnetic field with a specific intensity and direction, one can address the so-called zero first-order Zeeman shift (ZEFOZ) transitions [127]. The ions under these conditions become almost insensitive to low magnetic field changes (the frequency shift given by low magnetic fluctuations becomes negligible). This, besides being very important in Kramers ions which have a higher magnetic moment, is used in non-Kramers ions also. The spin-coherence of Pr^{3+}:Y_2SiO_5, for example, was extended with this technique from $\sim 500\,\mu$s to 860 ms [128].

2.2.3 Inhomogeneous broadening

When a dopant ion is hosted in a crystal, the surrounding matrix gets distorted and applies a strain to it. This strain is different for each dopant and comes, mostly, from lattice defects and chemical impurities, which are inevitable in most of the crystal growth processes. This gives rise to the so-called inhomogeneous broadening: depending on the different surroundings and crystal fields felt, each ion suffers a shift in its levels, i.e. in the central absorption frequency of its transitions. Thanks to it, the absorption of REDCs is many orders of magnitude broader than the single ion Γ_{hom}. For a Pr^{3+}:Y_2SiO_5 crystal with a doping concentration of $\sim 0.05\%$ we measure inhomogeneous broadenings of the order of 10 GHz (two measured traces are reported in Appendix B.3). Note that the inhomogeneous broadening is static, as it is caused by inhomogeneities in the crystal field. We can therefore tailor the absorption, which we will use for quantum memory protocols (see section 3.3).

Chapter 3

Light-matter interaction in rare-earth doped crystals

In this chapter I will shortly introduce a semiclassical formalism to describe the interaction between light and atoms. Then I will explain the optical protocols and techniques used along the thesis to characterize the spectral and coherence properties of the ions. Finally I will focus on the storage protocol, the atomic frequency comb, that we decided to use in this thesis.

3.1 Theoretical background

Most of the material of this section can be found in detail in [129, 130, 131]. Consider a quantized two-level atom and a classical monochromatic radiation field addressing it. The temporally dependent state of a two level atom can be described as:

$$|\psi\rangle = \mathrm{c}_g(\mathrm{t})\,|g\rangle + \mathrm{c}_e(\mathrm{t})\,e^{-i\omega_0 \mathrm{t}}\,|e\rangle \tag{3.1}$$

with $|\mathrm{c}_{g(e)}(\mathrm{t})|^2$ being the probability to have the atom in $|g\rangle$ ($|e\rangle$) at time t and ω_0 the resonance frequency of the transition $|g\rangle - |e\rangle$. We call $\hat{H}_0$ the Hamiltonian relative to the unperturbed atom, whose eigenstates are $|g\rangle$ and $|e\rangle$ with eigenvalues $\mathrm{E}_g = \hbar\omega_g$ and $\mathrm{E}_e = \hbar\omega_e$, respectively, where $\omega_e - \omega_g = \omega_0$.

3.1.1 Rabi frequency

The interaction between a monochromatic radiation field, $\mathbf{E} = \mathbf{E_0}\cos(\omega \mathrm{t})$, and the atom is governed by the Hamiltonian $\hat{H}_I = \mathbf{d} \cdot \mathbf{E}$. We call $\mathbf{d}$ the

atoms electric dipole moment operator. This is a non-diagonal operator such that $\langle g|\,\mathbf{d}\,|g\rangle = \langle e|\,\mathbf{d}\,|e\rangle = 0$ and $\langle g|\,\mathbf{d}\,|e\rangle = \langle e|\,\mathbf{d}\,|g\rangle = \mathrm{d}$.

Solving the Schrodinger equation:

$$i\hbar\frac{\partial\,|\psi\rangle}{\partial \mathrm{t}} = \hat{H}\,|\psi\rangle\,,$$

where we consider a total Hamiltonian $\hat{H} = \hat{H}_0 + \hat{H}_I$, we find:

$$\begin{cases} i\hbar\,\dot{\mathrm{c}}_g = \mathrm{c}_e e^{-i\omega_0 \mathrm{t}}\cos(\omega \mathrm{t})\,\langle g|\,\mathbf{d}\cdot\mathbf{E_0}\,|e\rangle \\ i\hbar\,\dot{\mathrm{c}}_e = \mathrm{c}_g e^{i\omega_0 \mathrm{t}}\cos(\omega \mathrm{t})\,\langle e|\,\mathbf{d}\cdot\mathbf{E_0}\,|g\rangle \end{cases} \rightarrow \begin{cases} i\,\dot{\mathrm{c}}_g = \mathrm{c}_e\left(e^{i(\omega-\omega_0)\mathrm{t}} + e^{-i(\omega+\omega_0)\mathrm{t}}\right)\,\Omega/2 \\ i\,\dot{\mathrm{c}}_e = \mathrm{c}_g\left(e^{i(\omega+\omega_0)\mathrm{t}} + e^{-i(\omega-\omega_0)\mathrm{t}}\right)\,\Omega/2 \end{cases}, \tag{3.2}$$

where we projected along $\langle g|$ or $\langle e|$, respectively. Here we introduced a new quantity, Ω, called Rabi frequency. It is defined as $\hbar\Omega = \langle g|\,\mathbf{d}\cdot\mathbf{E_0}\,|e\rangle = \langle e|\,\mathbf{d}\cdot\mathbf{E_0}\,|g\rangle$. For an easier treatment we consider a radiation field polarized along the electric dipole, for which $\hbar\Omega = \mathrm{E}_0\mathrm{d}$.

In our application we are interested in studying a radiation field close to resonance with the two-level system, $\omega \sim \omega_0$. In this situation we can neglect the fast-oscillating terms $(\omega + \omega_0)$ in eq. 3.2. This is called rotating-wave approximation. We now calculate the derivative of the second expression of eq. 3.2 and, after solving the system, we get:

$$\ddot{c}_e + i(\omega - \omega_0)\dot{c}_e + \frac{|\Omega|^2}{4}c_e = 0 \tag{3.3}$$

For an initial condition $|c_g(0)|^2 = 1$ and $|c_e(0)|^2 = 0$, i.e. starting with all the atomic population in the ground state $|g\rangle$, we find:

$$|c_e(\mathrm{t})|^2 = \frac{\Omega^2}{\Omega^2 + (\omega-\omega_0)^2}\sin^2\left(\frac{\sqrt{\Omega^2 + (\omega-\omega_0)^2}}{2}\,\mathrm{t}\right) \xrightarrow{\omega=\omega_0} \sin^2\left(\frac{\Omega}{2}\,\mathrm{t}\right). \tag{3.4}$$

This means that a light field resonant with the atomic transition drives the atomic population back and forth between the excited and the ground state. For a given intensity of the radiation field and the dipole moment of the atom, i.e. for a given Ω, the time for which we have the first inversion of population, $|c_e(\mathrm{t})|^2 = 1$, is $\mathrm{t}_\pi = \pi/\Omega$ and defines the so-called $\pi-$pulse. More precisely, as can be seen from eq. 3.2 and 3.3, by applying a $\pi-$pulse we get: $\mathrm{c}_g|g\rangle + \mathrm{c}_e|e\rangle \rightarrow -i(\mathrm{c}_g|e\rangle + \mathrm{c}_e|g\rangle)$. Note that the higher is the

Rabi frequency, the shorter t_π. This means that the Rabi frequency is proportional to the light-atom interaction. Equivalently to the $\pi-$pulse, we define the $\pi/2-$pulse as the shortest time needed to transfer half of the atomic population to the excited state, $|c_e(t)|^2 = 0.5$. In the case of a single atom in $|g\rangle$, a $\pi/2-$pulse drives it into the state $(|g\rangle + |e\rangle)/\sqrt{2}$.

3.1.2 Optical Bloch equations

For the following analysis we define the density matrix ρ associated to a quantum state, in this case to the state $|\psi\rangle$ of eq. 3.1, as:

$$\rho = |\psi\rangle\langle\psi| = \begin{bmatrix} |c_g|^2 & c_g c_e^* \\ c_g^* c_e & |c_e|^2 \end{bmatrix} = \begin{bmatrix} \rho_{11} & \rho_{12} \\ \rho_{21} & \rho_{22} \end{bmatrix}. \tag{3.5}$$

The diagonal elements are the probabilities to have the atom in one of the two states (the atomic population in case of many atoms), while ρ_{12} and ρ_{21}, called the *coherences* of the system, are related to the response of the system to a driving frequency. For example, if we calculate the expectation value of the dipole moment $\mathbf{d}$ for an atom with state ψ, we find that it only depends on the *coherences*:

$$\langle\psi|\,\mathbf{d}\,|\psi\rangle = d\left(c_g c_e^* e^{i\omega_0 t} + c_g^* c_e e^{-i\omega_0 t}\right) = d\left(\rho_{12} e^{i\omega_0 t} + \rho_{21} e^{-i\omega_0 t}\right). \tag{3.6}$$

Let's now define:

$$\tilde{c}_g = c_g\, e^{-i(\omega-\omega_0)t/2} \quad \text{and} \quad \tilde{c}_e = c_e\, e^{i(\omega-\omega_0)t/2}. \tag{3.7}$$

Rewriting $|\psi\rangle$ in terms of these variables and calculating $\tilde{\rho}$ as in eq. 3.5, we find the new *coherences*, $\tilde{\rho}_{12}\, e^{-i(\omega-\omega_0)t}$ and $\tilde{\rho}_{21} = (\tilde{\rho}_{12})^*$ (the population of the two states remain unvaried). In these terms eq. 3.6 becomes:

$$\langle\tilde{\psi}|\mathbf{d}|\tilde{\psi}\rangle = d\left(\tilde{\rho}_{12} e^{i\omega t} + \tilde{\rho}_{21} e^{-i\omega t}\right) = d(u\cos(\omega t) - v\sin(\omega t)). \tag{3.8}$$

With the new *coherences* we directly see the response of the system to ω, the frequency of the applied radiation. In a second step we define u and v, which are related to the real and imaginary part of $\tilde{\rho}_{12}$, respectively as:

$$\begin{cases} u = \mathrm{Re}(\tilde{\rho}_{12})/2 = \;\; \tilde{\rho}_{12} + (\tilde{\rho}_{12})^* \;\; = \tilde{\rho}_{12} + \tilde{\rho}_{21} \\ v = \mathrm{Im}(\tilde{\rho}_{12})/2 = -i[\tilde{\rho}_{12} - (\tilde{\rho}_{12})^*] \;\; = -i(\tilde{\rho}_{12} - \tilde{\rho}_{21}). \end{cases} \tag{3.9}$$

The set of expressions in 3.2 and 3.3, in terms of u and v, become:

$$\begin{cases} \dot{u} = \delta v \\ \dot{v} = -\delta u + \Omega w \\ \dot{w} = -\Omega v \end{cases}, \tag{3.10}$$

where $\delta = \omega - \omega_0$ is the detuning of the radiation field with respect to the resonance frequency of the atom and where we defined a new variable $w = \rho_{11} - \rho_{22}$ (remind that $\rho_{11} + \rho_{22} = 1$). w represents the difference of population in the two levels of the atom, while u and v are proportional to the in-phase and in-quadrature components of the dipole moment (see eq. 3.8).

It is possible to see that $|u|^2 + |v|^2 + |w|^2 = 1$. The normalized sphere defined by these three variables is called Bloch sphere. If we associate the three variables to perpendicular axes, they define the Bloch vector, as shown in fig. 3.1.

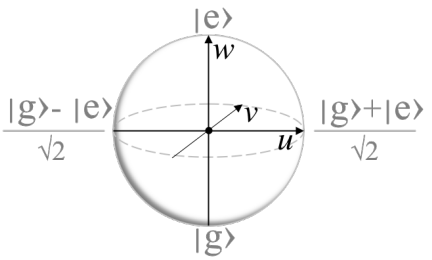

Figure 3.1: Bloch sphere with the vectors correspoding to the three components u, v and w.

To include the effect of dephasing into our model, we consider a damping effect, Γ. In analogy with the model of a damped classical oscillator [129], and considering as the energy of our system $\rho_{22}\hbar\omega_0$ (proportional to the population in $|e\rangle$), we can rewrite the last equation of the system 3.10 as:

$$\dot{\tilde{\rho}}_{22} = -\Gamma\tilde{\rho}_{22} + \Omega v/2.$$

Solving this expression in the case of no radiation field, the population in the excited state would decay exponentially as $e^{-\Gamma t}$. In this analogy, then,

$\Gamma = 1/T_1$, where T_1 is the lifetime of the transition (see section 2.2.2). Following the analogy to the same model [129], it is possible to see that the *coherences*, and therefore u and v, are affected by a damping parameter $\Gamma/2$, which defines the coherence time T_2 (see section 2.2.2). The set of equations 3.10 considering the damping becomes:

$$\begin{cases} \dot{u} = \delta v - \frac{\Gamma}{2} u \\ \dot{v} = -\delta u + \Omega w - \frac{\Gamma}{2} v \\ \dot{w} = -\Omega v - \Gamma(w - 1) \end{cases} . \tag{3.11}$$

This set of equations is known as optical Bloch equations and describes the behaviour of a two-level system interacting with a radiation field close to resonance and in presence of spontaneous decay.

T_1 and T_2 can be seen as the relaxation time of the energy and of the phase, respectively. In this simple model we find that $T_2 = 2T_1$. As discussed in sec. 2.2.2, most often we have $T_2 \leq 2T_1$. The set of equations in 3.11, should be rewritten in terms of T_1 and T_2 to account for this.

3.1.3 Maxwell-Bloch equations

Equivalently to a classical oscillating dipole, an atom oscillating between the ground and excited state radiates. To consider this effect on the radiation field we start from the classical Maxwell equation [130, 131]. Let's call z the direction of propagation of the light through the system. The interaction between system and radiation field depends on z, so that we consider the dependence on z of Ω, u, v and w. The classical Maxwell equation in the rest frame can be written as:

$$\nabla^2 E(z,t) - \frac{n^2}{c^2}\frac{\partial^2}{\partial t^2} E(z,t) = \frac{1}{\epsilon_0 c^2}\frac{\partial^2}{\partial t^2} P(z,t) \tag{3.12}$$

where n is the refractive index of the medium, c is the speed of light, ϵ_0 the vacuum permittivity and $P(z,t)$ is the macroscopic polarization of our system, that is what will mostly determine the effect of the atomic system on the radiation field. For an inhomogeneoulsy broadened ensemble of N

atoms [131], $P(z,t)$ can be described as:

$$P(z,t) = \frac{Nd}{2\pi}\int_0^\infty \left[u\cos(\omega t - k_z z) - v\sin(\omega t - k_z z)\right] g(\delta)\, d\delta \tag{3.13}$$

where $g(\delta)$ is the function associated to the inhomogeneous broadening.

Substituting 3.13 into 3.12 and performing the so-called slowly varying envelope approximation, i.e. assuming that the envelope of the radiation field varies slowly with respect to the optical frequency ω, we find:

$$\left(\frac{\partial}{\partial z} + \frac{n}{c}\frac{\partial}{\partial t}\right)\Omega(z,t) = \frac{i\alpha}{2\pi}\int_{-\infty}^{+\infty}\left[u(z,t;\delta) - iv(z,t;\delta)\right] g(\delta)\, d(\delta), \tag{3.14}$$

where we defined the absorption coefficient α. This is called Maxwell-Bloch equation. In our experiments we are not interested in effects varying as fast as L/c (being L the length of our medium) so that we can neglect the terms that goes like $\frac{n}{c}\frac{\partial}{\partial t}$ [131].

The Maxwell-Bloch equations can be written as a function of $\sigma = u - iv$, or separating the real and imaginary components of the formula:

$$\begin{cases} \frac{\partial \Omega_{Re}}{\partial z} = \frac{\alpha}{2\pi}\int_{-\infty}^{+\infty} v\, g(\delta)\, d(\delta) \\ \frac{\partial \Omega_{Im}}{\partial z} = \frac{\alpha}{2\pi}\int_{-\infty}^{+\infty} u\, g(\delta)\, d(\delta) \end{cases} . \tag{3.15}$$

This formalism can be used to understand the storage protocol that I will use throughout the thesis, the atomic frequency comb [68], and, more generally, photon-echo experiments [132].

3.1.4 Ω: optical nutation

As we saw in the previous analysis, if we excite a two-level system with a detuned laser, the Bloch vector associated with the atomic state oscillates between the ground and excited levels as $\sqrt{\delta^2 + \Omega^2}\, t/2$, δ being the detuning (see eq. 3.4). This oscillation of the Bloch vector is called optical nutation [125]. In an inhomogeneously broadened transition, different atoms excited have a different detuning. The average optical nutation, in this case, is proportional to $\Omega^2\, J_0(\omega\, t)$ [133], with $J_n(x)$ the n^{th}-order

Bessel function of the first kind at x. Finally, for a Gaussian beam, averaging the effect along the transverse profile of the field, we get an atomic excitation oscillating as $\Omega^2 J_1(\omega t)/(\omega t)$ [133].

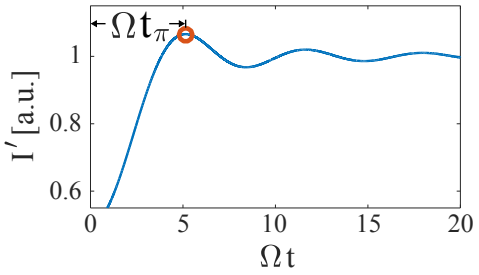

Figure 3.2: Simulation of a typical optical nutation measurement trace, showing the intensity of a laser, in resonance with a two-level atom, measured in transmission. The arrow and the red point indicate the first population inversion (from the ground to the excited state)

To measure the Rabi frequency, then, we shine a laser resonant with an inhomogeneously broadened transition into our sample. Provided that we can initialize all the atoms in one ground state, the excited-state population $|c_e|^2$ will vary as discussed above. The more atoms are transferred to the excited state, the less the intensity of the laser is absorbed. In transmission, then, we will measure a transmitted laser intensity

$$I' \propto 1 - \mathrm{M}\Omega^2 J_1(\omega t)/(\omega t),$$

M being a constant parameter (see fig. 3.2). In this case, t_π happens in the first maximum of I', namely $\Omega t_\pi \sim 5.1$.

3.1.5 T_2: two-pulse photon echo

We measure the T_2 of an optical transition by means of the two-pulse photon echo (TPE) technique. The experimental procedure is sketched in fig. 3.3. We start with all the atoms in a certain level $|g\rangle$. A $\pi/2$-pulse at time 0 transfers half of the population to a second state $|e\rangle$ (see sec. 3.1). If the transition is inhomogeneously broadened, each excitation evolves with a different phase (due to their different central absorption frequencies). After a certain time τ, a $\pi-$pulse inverts the phases of the excited atoms (sec. 3.1). In this way the atomic excitations get back to rephase, restoring the atomic coherence at a time 2τ. Here the atoms fall

back to $|g\rangle$, resulting in a coherent photonic emission, the two-pulse echo (TPE) [132, 134].

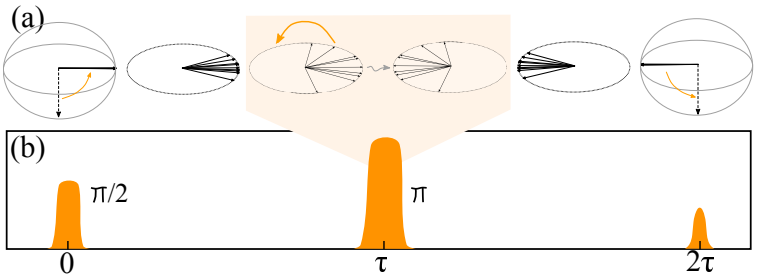

Figure 3.3: Sketch of the two-pulse photon echo (TPE) protocol. A $\pi/2$-pulse creates an atomic excitation at time 0. A π-pulse at time τ inverts the phases of the atoms excited. At time 2τ the coherence of the atomic excitation is restored and an echo is emitted. (a) Phases of the atoms in the Bloch sphere. (b) Temporal sequence.

Besides the static inhomogeneous dephasing, which is reversed by the $\pi-$pulse, all the other decoherence or relaxation mechanisms that contribute to decreasing the number of atoms participating in the rephasing, i.e. to the echo generation, are irreversible (see sec. 2.2.2). As these processes can happen in each moment between the first pulse and the time of the echo (2τ), increasing τ results in a decay of the TPE. From the exponential decay of the echo intensity (proportional to the square of the oscillation amplitude) while increasing the time τ, we extract the coherence time of the ions. The usual T_2 measured in our samples ranges from 50 to 110 μs, depending on the density of ions excited (beam size, power of the $\pi/2-$pulse and number of ions prepared in the ground state). In fact, the higher the number of ions excited, the more our T_2 is limited by ISD. In Pr^{3+}:Y_2SiO_5, the highest reported T_2 to my knowledge is 111 μs without any external magnetic field, comparable to our best measurements, and it arrives to 152 μs when applying a magnetic field [126].

3.1.6 T_1: fluorescence

The T_1 of the optical transition is associated with the population decay time (see sec. 3.1). This can be measured by a fluorescence measurement: we excite many atoms by sending a pulse in resonance with the transition of interest and we wait for the atomic population to decay. Each time that one atom falls back to the initial level, it emits one photon, resulting in a

fluorescence signal. Fitting the data to an exponential decay, we measured the T_1 of one of our samples to be $\sim 160\,\mu s$ [119], compatible with the value of 164 μs reported in the literature [126].

The T_1 of a transition can be also measured by adding a third pulse to the TPE scheme of sec. 3.1.5. This scheme, called three-pulse photon echo or stimulated photon echo (SPE), is explained in Chapter 7.

3.2 Spectral hole-burning

In some inhomogeneously broadened media, shining pulses of light at a specific frequency in the absorption profile can cause the generation of a *transparency window*, i.e. an increased transmission at that specific frequency. This process takes the name of spectral hole-burning and it is a fundamental tool for all the protocols used in the thesis [135].

Let's consider the level scheme of fig. 2.2. A pulse resonant with the $\pm 1/2g \rightarrow \pm 1/2e$ transition excites part of the atoms that were in the $\pm 1/2g$ level. These atoms will consequently decay in the three ground states with different probabilities (related to the dipole moment, or oscillator strength, of the transitions). This results in a lower number of atoms in the $\pm 1/2g$ level, i.e. in a lower absorption in the three transitions starting from the $\pm 1/2g$ state, generating a series of holes in the absorption profile. Consequently, the increased number of atoms in the $\pm 3/2g$ and $\pm 5/2g$ states creates anti-holes in the absorption profile of the crystal. From these holes and anti-holes it is possible to reconstruct the energy separation between the levels involved [135]. Their height is related to the oscillator strength of the transitions.

Note that, to perform protocols based on spectral hole-burning in which we redistribute the population in the spin levels to tailor the absorption profile of the system, we need the population lifetime of the spin transition T_1^s to be much longer than the optical T_1^o. In fact these protocols need many repetitions of optical sequences that excite the optical transition, during which the spin population should not redistribute.

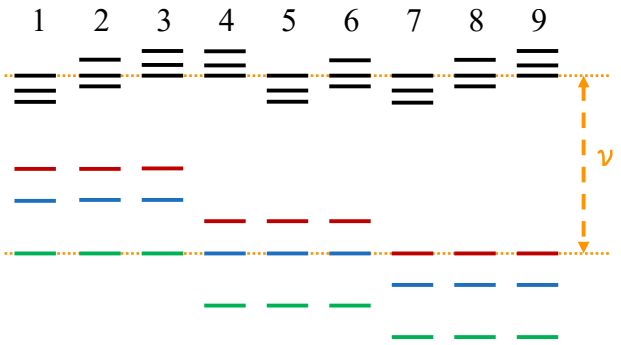

Figure 3.4: Sketch of the 9 classes of ions present in Pr^{3+}:Y_2SiO_5 due to inhomogeneous broadening.

3.2.1 Classes of ions

The inhomogeneously broadened absorption profile of the 4f-4f transitions in our crystal is composed of Pr^{3+} ions all with about the same Γ_{hom} and hyperfine separation (fig. 2.2), but each of them with a different central absorption frequency. As a consequence, provided that the inhomogeneous broadening is much bigger than the separation between the hyperfine levels, when a narrowband light pulse of frequency ν is sent through the crystal it can be resonant to different transitions for different ions (see fig. 3.4). In particular, within each window of about 40 MHz in the inhomogeneous line, we can define 9 different classes of ions according to the transition addressed. This discretized description can help us to simplify the understanding of such a complex system. At the same time, the spectral hole-burning technique explained before, becomes more complicated when we take into account all the classes. A simple explanation of the hole-burning technique in presence of more than one class of ions can be found in [119]. An experimental trace of the holes and antiholes generated by a narrowband laser shined within the inhomogeneous line of a Pr^{3+}:Y_2SiO_5-waveguide is shown in Appendix C.3.1.

3.2.2 Single-class absorption feature in Pr^{3+}

Throughout the thesis we will refer to the level scheme of fig. 2.2. Here I explain how to address only one of the nine classes of ions. In particular, how to populate in a controlled way a single class of ions, for example class 2, in the $\pm 1/2g \rightarrow \pm 3/2e$ transition via spectral hole-burning.

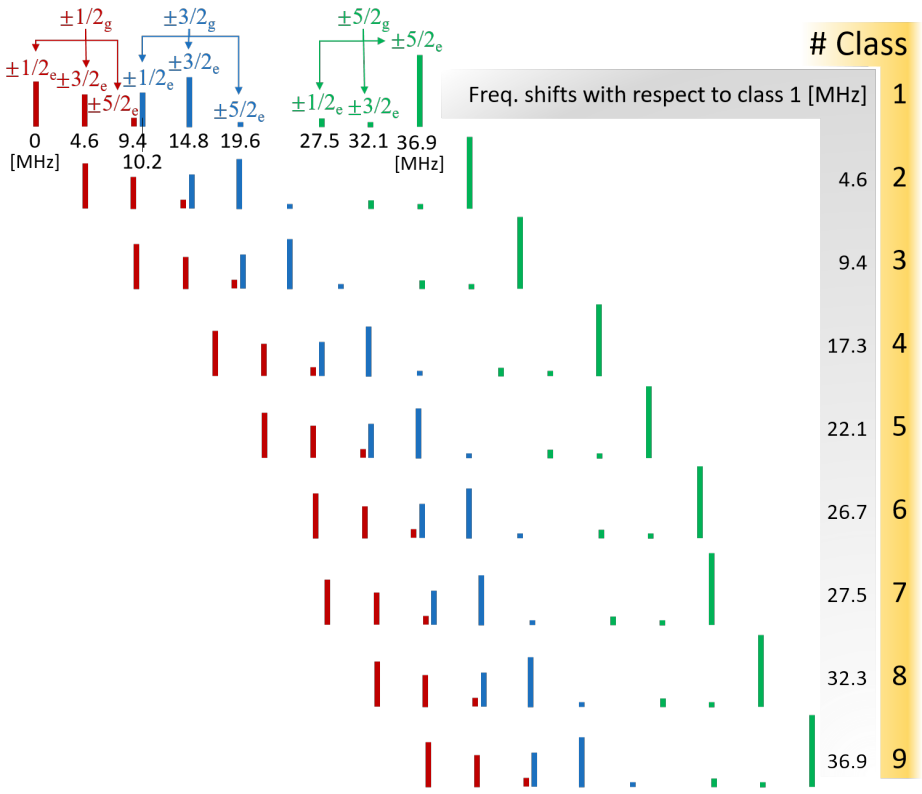

Figure 3.5: Optical transitions of the 9 classes of Pr^{3+} ions. The transition defined by each line is indicated in the first row. Each row is a different class of ions (see column on the right). The shift of each class with respect to the first one is written in the gray column. The height of the lines is proportional to the dipole moment of the transition.

In the following explanation I will refer to fig. 3.5. In this figure we report the 9 transitions, their height being proportional to their oscillator strength, for each class of ions (rows). For each row the three red (blue) [green] lines correspond to the transitions from the $\pm 1/2g$ ($\pm 3/2g$) [$\pm 5/2g$] state, to the $\pm 1/2e$, $\pm 3/2e$ and $\pm 5/2e$ states. The frequency shift of each class with respect to the first class of ions is reported in the gray column. At the bottom of the transitions of the first class I report the frequency difference (in MHz) of those transitions with respect to the $\pm 1/2g \rightarrow \pm 1/2e$ (first red line). I quantify the absorption in terms of optical depth, OD, that accounts for the number of atoms we are interacting with. It is defined as OD$= \alpha$L, where α is the absorption coefficient of the crystal (see sec. 3.1) and L its length.

We first create a spectral *pit*, i.e. a $\sim$ 16 MHz broad hole around the $\pm 1/2g \rightarrow \pm 3/2e$, $\pm 1/2g \rightarrow \pm 5/2e$, $\pm 3/2g \rightarrow \pm 1/2e$ and $\pm 3/2g \rightarrow \pm 3/2e$ transitions of the second class of ions, as shown as a green rectangle in fig. 3.6 (a). While interacting with the second class of ions, we interact also with other classes (all the transitions highlighted in the green rectangle are addressed). In the frequency window considered, we interact with the ions of the first four classes. For this reason, from the next step we will not consider any ion belonging to higher classes. Moreover, creating a hole in a transition starting from a certain ground state, as explained previously, has the effect to empty that ground state, i.e. to create a hole even in the other two transitions starting from the same ground state. The transitions emptied by generating a spectral pit are depicted as thinner lines. A sketch of the resulting zero absorption around the frequency of the spectral pit is depicted in the inset of the same figure.

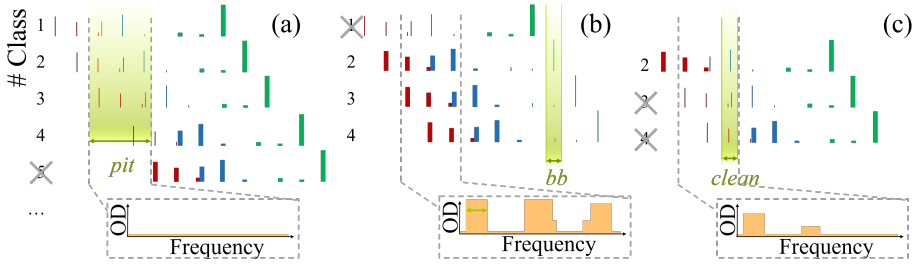

Figure 3.6: Sketch of the protocol used to create a single class absorption feature in the $\pm 1/2g \rightarrow \pm 3/2e$ and $\pm 1/2g \rightarrow \pm 5/2e$ transitions of the second class of Pr^{3+} ions. The protocol consists of three parts: the spectral pit (a), the burn-back (b) and the clean (c). At the top of each panel the classes and transitions involved, at the bottom the OD in the frequency window considered.

Secondly we shine a pulse, the *burn-back* (*bb*) pulse, on the $\pm 5/2g \rightarrow \pm 5/2e$ transition of class 2 (green rectangle in fig. 3.6(b)). This, beside emptying the resonant transitions, repopulates the $\pm 1/2g$ and $\pm 3/2g$ states of the second class with the resulting anti-holes. This is important because we can repopulate the desired ground states in a controllable way, i.e. with the desired OD (depending on the power and repetitions of the bb-pulse) and width (depending on the frequency chirp of the bb-pulse). The resulting absorption profile within the pit is depicted in the inset of fig. 3.6(b). Note that the bb-pulse is not in resonance with any transition of the first class of ions, so that we can avoid considering any class of ions lower than the second.

Finally, to eliminate the third and fourth classes from the selected frequency range, we shine a *clean* pulse around the frequency of the $\pm 3/2g \rightarrow \pm 3/2e$ transition of the second class (green rectangle in fig. 3.6(c)). This pulse empties the ground state $\pm 3/2g$ of the second class, as well as the levels $\pm 1/2g$ and $\pm 3/2g$ of the third and the $\pm 1/2g$ of the fourth. At this stage, the only populated level in the considered frequency window will be the $\pm 1/2g$ of the second class.

In conclusion, we populated in a controlled way two single-class transitions, the $\pm 1/2g \rightarrow \pm 3/2e$ and the $\pm 1/2g \rightarrow \pm 5/2e$ transitions of the second class, as shown in the inset of fig. 3.6(c) (the OD of the second transition is smaller because of its lower oscillation strength).

3.3 Atomic frequency comb

The storage protocol that we use is the so-called atomic frequency comb (AFC) technique [68]: a periodical structure (the AFC) is tailored in the inhomogeneous absorption of the crystal, with a separation of Δ between its peaks. A photon absorbed by such structure is mapped into a collective excitation of atoms. A single photon has enough energy to excite only one atom, so that the collective excitation is a superposition of single atomic excitations where only the atom k is promoted to the excited state $|e\rangle$, while the others remain in the ground state $|g\rangle$. This can be mathematically described as a Dicke state of the form:

$$\sum_k e^{-i2\pi\delta_k t} c_k |g \cdots e_k \cdots g\rangle.$$

In the phase term, the frequency detuning δ_k of an atom k with respect to the central frequency of the photon is a multiple of Δ and can be written as $\delta_k = m_k\Delta$. Its amplitude c_k depends on its specific position in the crystal and central absorption frequency. After an initial inhomogeneous dephasing, the atomic excitations will rephase at a time $\tau = 1/\Delta$ giving rise to a re-emission of the photon in the forward direction, the so-called AFC echo [68]. The storage and retrieval efficiencies of the process depend mostly on the optical depth, OD, on the background OD, d_0, i.e. the absorption given by atoms remaining in the unwanted frequencies (fig. 3.7(a)), and on the finesse of the comb, $F = \Delta/\gamma$, with γ the width of

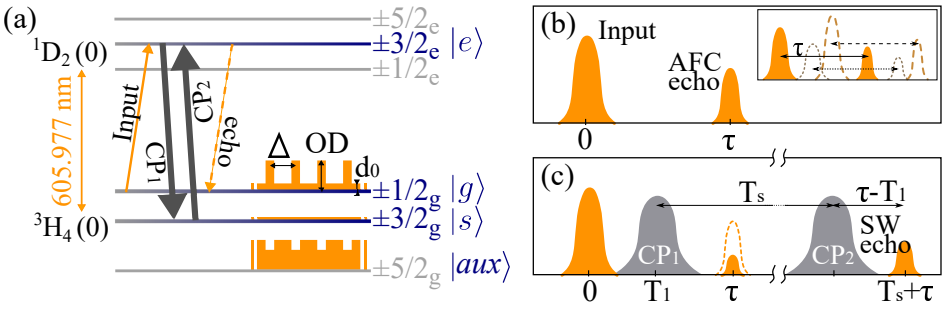

Figure 3.7: (a) Level scheme of the transition of interest in Pr^{3+}:Y_2SiO_5. The chosen Λ-scheme for the storage is indicated by arrows. The prepared spectral features in the atomic populations of the three ground states are sketched on the right side in orange. (b) Temporal sequence of the AFC storage: an optical pulse (or a photon) is sent at time 0. In presence of an AFC, it is absorbed and an AFC echo is reemitted after a time τ. In the inset the intrinsic temporal multimodality of the protocol: if N pulses are sent at N different times, each of them will be absorbed and reemitted after a time τ. (c) Temporal sequence of SW storage: a control pulse before the AFC echo (CP1), transfers the excitation to the spin state. The atoms not transferred due to the imperfect CP1, rephase and result in an AFC echo (the dotted line being the AFC echo without CP1). A second control pulse (CP2) brings back the excitation to the excited state. A SW echo is emitted at time τ+T_s

the peaks [68] (the formula can be found in sec. 3.3.2). It is important to remark that this scheme provides just a pre-programmed storage time.

An example of single-class AFC tailored in the $\pm 1/2g \rightarrow \pm 3/2e$ transition ($|g\rangle \rightarrow |e\rangle$) is sketched in figure 3.7(a). The input single photon and AFC echo are represented as a solid thin orange arrow and a dashed one, respectively. The atoms optically pumped away from the ground state $|g\rangle$ are transferred to the auxiliary state $\pm 5/2g$. In this way the spin-state, $|s\rangle$, is kept empty and can be used to store photons for longer times as spin-waves, and with an on-demand readout (see sec. 3.3.1). A sketch of the temporal trace of the AFC storage is reported in fig. 3.7(b). A very important property of the AFC technique is its intrinsic temporal multimodality, i.e. the possibility to store and retrieve multiple distinguishable temporal modes. As shown in the inset of fig. 3.7(b), if many photons arrive at different times (solid line, dashed line and dotted line represent three different photons), each of them will rephase after a time τ, independently from the others. With an AFC-based memory the maximum number of temporal modes that can be stored is proportional to the number of peaks

of the AFC [68]. The ultimate limit is given by the maximum width of the comb, about 4 MHz in Pr^{3+}, and the smallest peak that can be burned, limited by the laser linewidth and the homogeneous linewidth of the ions (about 3 kHz in our crystal without applying an external magnetic field [126]). This is not true for the other storage protocols, like EIT, GEM or Raman schemes, where the number of temporal modes that can be stored depend on the OD of the system [136] (see sec. 1.2.1.1).

The experimental procedure followed to tailor an AFC is described in detail in the next chapter (sec. 4.4).

3.3.1 Spin-wave storage

The AFC protocol can be exploited to perform a long-lived storage with on-demand read-out, called full AFC protocol or spin-wave (SW) storage [68]. The storage sequence is sketched in fig. 3.7(c): before the rephasing of the atoms the collective excitation is mapped onto the so-called *spin-state*, $|s\rangle$, using a strong optical pulse, called control pulse (CP1, first gray arrow in fig. 3.7(a)). The spin excitation is described by: $\sum_k c_k|g\cdots s_k\cdots g\rangle$. The phases of the spins remain frozen until they are transferred back to the excited state with a second control pulse identical to the first one (CP2, second gray arrow in fig. 3.7(a)). Here the atomic excitations complete the rephasing, finally emitting the so-called SW echo after a total storage time $T_{SWS} = \tau + T_s$, with T_s the time spent in the spin-state (i.e. the time between the two control pulses). T_s is then limited by the coherence of the spin-state, which can be increased using different techniques [127] up to a maximum fixed by the population lifetime of the spin state, T_1^s. The longest demonstrated storage time in the spin state of Pr^{3+} ions is $\sim$ 1 minute for classical light pulses and using another storage protocol, namely electromagnetically induced transparency [72].

3.3.1.1 Spin Inhomogeneity

The inhomogeneous broadening shifts also the ground states of the doped ions, i.e., when the atoms are mapped into the spin state each of them will be slightly detuned [88]. Therefore, after the time T_s between the two control pulses they will acquire different phases, thus degrading the retrieval efficiency of the protocol. Studying the decay of the SW echo as a

function of T_s, we can measure the inhomogeneous broadening of the spin-state, called spin inhomogeneity, as proportional to $\exp\left[\frac{-(\gamma_{\text{inh}}T_s)^2}{2\log(2)/\pi^2}\right]$. In samples like ours this is usually measured to be ~ 25 kHz [88, 119, 28, 137] (an experimental trace measured in a bulk sample is shown in section 5.4.3). This spin inhomogeneity results in a quite fast decay of the spin-wave echo, on the order of tens of μs. Nevertheless the inhomogeneous dephasing can be compensated with spin-echo techniques [138, 128], i.e. using π-RF-pulses, resonant to the $|g\rangle$-$|s\rangle$ transition, to invert the phases of the atoms and let them rephase at the time of the second control pulse (using the same idea behind the TPE of sec. 3.1.5).

3.3.2 AFC and SW storage efficiencies

The maximum efficiency achievable using the AFC protocol is limited to $\eta_{\text{AFC}}^{fw} = 54\%$ if the echo is retrieved in the same direction as its input (*forward retrieval*). This effect is caused by the re-absorption of the retrieved light in the memory [68]. If, instead, we recall it back-propagating (*backward retrieval*) the maximal efficiency can reach $\eta_{\text{AFC}}^{bw} = 100\%$ [68].

The formulas [109], considering an AFC with square peaks (the best case scenario in terms of efficiencies [139]), are:

$$\eta_{\text{AFC}}^{fw} = \tilde{d}^2 e^{-\tilde{d}} \text{sinc}^2(\pi/F) e^{-d_0}, \tag{3.16}$$

$$\eta_{\text{AFC}}^{bw} = \left(1 - e^{-\tilde{d}}\right)^2 \text{sinc}^2(\pi/F) e^{-d_0}. \tag{3.17}$$

To retrieve the stored light backward, one could embed the memory into an impedance-matched cavity or perform SW storage using two CPs counter-propagating between each other. For SW storage, the achievable efficiency is related to η_{AFC}, being:

$$\eta_{\text{SW}} = \eta_{\text{AFC}}\, \eta_{\text{T}}^2\, \eta_{\text{C}}, \tag{3.18}$$

where η_{T} is the transfer efficiency of each CP and η_{C} accounts for the dephasing experienced in the spin-state due to spin inhomogeneity.

Chapter 4

Experimental setup

The experimental setup consists of three main parts: (1) the laser preparation part, where the light at 606 nm generated by the laser is split in different beams to be modulated and locked in frequency; (2) the memory setup, where the storage and retrieval processes and the characterization measurements take place; (3) the photon-pair source setup (PhD project of other students of the group). In this chapter I will give the general experimental details of these three parts. Then I will focus on the optical sequence used to tailor a single-class atomic frequency comb (AFC).

4.1 Laser operation and modulation

Our laser source at 606 nm, a second harmonic generation laser (Topica, DL-SHG-pro), is stabilized in frequency, using the Pound-Drevel-Hall technique, to a Fabry-Perot cavity hosted in a home made vacuum chamber [107]. From this laser we derive all the beams necessary to prepare and operate the memory (see figure 4.1). Both amplitude and frequency of the different beams are modulated with double pass acousto-optic modulators (AOMs) driven by an arbitrary waveform generator (Signadyne). The four AOMs are used independently for the four different paths.

A first beam is used to prepare the quantum memory by spectral hole burning techniques. We call it the preparation beam. A second beam is used to probe and characterize the memory, either sending classical optical pulses or weak coherent states. A third beam is used to prepare a narrow spectral window in a second crystal, that we call filter crystal (FC in fig. 4.2). This crystal is used as a narrowband tunable spectral filter for the

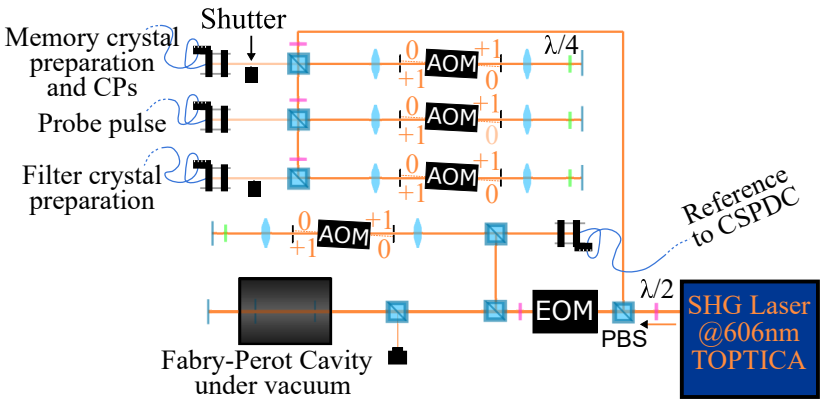

Figure 4.1: Setup for the laser modulation: the light emitted by the laser at 606 nm, is split in two parts by a polarizing beam-splitter (PBS). The reflected beam is divided again in 3 paths. Before each PBS a $\lambda/2$ is used to change the powers going to the different beams. Each path is modulated via independent AOMs aligned (to the mode +1) in a double pass configuration (giving a modulation of twice the resonance frequency). The beam transmitted by the first PBS is modulated by an electro-optic modulator (EOM). Another PBS is used to split the beam: the light reflected is modulated with an AOM and is sent to the photon-pair source. The transmitted light is sent into a Fabry-Perot cavity, and it is used to stabilize the frequency emitted by the laser using the Pound-Drevel-Hall technique. For each AOM, a $\lambda/4$ waveplate in double pass changes the initial polarization to its perpendicular. The light is focused into the AOMs and recollimated with 25 cm lenses.

experiments of spin-wave storage at the single photon level. These three beams are fiber-coupled and sent to another table where the memory is hosted. The last beam is first modulated with a frequency of 12.5 MHz with an electro-optic modulator (EOM) to provide the sidebands necessary for the locking system. This beam is split in two paths, one of which is sent to the Fabry-Perot cavity and is used to lock the 606 nm laser. The other one, after passing through its double pass AOM, is sent to the photon-pair source. We call this beam *reference light*, as it is used as a reference for the source to generate photons at the same frequency at which the memory is prepared (see section 4.3).

4.2 Memory experimental setup

The experimental setup used for the storage is similar for all the experiments described in this thesis. I report here the general details of the

setup, which is shown in fig. 4.2. The main differences from an experiment to another depend on whether we use a bulk sample or a waveguide. In both cases, the memory consists of a Pr^{3+}:Y_2SiO_5 crystal cooled down to $< 3\,K$ (usually $\sim 2.8\,K$) in a cryostat (closed-cycle cryocooler, Oxford Instruments). The Pr^{3+}:Y_2SiO_5 crystals that we use are produced by Scientific Materials, with an active-ion concentration of 0.05 %. The length of the samples used will be specified in each experiment and ranges from 3 mm to 1 cm.

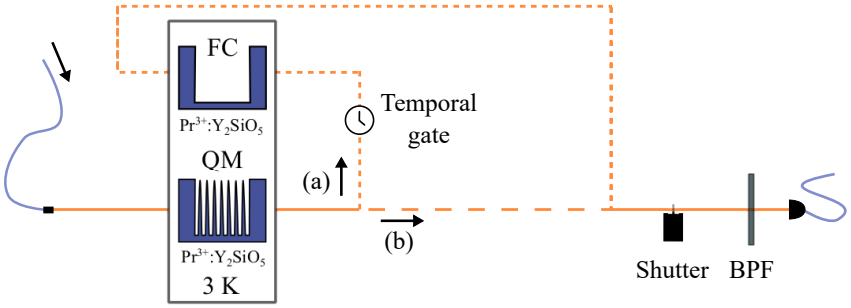

Figure 4.2: Memory experimental setup. Two crystals, the memory (QM) and the filter crystal (FC) are placed in a cryostat at a temperature of $< 3\,K$. When the FC is used, a fast temporal gate, composed by two AOMs, is placed between the two crystals. A shutter and a band pass filter (BPF) are placed before the fiber that guide the light to the detector.

The incoming light to store, either single photons or classical pulses, is sent through the memory crystal along the Y_2SiO_5 crystalline b-axis and it is polarized along its D_2-axis (to address Pr^{3+} ions in site 1).

After the memory we can follow two different strategies. When we perform spin-wave (SW) storage of single photons (Chapter 5), we protect the single photon detector (SPD) from the control pulses by adding a fast temporal gate (composed of two AOMs). The AOMs are also used to avoid the preparation of a hole in the filter crystal by the leakage of the control pulses. Moreover, to filter out the noise generated by the control pulses, which is only 10.2 MHz away from the frequency of the stored light, we put a second Pr^{3+}:Y_2SiO_5 crystal into the cryostat, and we use it as a narrow-band spectral filter (the already mentioned filter crystal). We further filter the light with a band-pass filter (centered at 600 nm, linewidth 10 nm, Semrock). In all the other experiments, where we either store single photons without performing SW storage or we store classical pulses,

the light is directly sent to the detection stage. When measuring at the single photon level we further protect the SPD with a mechanical shutter which remains closed during the whole memory and filter preparation. Two other shutters, in anti-phase with the first one, are installed before the memory and filter preparation beams, respectively (see fig. 4.1), and remain closed during the single photon measurement period, blocking the leakage from the preparation AOMs. The shutter is not present in the memory preparation for spin-wave storage measurements, as we use that beam to send control pulses. All the experiments are synchronized with the cycle of the cryostat (1.4 Hz) to reduce the effect of the mechanical vibrations. More details, specific to each experiment, will be reported chapter by chapter.

Our main SPD at 606 nm is a Silicon Avalanche photodiode (Laser Components) with 50 % detection efficiency and 10 Hz dark-count rate. For auto-correlation measurements we add a second Si-SPD: either a tau-SPAD, detection efficiency 45 %, dark count rate 15 Hz from PicoQuant (Chapter 5) or an Excelitas SPD with 50% detection efficiency and 50 Hz dark-count rate (Chapters 7). In Chapter 8 we use various SPDs for different measurements (it will be stated directly in the Chapter).

4.3 Photon-pair source

In the following experiments we will show storage of photons generated by two different photon-pair sources. They have been developed during the PhD projects of two students in our group, Dr. Daniel Rielander and Dario Lago Rivera. They are based on the same scheme that I am going to describe in this section. I will give more details about the properties of the generated photons in the following subsections.

Our photon-pair sources (fig. 4.3) are based on cavity-enhanced spontaneous parametric down conversion (CSPDC) in a 2 cm-long type I periodically-poled lithium niobate (PPLN) crystal [106]. The non-linear crystal is pumped with a 426 nm laser (Toptica TA SHG) to produce widely non-degenerate photon pairs. One photon of the pair, the idler, is at telecom wavelength (Telecom E-band, 1436 nm), while the other, the signal, is at 606 nm. The crystal is placed inside a bow-tie cavity (BTC). To ensure that the signal photons are resonant with the quantum memory, the length of

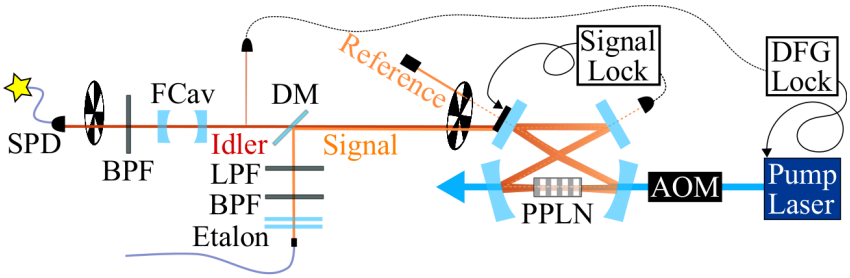

Figure 4.3: Experimental setup for storage of heralded single photons (PPLN: periodically-poled lithium niobate; DFG: difference frequency generation; DM: dichroic mirror; FCav: filter cavity; LPF: low pass filter; BPF: band pass filter; AOM: acousto-optical modulator; SPD: single photon detector).

the BTC is locked via Pound-Drever-Hall technique to the reference beam described in fig. 4.1. A classical beam at 1436 nm, generated in the PPLN by difference frequency generation (DFG) of the pump beam at 426 nm and the reference beam at 606 nm, is used as reference to ensure the maximum transmission of the idler photons through the BTC. This lock of the DFG signal is operated by acting on the 426 nm pump frequency by changing the current sent to the laser diode. Two mechanical choppers are used to alternate between the locking period and the single-photon measurement, the duty cycle being about 45%. The photons of the pair are generated collinearly and separated after the BTC using a dichroic mirror (DM, fig. 4.3).

In order to achieve cavity enhancement, both signal and idler modes should be resonant with the BTC. However, as the two photons are widely-nondegenerate, only a few modes are doubly resonant (clustering effect [140, 106, 141]). At the cavity output the measured spectrum therefore consists of several (between 6 and 15, depending on the source) ultra-narrowband frequency modes in the main cluster separated by the cavity free spectral range. In Chapter 8 we characterize and store the whole spectrum of the photons described in section 4.3.2. In all the other demonstrations we operate in single-mode regime. To do so, the idler photons are sent through a homemade Fabry-Perot filtering cavity (FCav, linewidth 80 MHz, free spectral range 16.8 GHz), then coupled into a single mode fiber and sent to a SPD (InGaAs APD, ID230, IDQuantique, 10% efficiency and 10 Hz of dark-count rate). The FCav ensures a single-mode herald. The signal photons are filtered with an etalon, which suppresses

broadband noise and possible side clusters, and a bandpass filter (centered at 600 nm, linewidth 10 nm, Semrock) before being sent to the quantum memory. The heralding efficiency of both the sources, i.e. the probability to find a signal photon after the optical fiber conditioned on a detection in the idler channel, is $\eta_H^{\mathrm{SPDC}} \sim 25\%$ with a single frequency-mode idler. For the auto-correlation measurement of the idler photons, we use a second SPD (ID220, IDQuantique), with 10% efficiency and 400 Hz of dark-count rate.

4.3.1 CSPDC source 1

The first CSPDC source that was built in our lab is the project of the PhD thesis of Dr. Daniel Rielander. It was used for the experiment described in Chapter 5. All the details about this source can be found in [141]. The generated heralded signal is a Lorentzian with a linewidth of 2.8 MHz and a free spectral range of 423 MHz. To access its spectrum we compare two measurements:

• The temporal distribution of coincidences between the signal and idler photons of the source, shown in fig. 4.4(a), is taken from the data published in [141]. The correlation time of our heralded photons can be estimated by fitting the histogram with two exponential decays, as

$$\propto e^{-2\pi\,\Gamma_s\,t}\,\Theta(t) + e^{2\pi\,\Gamma_i\,t}\,\Theta(-t) + c_0,$$

where Γ_s (Γ_i) is the bandwith of the signal (idler) photon, $\Theta(t)$ is the heaviside function to distinguish the rising and falling exponentials related to the idler and signal photons, respectively, and c_0 is an offset [141]. The two decay times are different due to the different losses experienced in the cavity by the signal and the idler photons, generated at widely different frequencies. We can extract the linewidth of the signal (idler) photon to be $\Gamma_s = 3.7\,\mathrm{MHz}$ ($\Gamma_i = 2.3\,\mathrm{MHz}$). The resulting biphoton coherence time is $\tau_c = \frac{\ln 2}{2\pi\Gamma_s} + \frac{\ln 2}{2\pi\Gamma_i} = 78\,\mathrm{ns}$, from which we can calculate the biphoton linewidth as $\Gamma = \frac{\ln 2}{\pi\tau_c} = 2.8\,\mathrm{MHz}$ [141], being also the linewidth of the heralded single photons.

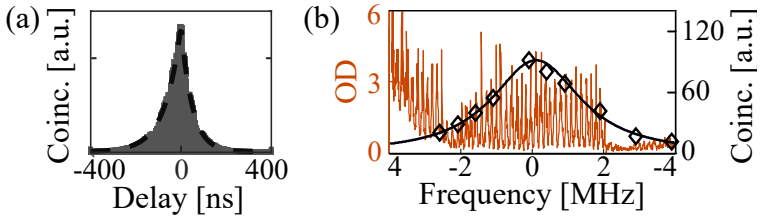

Figure 4.4: (a) Time-resolved coincidence histogram between signal and idler photons. The black dashed line is the temporal fit of the biphoton correlation. The data of this plot are taken from [141]. (b) A trace of a single-class AFC for $\tau = 7.3\,\mu$s (brown trace) tailored in the $\pm 1/2g \rightarrow \pm 3/2e$ transition is centered at 0 MHz[1]. The diamonds are signal-idler coincidence rates taken after the memory crystal used as a tunable spectral filter (preparing 800 kHz broad transparency windows at different frequencies). The error is smaller than the data points. The black line is a simulation of a Lorentzian peak with FWHM = 2.8 MHz convoluted with a 800 kHz-wide spectral hole.

• In a second experiment we employ the Pr^{3+}:Y_2SiO_5 memory crystal as a tunable frequency filter [142, 143, 24]. We prepare a 800 kHz-wide spectral hole. We record coincidence histograms between the idler detections and the signal photons passing through the crystal, while tuning the central frequency of the spectral hole by about 10 MHz around the frequency of the signal photons. The photons passing through the transparency window are directly steered to the APD for detection. The coincidence rate as a function of the hole position (black diamonds overlapped to the AFC in fig. 4.4(b)) gives a measure of the spectral distribution of the heralded single photons at 606 nm. The result of this measurement agrees with the spectrum extrapolated from the signal-idler coincidence histogram measured immediately after the SPDC source. This is confirmed by the good overlap between the diamonds and the black dotted line, which represents the convolution of a Lorentzian curve of width 2.8 MHz and the trace of the 800 kHz-wide spectral hole.

[1]The AFC absorption profile in our transition of interest, $\pm 1/2g \rightarrow \pm 3/2e$, occupies about 4 MHz. Other absorbing features on either side come from adjancent transitions. On its left side the $\pm 1/2g \rightarrow \pm 1/2e$ of the same class of ions (where a comb profile is present too) and other transitions of different classes of ions are probed. On the right side, for a single-class AFC, we can have two different situations: if the $\pm 3/2g$ ground state is kept empty during the AFC preparation, as in the present case or in fig. 5.3 and fig. 6.5, the atoms in that position belong to the $\pm 1/2g \rightarrow \pm 5/2e$ transition, where the comb is tailored too (the AFC feature in this transition looks smaller because of its lower dipole moment). Otherwise, for a non-empty $\pm 3/2g$ level, as in the case of the next section, namely fig. 4.5(b), or in fig. 6.8(c), we also interact with the $\pm 3/2g \rightarrow \pm 1/2e$ transition which is overlapped with the previous one.

4.3.2 CSPDC source 2

In the experiments described in Chapters 7 and 8, our heralded single photons are created with a new generation CSPDC source [144], which has been a project of the PhD student Dario Lago Rivera in our group. A longer BTC was built to decrease the linewidth of the generated biphoton to 1.8 MHz (FSR 261 MHz).

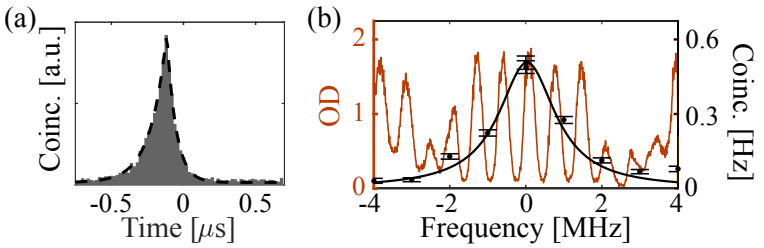

Figure 4.5: As in fig. 4.4. In (b) the transparency window prepared in the crystal is 1.6 MHz-wide (the measurement was performed in the waveguide type I described in Chapter 7).

We access the spectrum of the biphoton performing the same measurements as for the previous source, reported in fig. 4.5. From the right (left) decay of the coincidence histogram in fig. 4.5(a) we extract the linewidth of the signal (idler) photons to be $\Gamma_s = 2.5\,\text{MHz}$ ($\Gamma_i = 1.4\,\text{MHz}$). The resulting biphoton coherence time is 121 ns.

4.4 AFC experimental preparation

The storage protocol used in all our experiments is the atomic frequency comb (AFC) technique explained in detail in sec. 3.3. In this section I describe the general experimental procedure that we follow to generate our AFCs in Pr^{3+}:Y_2SiO_5 . We always prepare single-class AFC features in the $|g\rangle$-$|e\rangle$ transition (see fig. 4.6(a)). When spin-wave storage is performed we keep the $|s\rangle$ state empty. The timings given to the different parts of the pulse sequence will vary, as well as the powers used and the repetitions. I will recall shortly the main differences chapter by chapter.

We start by preparing a 4 MHz-broad single-class-populated $1/2_g - 3/2_e$ transition. The theoretical description and detailed explanation of the approach that we use can be found in section 3.2.2.

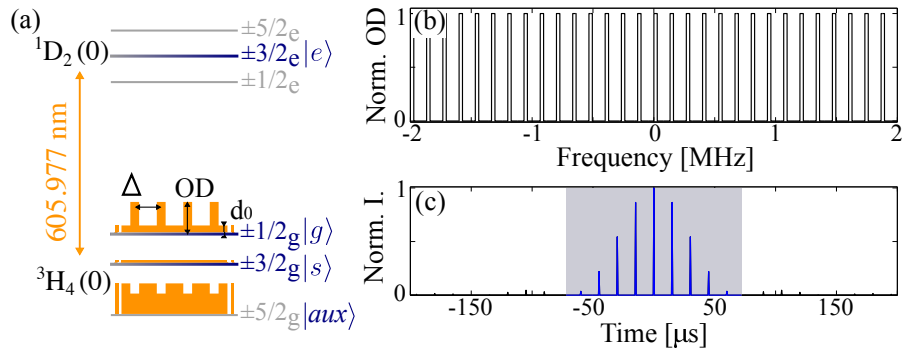

Figure 4.6: (a) Level scheme of the transition of interest in Pr^{3+}:Y_2SiO_5. The atomic populations of the three ground states after the AFC preparation are sketched in orange. (b) Example of desired atomic frequency comb, with optimized finesse; (c) pulse train obtained by performing the Fourier transform of the comb shown in panel (a). The shaded rectangle shows the principal part of the waveform that we select.

We create the comb structure using a procedure inspired by [27]: we simulate the desired comb (an example being shown in fig. 4.6(b)), deciding the shape of the peaks (square), fixing the optical depth (OD) and the background optical depth (d_0), and calculating the best finesse for each particular AFC storage time (τ). We perform the Fourier transform of the simulated comb. In this way we generate a temporal sequence of pulses (blue line in fig. 4.6(c)) containing all the spectral information of the desired AFC. This optical pulse train, fixed in frequency to the $|g\rangle$-$|e\rangle$ transition, would generate, ideally, the AFC of fig. 4.6(b). We modulate the laser light temporally according to this temporal function, using a double-pass AOM (see fig. 4.1). To maintain the duration of the preparation within the limit imposed by the cryostat cycle, we consider only the principal part of the Fourier transform, as highlighted in fig. 4.6(c) by the shaded rectangle (the temporal part considered varies from one experiment to the other, as well as the desired AFC parameters used, which we kept optimizing throughout my PhD thesis). This pulse is finally renormalized for the non-linear response of the double-pass AOM. We optically pump the $|g\rangle$-$|e\rangle$ transition with this pulse train many times (about 1000 times, but different for each storage time and for the different experiments described in the following chapters).

If we want to perform spin-wave storage, parallely to the comb preparation, we keep emptying $|s\rangle$ (see fig. 4.6(a)) with optical pulses resonant with the

$|s\rangle$-$|e\rangle$ transition and chirped by $\sim 5\,\mathrm{MHz}$. We want this spin-state to be as empty as possible, in order to reduce the noise generated by the control pulses (CPs) in the temporal window of the spin-wave echo.

Chapter 5

Spin-wave storage of heralded single photons

In this chapter we demonstrate a building block for a quantum repeater link (see fig. 5.1), performing spin-wave (SW) storage with on-demand retrieval of heralded single photons with a telecom heralding. This is achieved in a Pr^{3+}:Y_2SiO_5 crystal using the full atomic frequency comb (AFC) scheme described in sec. 3.3.1. Pairs of non-degenerate single photons are generated one resonant with an optical transition of Pr^{3+}:Y_2SiO_5 and the other at telecom wavelength (the source is the PhD project of Dr. D. Rielander, see sec. 4.3.1). The telecom photon is used to herald the presence of the signal photon, which is stored as a spin-wave in the crystal and retrieved on demand after a controllable time. We measure second-order cross correlation values between the heralding and the retrieved photons, which exceed the classical bound fixed by the Cauchy-Schwarz inequality for storage times longer than 30 μs, effectively demonstrating quantum correlations

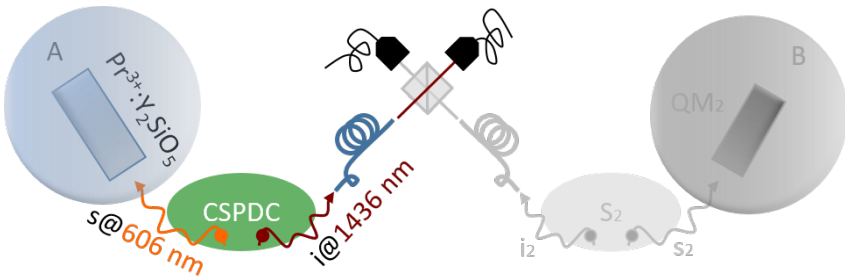

Figure 5.1: Sketch of the performed experiment in a possible quantum repeater link

between telecom photons and single spin waves in a solid. Moreover we demonstrate that our memory can store spin-waves in multiple independent temporal modes.

The results of this experiment were published in Physical Review X [28] and also featured in Physics as a ViewPoint by J. Nunn [145]. The content of this chapter is mostly taken from the paper and its supplementary material.

5.1 Introduction

Most protocols for long distance quantum communication require quantum memories connected to communication channels through fibers. One possible direction is to use telecom quantum memories, e.g. based on erbium doped solids [146, 39] or optomechanical systems [147]. However, the most efficient and long lived storage systems up to date are working at wavelengths far from the telecom window, leading to large loss in optical fibres. Possible solutions to overcome this problem include quantum frequency conversion [148, 57, 101, 149, 48, 150] or non-degenerate photon pair sources to establish entanglement between quantum memories and telecom photons [19]. The latter approach has been demonstrated using the atomic frequency comb scheme [68] in rare earth doped single crystals or waveguides [22, 23, 107], but the storage of photonic entanglement was performed so far only in the excited state for short and pre-determined storage times.

Longer and programmable storage times can be obtained by transferring the optical atomic excitations to long lived spin collective excitations (spin waves) using control laser pulses (see sec. 3.3.1). Recently, spin wave storage of weak coherent states at the single photon level [24, 90], including time-bin qubit and polarization qubit storage [24, 44], has been demonstrated with rare-earth doped crystals. The generation and storage of continuous variable entanglement between a multimode solid-state quantum memory and a light field has also been reported recently [59]. In this experiment, light-matter entanglement was created within the memory between spontaneously emitted light and spin waves, the latter then being converted into a light field. This is an emissive quantum memory [16] with the generated light fields being, for this demonstration, outside

the telecommunication band. This motivates the need for an absorptive quantum memory that can store an externally prepared quantum optical state that shares a quantum correlation with a telecom band photon (see sec. 1.2.2).

The demonstration of such a quantum memory with single photons requires an efficient quantum light source matching the spectral properties of the quantum memory [106, 141], and the quasi-suppression of the noise generated by the strong control pulses. These tasks are challenging due to the small spectral separation between the hyperfine states of the optically active ions (a few MHz in our system). We show here that we could achieve this goal, demonstrating for the first time an on-demand spin-wave solid-state quantum memory for telecom-heralded single photons.

5.2 Experimental details

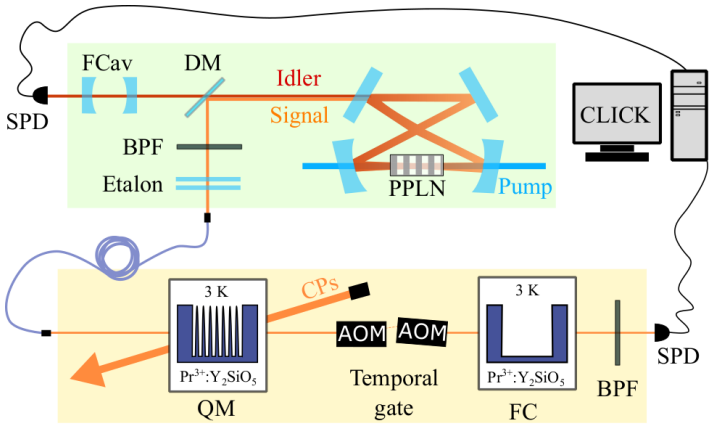

Figure 5.2: The photon pairs are generated by CSPDC with a setup similar to fig. 4.3 (sec. 4.3). The optical path of the preparation light and the control pulses (CPs) is aligned at an angle of $\sim 3°$ with respect to the input photons and is counter propagating to them. The retrieved single photon is spectrally filtered using a filter crystal (FC) before being detected by a Silicon SPD. Temporal filtering is achieved with acousto-optic modulators, placed after the memory crystal and opened only when we expect the SW echo.

Fig. 5.2 depicts the experimental setup. A single-class atomic frequency comb (AFC) is prepared, following the spectral hole burning procedure described in section 3.2.2, at the frequency of the $1/2_g - 3/2_e$ transition (the level scheme of interest is reported in fig. 2.2). To perform SW storage, an

optical control pulse drives the coherence from the $3/2_e$ state to the empty $3/2_g$ state (the spin-state $|s\rangle$). The beam for memory preparation and control pulses (with a maximum power of 21 mW) has a waist of 175 μm (bigger than the 45 μm of the single photons path), and is sent with a small angle with respect to the photons (about 3°) and counter propagating. In this way we can spatially filter out some noise generated by the control pulses. In [119], where the CPs were co-propagating with the stored and retrieved light and with an angle between the beams of only 1.5°, the extinction ratio of this spatial filter was of 10^{-5}. The narrow-band spectral filtering of the noise resulting from the control pulses is accomplished with a second Pr^{3+}:Y_2SiO_5 crystal, the filter crystal FC, where a 5.5 MHz-broad transparency window is burnt at the frequency of the AFC [24]. An example of AFC prepared in the memory crystal overlapped with the narrow spectral hole burnt in the filter crystal is reported in fig. 5.3. The actual shape of the comb peaks is Gaussian rather than square, due to power broadening. Between the memory and the filter crystal we add a fast temporal gate composed of two AOMs. This prevents additional holeburning in the filter crystal and the SPD from being blinded by a possible leakage of the control pulses. Then, the retrieved photons pass through a band-pass filter (centered at 600 nm, linewidth 10 nm, Semrock) and are sent to an SPD through a single mode fiber.

Our CSPDC source, described in section section 4.3, produces ultra-narrow photon pairs where one photon, the idler, is in the telecom E-band at 1436 nm, and the other is resonant with the Pr^{3+} optical transition at 606 nm, specifically with the transition where the AFC is prepared [106, 107]. The pump at 426.2 nm is kept at the average power of 3.3 ± 0.5 mW for the measurements presented in this chapter. The probability to obtain a single signal photon in front of the quantum memory conditioned on a detection in the idler SPD (i.e. the heralding efficiency) is $\eta_H = (20.9 \pm 0.5)\%$.

To prepare the AFC we use the technique described in section 4.4. During the preparation of the memory crystal, the SPDs of both idler and signal arms are gated off. After each AFC preparation, the gates are opened and we detect the arrival time of both photons of the pair during a measurement time of about 100 ms, leading to a memory duty-cycle of 14%.

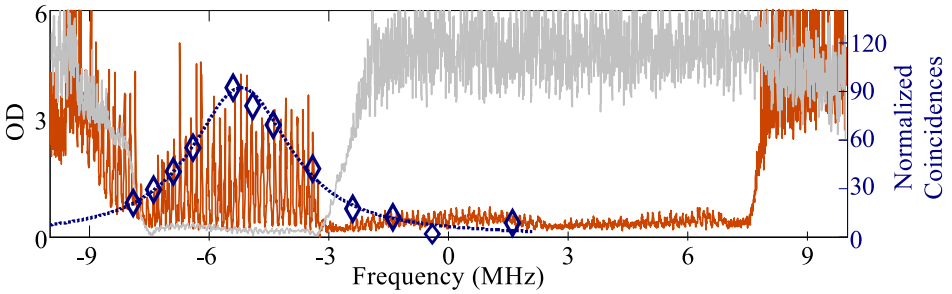

Figure 5.3: AFC for $\tau = 7.3\,\mu$s (brown trace). The light gray trace is the transparency window that we burn in the filter crystal. The diamonds are signal-idler coincidence rates taken after the memory crystal used as a tunable spectral filter (preparing 800 kHz broad transparency windows at different frequencies). The error is smaller than the data points. The dotted blue line is a simulation of a Lorentzian peak with $FWHM = 2.8$ MHz convoluted with a 800 kHz-wide spectral hole.

Further details about the experimental setup and the preparation of the AFC feature can be found in Chapter 4.

In order to reduce the noise generated by the CPs during the spin-wave storage, we send 100 CPs separated by 25 μs after the preparation of the comb and, afterwards, another 50 with a separation of 100 μs. If these *cleaning* CPs are too close to each other the atoms are coherently driven between the ground and the excited state and some might remain in the former.

5.3 Spin-wave storage of heralded single photons

The heralded single photons that we want to store have a Lorentzian spectrum with a linewidth of 2.8 MHz (see section 4.3.1). The spectrum of the biphoton, shown in fig. 5.3 as a blue trace, matches with the prepared AFC structure, brown trace. We estimate the spectral overlap between the heralded single photons and the AFC to be about 66 %, which limits the AFC storage efficiency in this experiment. The correlation between the idler and signal photons is inferred by measuring the normalized second-order cross-correlation function, $g^{(2)}_{s,i}$, in a time window $\Delta t_d = 320$ ns (see sec. 1.4.1). This is extracted from coincidence histograms, constructed by taking the detection of the idler photons as a start and the detection of

signal photons as stop. Before the memory we measure $g^{(2)}_{s,i}(\Delta t_d) = 57 \pm 1$ (pump power 3.4 mW).

Spectral *pit*

We first prepare in the memory crystal a 18 MHz-wide transparency window (spectral *pit* of sec. 3.2.2). We measure the coincidence histogram when the signal photons are sent through the spectral *pit* (blue input trace in fig. 5.4(a)). The correlation time between the signal and idler photon, measured by fitting their coincidence histogram with a double exponential decay as explained in sec. 4.3, is $\tau_c = (89 \pm 4)$ ns, leading to a heralded photon linewidth of (2.5 ± 0.1) MHz [141]. The measured $g^{(2)}_{s,i}(\Delta t_d)$ value is 96 ± 32[1].

AFC

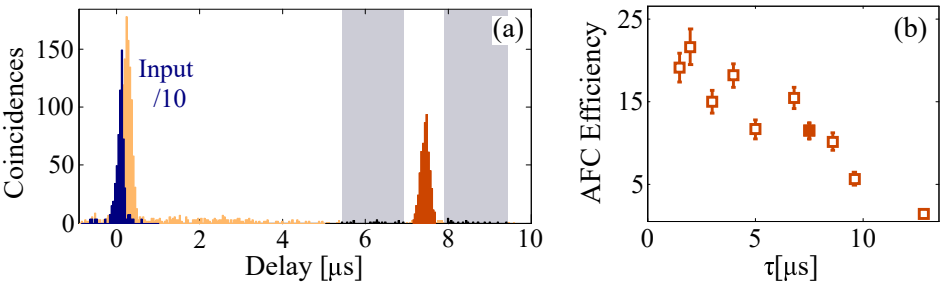

Figure 5.4: (a) Time histograms of the input photons (dark blue trace peaked at 0 μs) and the AFC echo (brown trace, including the transmitted signal in light orange). The shaded rectangles mark the areas used to measure the uncorrelated noise in the calculation of the $g^2_{AFC,i}$ value. The transmitted part of the input photon is delayed due to slow-light effects when interacting with the features shown in fig. 5.3. (b) AFC storage efficiency for different storage times, τ. The filled square is $\tau = 7.3\,\mu$s, whose coincidence histogram is shown in panel (a).

Then we prepare a single-class AFC (fig. 5.3), following the approach described in sec. 4.4, obtaining, for a pre-programmed storage time $\tau = \frac{1}{\Delta} = 7.3\,\mu$s, an efficiency $\eta_{AFC} = (11.0 \pm 0.5)\,\%$ and $g^{(2)}_{AFC,i}(\Delta t_d) = 130 \pm 31$. The signal and the uncorrelated coincidences used to measure the $g^{(2)}_{AFC,i}$ are, respectively, the brown echo at about τ and the gray rectangles around

[1] This value increases after transmitting the signal photon through the pit because part of the uncorrelated signals that are measured with just the source are filtered by the memory crystal.

it (i.e. the stored signal and the stored noise) in fig. 5.4(a). The efficiency is extracted from the coincidence histogram by dividing the counts in the AFC echo window by the number of expected photons in front of the memory. Figure 5.4(b) shows the AFC efficiencies achieved for different storage times τ, the filled square being the efficiency at $\tau = 7.3\,\mu$s.

The shown $g^{(2)}_{AFC,i}$ represents an improvement by more than one order of magnitude compared to the state of the art in the same system [107]. The $g^{(2)}_{s,i}$ value increases after the AFC storage due to the fact that the stored photons are transferred to a temporal mode free of noise (as the pump laser of the CSPDC is switched off upon the detection of the idler photon) [107]. After the retrieval, we measure $\tau_c = (147 \pm 7)\,$ns, larger than the value measured before storage. We attribute this temporal stretching to spectral mismatch between the input photons before the memory (FWHM = 2.8 MHz) and the atomic frequency comb (total width 4 MHz), as highlighted in fig. 5.3.

SW storage

We then perform SW storage experiments (sec. 3.3.1) by sending pairs of strong control pulses after the detection of each heralding photon. The control pulses, detected with a reference photodetector, are displayed in fig. 5.5(a) as plain pulses and are separated by $T_s = 6\,\mu$s. They are modulated in amplitude and frequency with Gaussian and hyperbolic tangent waveforms, respectively, as described in the Appendix A.1. Their peak power is 21 mW.

In the coincidence histogram of fig. 5.5 we observe a SW echo at 13.3 μs, as expected from τ and T_s. The efficiency of our quantum memory, $\eta_{sw} = (3.6 \pm 0.2)\,\%$, is inferred with a coincidence window of $\Delta t_d = 320\,$ns, containing 80 % of the signal (see Appendix A.3) and including the loss induced by the filter crystal. Fig. 5.5(b) shows a magnification of the SW echo, normalized by the average value of the noise measured outside the peak. This plot quantifies the signal-to-noise ratio (SNR) of the stored and retrieved photon in each bin and could be used to infer $g^{(2)}_{swe,i}$ (that will be measured accurately in the next section). We observe a maximum SNR of around 5. With our filtering strategy we reach a noise floor of $(2.0 \pm$

$0.1) \times 10^{-3}$ photons per storage trial at the memory crystal[2] (horizontal dashed line in the SW echo temporal mode). The correlation time of

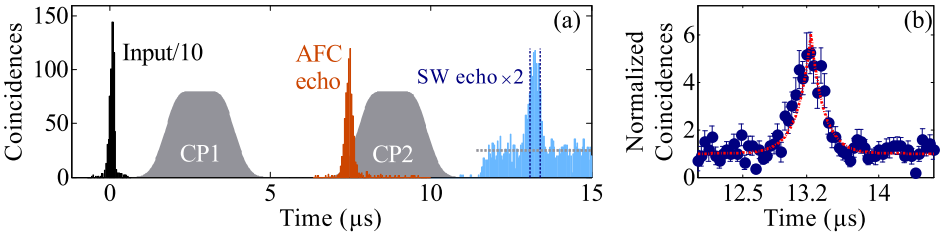

Figure 5.5: (a) Time histograms of the input photons (black trace), the AFC echo at $\tau = 7.3\,\mu$s (brown trace), and the SW echo (blue trace) acquired over an integration time of 343 min. The coincidence count rate in the AFC echo is 4/min and in the SW echo ≈ 1/min. The control pulses are shown in gray. The dashed vertical lines indicate the coincidence window for the signal ($\Delta t_d = 320$ ns), while the dashed horizontal line represents the noise floor. (b) Coincidence counts for the SW echo at $T = \tau + T_s = 13.3\,\mu$s normalized by the average noise level, along with its fit to a double exponential function, to account for the Lorentzian spectral shape of the SPDC photons.

$\tau_c = (200 \pm 40)$ ns exceeds the one after storage in the excited state. This further increase after the SW storage is attributed to the limited frequency spanned by the control pulses (called chirp).

5.4 Quantum correlation between single telecom photons and single spin waves

To investigate the non-classical nature of the photon correlation after the SW storage, we measure $g^{(2)}_{swe,i}(\Delta t_d)$ and compare it to the unconditional autocorrelation of the idler ($g^{(2)}_{i,i}(\Delta t_d)$) and retrieved signal ($g^{(2)}_{swe,swe}(\Delta t_d)$) fields (see sec. 1.4.2). To access these quantities we perform a measurement in which we store photons unconditioned on the detection of heralding photons. This sequence is sketched in fig. 5.6. After the preparation of the memory, we perform 500 storage trials, separated by 190 μs. We choose this time, longer than the relaxation time of the excited state, in order to reduce accumulated noise from the CPs in the SW echo mode due to the multiple storage trials. Each storage trial consists of two transfer pulses, the write (CP1) and the read (CP2), separated by $T_s = 6\,\mu$s. The gate of

[2] The noise floor measures the number of noise counts detected in a coincidence window Δt_d, back-propagated to the output of the memory.

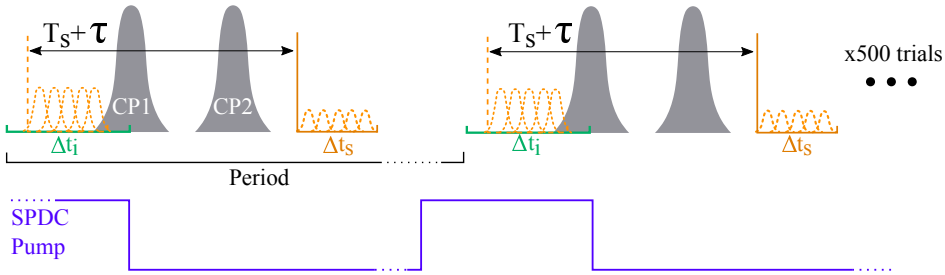

Figure 5.6: Unconditional sequence: storage of single photons not conditioned on the detection of the heralding photon. The blue line shows the voltage sent to the AOM in front of the SPDC cavity, thus the switching on and off of the pump laser.

the idler detector is opened for a time $\Delta t_i = 6\,\mu$s and it closes when the write pulse arrives to its maximum intensity. For this measurement, we assemble a Hanbury-Brown Twiss setup after the memory (splitting the signal photon with a fiber BS at the detection stage) such that we can reconstruct both the cross-correlation $g^{(2)}_{swe,i}$ between the retrieved photons and the heralding photons and the auto-correlation of the retrieved photons $g^{(2)}_{swe,swe}$. The two detectors of the signal are switched on $1.3\,\mu$s after the read pulse and are maintained open for a time $\Delta t_s = 4.5\,\mu$s. Together with the closing of the idler gate, an RF-signal is sent to the AOM of the pump laser of the source in order to keep it off for $30\,\mu$s during the detection of the signal photons (purple line in fig. 5.6).

We reconstruct the $g^{(2)}_{swe,i}$ value as the ratio between the coincidences detected at a storage time $\tau + T_S = (7.3 + 6)\,\mu$s $= 13.3\,\mu$s within the same storage trial and the average of the coincidences between signal and idler photons detected in the spin wave temporal mode of the 20 neighboring storage trials (fig. 5.7(a)). In both cases the integration window is 320 ns. We find $g^{(2)}_{swe,i} = 6.1 \pm 0.7$. We note that our $g^{(2)}_{swe,i}$ is limited by the SW read-out efficiency, that we estimate to be approximately $\eta_R = 24\,\%$, while the write efficiency is $\eta_W = 31\,\%$ (see Appendix A.2 for a detailed discussion).

The classical bound from the Cauchy-Schwarz inequality $g^{(2)}_{swe,i} < \sqrt{g^{(2)}_{swe,swe} \cdot g^{(2)}_{i,i}}$ is indicated in fig. 5.7(a) as a horizontal line (see sec. 1.4.3). We build the coincidence histogram between the signal photons at the two outputs of the fiber (BS) considering the whole detection window, as the signal

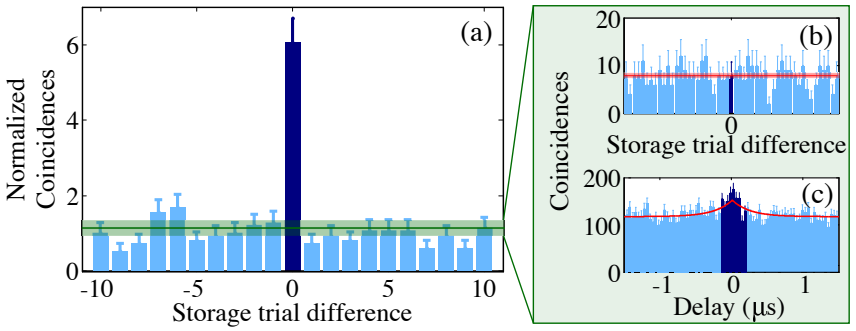

Figure 5.7: (a) Unconditional cross-correlation between the idler photons and the retrieved signal photons. All the coincidences are normalized to the average value of the noise counts (storage trial difference $\neq 0$). The $g^{(2)}_{swe,i}$ value for this measurement is 6.1 ± 0.7. The classical bound given by the Cauchy-Schwarz inequality is reported as a horizontal line. The error bars are calculated considering Poissonian statistics. (b) Second-order autocorrelation histogram of the stored and retrieved single photons $g^{(2)}_{swe,swe}$. The darker bar indicates the coincidence counts in a window $\Delta t_d = 320\,\text{ns}$ about 0 delay in the same storage trial. The red line is the average of the counts with storage trial difference $\neq 0$. (c) Second-order autocorrelation time-resolved histogram of the idler photons measured in CW configuration. The region marked with darker bars indicate the coincidence window $\Delta t_d = 320\,\text{ns}$. The red line is a double exponential fit of the histogram.

can arrive everywhere in Δt_s thanks to the multimodality of the AFC protocol. We calculate $g^{(2)}_{swe,swe}$ as the ratio of the coincidences between the signal detections in the same storage trial and the coincidences in the 20 neighbouring storage trials [151, 141]. We consider a coincidence window $\Delta t_d = 320\,\text{ns}$ around $0\,\mu\text{s}$ delay, to be consistent with the cross-correlation measurement. The result is shown in fig. 5.7(b) and the value that we extract is $g^{(2)}_{swe,swe}(320\,\text{ns}) = 1.0 \pm 0.4$. The large error bar is due to the low statistics. This value is remarkably lower than expected for a thermal state produced by a SPDC process [94] (sec. 1.4.2). This is, mainly, a consequence of the noise produced by the storage protocol. As the noise is not bunched, the higher is the level of noise, the closer to 1 the $g^{(2)}_{swe,swe}$. In fact, in an unconditional measurement, the probability to detect a retrieved signal photon over the probability to detect a noise count is very low, being $\text{SNR}^{unc} = (P_{swe} - P_n)/P_n = 0.030 \pm 0.003$. The finite coincidence window also contributes to decrease the autocorrelation [141].

The unconditional autocorrelation for the idler photons is measured in a CW configuration (without gating), as no storage is involved [141]. A

typical measurement for a pump power of 4.3 mW is shown in fig. 5.7(c) from which we calculate a value of $g^{(2)}_{i,i}(320\,\text{ns}) = 1.32 \pm 0.04$.

5.4.1 Cauchy-Schwarz R-parameter

To confirm the quantum correlation between the idler and the retrieved SW echo, we calculate the Cauchy-Schwarz parameter $R = \frac{(g^{(2)}_{swe,i})^2}{g^{(2)}_{swe,swe} \cdot g^{(2)}_{i,i}}$ (see sec. 1.4.3). Using the measured values reported before, we calculate $R = 28 \pm 12$, which exceeds the classical benchmark of 1 by more than two standard deviations. The sizable errorbar is due to the low statistics in the second-order autocorrelation measurements of the retrieved signal photons, $g^{(2)}_{swe,swe}$. Considering a wider coincidence window for the auto- and cross-correlation value calculation, e.g. $\Delta t_d = 1\,\mu$s, the uncertainty decreases due to better statistics (the auto- and cross-correlation values also decrease due to the bigger contribution of uncorrelated noise). Nonetheless, the Cauchy-Schwarz inequality is violated by more than 3 standard deviations, as shown in Table 5.1.

Δt_d	320 ns	1 μs
$g^{(2)}_{swe,swe}$	1.0 ± 0.4	1.1 ± 0.2
$g^{(2)}_{i,i}$	1.32 ± 0.04	1.14 ± 0.02
$g^{(2)}_{swe,i}$	6.1 ± 0.7	3.1 ± 0.3
R	28 ± 12	8.3 ± 2.3

Table 5.1: Second-order auto- and cross-correlation values of idler and retrieved signal photons as obtained from the experimental histogram when considering different coincidence windows. The corresponding Cauchy-Schwarz parameters R are also reported.

The confidence level for the measured Cauchy-Schwarz inequality violation, i.e. for observing a non-classical correlation between the telecom heralding photon and the single SW stored in the crystal, is 98.8 % if we consider a window $\Delta t_d = 320\,\text{ns}$. If a larger coincidence window is considered, $\Delta t_d = 1\,\mu$s, the R value is reduced, but the confidence level for the demonstration of non-classical correlation rises up to 99.92 %.

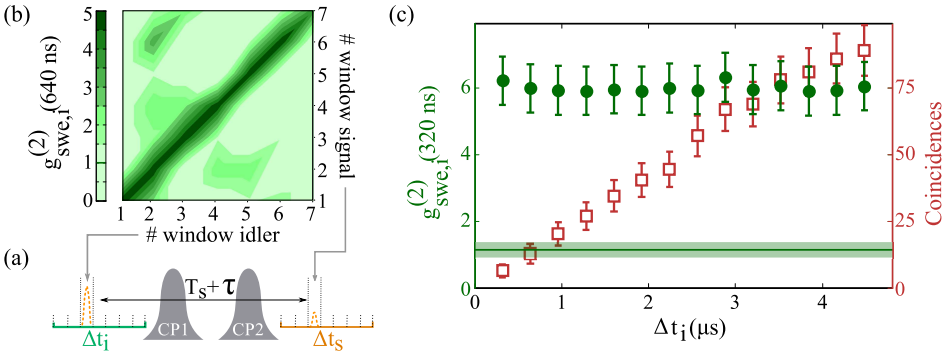

Figure 5.8: (a) Scheme representing the analysis of the cross-correlation measurement to evidence the multimodality. Both idler and retrieved signal detection windows are divided into many intervals of 640 ns. The correlation is calculated between the different intervals. (b) Cross-correlation value between idler and retrieved signal photons, each of them measured in different temporal intervals. The $g^{(2)}_{swe,i}$ exceeds the classical threshold only for windows separated by the total storage time $T = 13.3\,\mu$s (same # window in both idler and signal). (c) Cross-correlation value between the idler photons and the retrieved signal photons (full circles) and the coincidence counts in the SW echo (empty squares) as a function of the detection window for the idler photons (considering the full signal list). The classical threshold is also reported as a horizontal line. The integration time for this measurement is 38.5 h. The error bars are calculated considering Poissonian statistics.

5.4.2 Temporal multimodality

The main advantage of the full AFC protocol is the multimode storage. In our case we show the possibility to store multiple distinguishable temporal modes, while maintaining their coherence and quantum correlation [68]. This ability is crucial for applications in quantum information protocols, e.g. to enable temporally multiplexed quantum repeater protocols with high communication speed [19] and storage of time-bin qubits robust against decoherence in optical fibers. To test this aspect, we perform experiments with detection gates much longer than the photons duration. We divide both the idler and the retrieved signal detection windows into many temporal modes of width 640 ns (longer than what considered in the former analyses in order to have better statistics), as sketched in fig. 5.8(a). We then check that we have non-classical correlations between modes separated by the total storage time $T = T_s + \tau = 13.3\,\mu$s and classical correlations between modes separated by $T \neq 13.3\,\mu$s, as shown in fig. 5.8(b). Contrarily to other temporally multimode storage protocols

[65, 152, 59], in the full AFC protocol the total storage time is maintained for the different temporal modes (see sec. 3.3). With $\Delta t_d = 640\,\text{ns}$, containing the 94 % of the coincidence peak (as shown in appendix A.3), we confirm non-classical storage of 7 temporal modes (each interval of fig. 5.8(b)). However, considering $\Delta t_d = 320\,\text{ns}$, which still contains the 80 % of the SW echo, a 4.5 μs-wide gate can accommodate up to 14 independent temporal modes.

To additionally demonstrate that the multimode capacity does not imply any increase of the noise, we compute $g^{(2)}_{swe,i}$ for idler gate windows varying from 320 ns to 4.5 μs, as shown in fig. 5.8(c) (full circles) together with the coincidence counts measured in the center peak for each window size (empty squares). As expected, the latter increases with increasing idler gate window but the $g^{(2)}_{swe,i}$ value remains constant, within the error bar, and well above the classical bound over the whole range.

5.4.3 Different storage times

Finally, to illustrate the ability to read-out the stored spin wave on demand, we perform storage experiments at different SW storage times. For these measurements, we implement a semi-conditional storage sequence in order to obtain good statistics with shorter integration time.

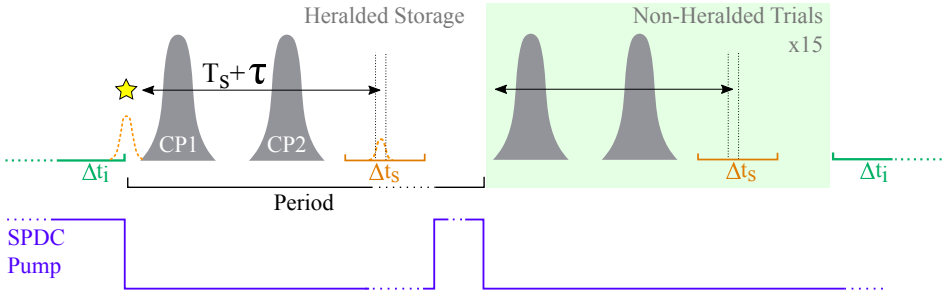

Figure 5.9: Semi-conditional sequence: storage of single photons conditioned on the detection of the heralding photon. After each conditional storage we perform 15 other unconditional storage trials. The blue line shows the voltage sent to the AOM in front of the pump, thus the switching on and off of the pump laser.

In this sequence, sketched in fig. 5.9, after the preparation of the memory we open the idler gate and continuously check for heralding events (every 80 ns). Each time that we detect an idler photon we close the gate of

the telecom detector, we switch off the SPDC pump (for 40 μs), and we start the SW storage cycle. As for the unconditional case, after the second control pulse CP2, the signal gate is opened for a time Δt_s (see fig. 5.9) to detect the retrieved photon. To estimate the noise, after the retrieval we send 15 pairs of CPs (unconditional) with a period of 190 μs.

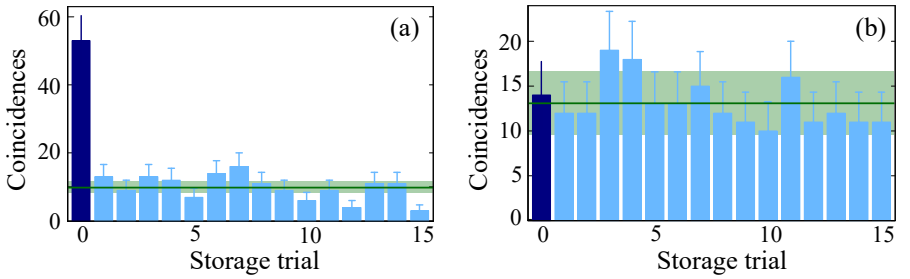

Figure 5.10: (a) Cross-correlation measurement for a spin wave storage $T_s = 6\,\mu$s, using the semi-conditional sequence: the bar at 0, in dark blue, represents the sum of the coincidences in a 320 ns window placed $\tau + T_s = 13.3\,\mu$s after the heralding photon. The other bins represent coincidences (for the same coincidence window size and position) between the heralding and signal detections in the following 15 storage trials, the green line being the average value and the green shaded area the standard deviation. (b) Cross-correlation measurement of the noise using the semi-conditional sequence, as (a) but blocking the signal photons in front of the quantum memory.

We calculate the $g^{(2)}_{swe,i}$, as in the unconditional sequence (sec. 5.4). The uncorrelated noise is estimated from the average of the coincidences in the following 15 storage trials. The resulting coincidence histogram is reported in fig. 5.10(a), to be compared with the unconditional coincidence histogram shown in fig. 5.7(a). The $g^{(2)}_{swe,i}$ for the semi-conditional measurement is 5.0 ± 0.3. Note that in the same conditions (pump power and storage time), the semi-conditional sequence provides a slightly lower $g^{(2)}_{swe,i}$ value, mainly due to the higher noise floor, $(2.0 \pm 0.1) \times 10^{-3}$, with respect to the unconditional sequence ($(1.3 \pm 0.1) \times 10^{-3}$ photons per storage trial). We attribute this result to the fact that the number of control pulse pairs per comb is larger in the unconditional sequence. This probably contributes to a further emptying of the spin storage state. We also repeated the same measurement while blocking the signal photons before the quantum memory with a beam block. In this way we can measure the cross-correlation of the noise, which is $g^{(2)}_{n,i}(320\,\text{ns}) = 1.1 \pm 0.3$ ($g^{(2)}_{n,i}(3\,\mu\text{s}) = 1.0 \pm 0.1$), as shown in fig. 5.10(b). As previously discussed, the biggest contribution to the signal unconditional autocorrelation is given by the noise (see sec. 5.4) and

that this is not bunched. Thus, any modification in the measurement that increases the noise (e.g. the use of the semi-conditional sequence), would only further approach the autocorrelation to the value of 1, thus lowering the classical threshold. For simplicity we will consider the measured unconditional autocorrelation of the signal.

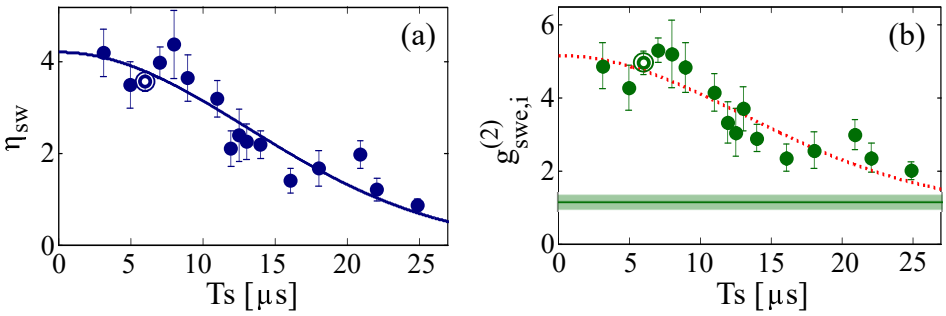

Figure 5.11: (a) Spin-wave storage efficiency as a function of the storage time T_s. The solid line is a fit of the experimental data taking into account a Gaussian inhomogeneous broadening of the spin state. The spin inhomogeneous broadening extracted from the fit is $\gamma_{inh} = (20 \pm 3)$ kHz. (b) $g^{(2)}_{swe,i}(320\,\text{ns})$ value as a function of the storage time. The classical threshold is reported as horizontal line. In both panels, the error bars are calculated considering Poissonian statistics and the circled data points refer to the measurement reported in fig. 5.10.

This sequence has been employed to measure $g^{(2)}_{swe,i}$ for different T_s. The storage and retrieval efficiencies, measured dividing the counts in the *swe* by the estimated input before the memory, are reported in fig. 5.11(a). A Gaussian fit, blue line, accounts for the inhomogeneous broadening of the spin-state (see section 3.3.1). As a fitting parameter we obtain the spin inhomogeneous linewidth $\gamma_{inh} = (20 \pm 3)$ kHz, in good agreement with what was measured in different experiments on the same crystal [24, 137]. This further confirms that the photons are stored as spin waves. The measured second-order cross-correlation function $g^{(2)}_{swe,i}$ for increasing SW storage times T_s is shown in panel (b) of fig. 5.11. The red dashed curve is the expected behaviour for the SNR. It is calculated by considering the Gaussian fit of the signal decay (solid curve in panel (a)), normalized by the source heralding efficiency η_H and the average noise floor of $(1.9 \pm 0.2) \times 10^{-3}$ photons per trial (averaged over the different T_s). We measure non-classical correlations between the idler and the retrieved signal photons up to a total storage time $T = \tau + T_s = 32.3\,\mu$s. Note that,

while we measure the Cauchy-Schwarz parameter R for $T = 13.3\,\mu$s, to assess the non-classicality for longer storage times we make the assumption that the retrieved signal autocorrelation does not change with the storage time. This is a conservative estimate, since the $g^{(2)}_{swe,swe}$ value is mainly determined by the noise in the read-out, that we verify to be constant over the whole range of storage times investigated. Under this hypothesis, the Cauchy-Schwarz inequality is violated at $T = 32.3\,\mu$s with a confidence of 94 % for $\Delta t_d = 320\,$ns.

5.5 Discussion and conclusion

We have reported the first demonstration of quantum storage of heralded single photons in an on-demand solid state quantum memory. We have shown that the non-classical correlations between the heralding and the stored photons are maintained after the retrieval, thus demonstrating non-classical correlations between single telecom photons and single collective spin excitations in a solid. Finally we showed that the full atomic frequency comb protocol employed allows storing single photons in multiple independent temporal modes. These results represent a fundamental step towards the implementation of quantum communication networks where solid state quantum memories are interfaced with the current fiber networks operating in the telecom window [19].

The demonstrated quantum correlation between a telecom photon and a spin wave in a solid is an essential resource to generate entanglement between remote solid state quantum memories [19]. The measured value of $g^{(2)}_{swe,i}$ after spin wave storage is currently limited by the signal-to-noise ratio of the retrieved photon, which is in turn mostly limited by the low storage and retrieval efficiency. This could be greatly improved by using a higher optical depth [65] with higher quality combs, or crystals in impedance matched cavities [76, 153]. The storage time is currently limited by the spin inhomogeneous broadening and could be increased using spin-echo and dynamical decoupling techniques [90], with prospect for achieving values up to one minute [72] in our crystal, while even longer storage times (of order of hours) may be available in Eu^{3+}:Y_2SiO_5 [154]. Finally our experiment could be extended to the storage of entangled qubits, e.g. in time-bin [24].

Chapter 6

Integrated optical memory: *Type II* waveguide

In this chapter I report on the first realization of an integrated optical memory for light based on a laser-written waveguide in a rare-earth doped crystal. This project was done in collaboration with Dr. Roberto Osellame and Dr. Giacomo Corrielli of Politecnico di Milano. The waveguides were fabricated by them in a Pr^{3+}:Y_2SiO_5 crystal using femtosecond laser micromachining. The guiding properties were characterized mostly in their lab, while we performed optical characterization and storage experiments. We demonstrated that the waveguide inscription does not affect the coherence properties of the material and that the light confinement in the waveguide increases the interaction with the active ions by a factor of 6. We also demonstrated that, analogously to the bulk crystals, we can operate the optical pumping protocols necessary to prepare the population in atomic frequency combs, that we used to demonstrate light storage both in the excited and in the spin state of praseodymium ions. These results represent the first realization of laser written waveguides in a Pr^{3+}:Y_2SiO_5 crystal and the first implementation of an integrated on-demand spin-wave optical memory, opening new perspectives for integrated quantum memories.

Most of the following results are published in Phys. Rev. Applied [137], selected as editor suggestion. The content of this chapter is mostly taken from the paper. Some unpublished measurements taken on new waveguides type II fabricated in a different sample are reported at the end of the chapter.

6.1 Introduction

In order to progress towards large scale quantum information architectures involving several quantum memories (QMs), it is important to rely on devices that can be easily duplicated and integrated. This would facilitate the scalability and the realization of complex optical circuitry involving QMs. Furthermore, the integration of QMs with other required devices, such as quantum light sources and single photon detectors, would be greatly simplified. The possibility to write matrices of waveguides in the same sample would allow easy and stable access to spatially multiplexed QMs. Finally, the tight light confinement achieved in waveguide structures would lead to a strong enhancement of the light matter interaction. Solid state systems are well suited for the exploration of integrated QMs. Among them, rare-earth doped solids showed promising properties for QM applications with bulk crystals [17, 15].

In the first chapter, sec. 1.2.1.2, I report a detailed state of the art for integrated REI-based memories. The different examples discussed follow two approaches: either integrating REIs in already available guiding systems [80, 81, 23, 82, 39, 84, 85] or fabricating waveguides in crystals already used for demonstrating bulk QMs [86, 91, 87].

In this chapter, following the second approach, we propose an alternative way to fabricate waveguides in Pr^{3+}:Y_2SiO_5 using femtosecond laser micromachining (FLM), where the active ions are directly coupled to the light. FLM demonstrated in the past two decades to be a very powerful technology for the direct inscription of high quality optical waveguides in the bulk of both amorphous and crystalline transparent substrates [155, 156, 157, 158]. Several complex integrated photonic devices have been developed with this technique, ranging from all-optical routers [159] and power dividers [160], to modulators [161], and frequency converters [162, 163]. Moreover, it has been shown that laser written waveguide circuits in glass are suitable for supporting the propagation of photonic qubits [164], and represent a promising platform for the development of the rapidly growing field of integrated quantum photonics [165, 166, 167]. The class of materials where waveguide writing with FLM has been demonstrated includes several rare-earth doped crystals, e.g. Nd:YAG, Yb:YAG, Nd:YVO_4 , and Pr:YLF among others, with applications mainly oriented

towards the realization of integrated laser sources [168, 169, 170, 171]. FLM in Pr^{3+}:Y_2SiO_5 crystals was never reported in the literature before, and it allows us to take advantage of the direct access to the active ions as well as profiting of the exceptional performances as light storage medium.

6.2 Fabrication and experimental setup

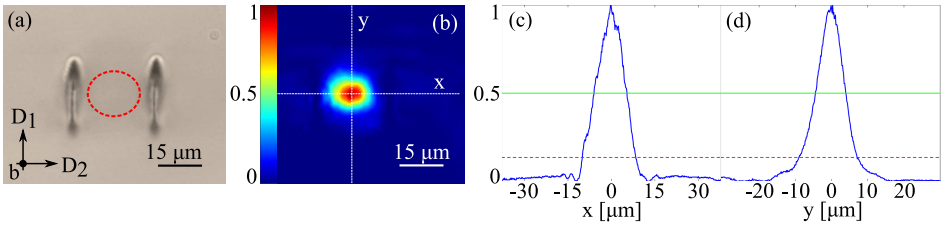

Figure 6.1: (a) Microscope picture of the waveguide cross section. The distance between the damage tracks is 25 μm. The red-dashed ellipse indicates the e^{-2} contour of the guided mode. Scale bar is 15 μm. (b) CCD-acquired near-field intensity profile of the guided mode. Scale bar is 15 μm. (c),(d) Normalized intensity profiles of the waveguide mode along the x and y sections indicated in panel (b). The resulting full widths at half maximum (FWHM) are $\Delta_x = 11.3\,\mu$m and $\Delta_y = 8.6\,\mu$m (green solid level). The measured e^{-2} diameters are $\tau_x = 18.5\,\mu$m and $\tau_y = 15.8\,\mu$m (red dashed level).

The substrate used is a Pr^{3+}:Y_2SiO_5 bulk crystal (Scientific Material), 10 mm-long (along the crystal b-axis) and with a concentration of active ions of 0.05 %. Optical waveguides are fabricated by FLM adopting the so-called type II configuration [115], where the fs-laser irradiation is used to directly inscribe into the substrate two closely spaced damage tracks, where the material locally expands and becomes amorphous. This gives rise to the formation of a stress field in their proximity, which, in turn, causes a material refractive index alteration. By tailoring properly the irradiation parameters and geometry, it is possible to obtain a light guiding region with a positive refractive index change localized between the two tracks. It is worth highlighting that in type II waveguides the core region (where most of the light remains confined) is only marginally affected by the fabrication process, hence preserving all its bulk properties. Single mode waveguides for 606 nm light have been fabricated with this method by inscribing pairs of damage tracks with a reciprocal distance of 25 μm and buried 100 μm beneath the sample top surface. Figure 6.1(a) shows a microscope picture of the waveguide cross section, in which the two damages are clearly visible.

The mode supported by the waveguide, when it is coupled with 630 nm light polarized parallel to the Y_2SiO_5 crystalline D_2-axis, is reported in fig. 6.1(b). From the horizontal and vertical intensity profiles, shown in panels (c) and (d), respectively, we estimate the full width at half maximum (FWHM) of the guided mode to be $\Delta_x = 11.3\,\mu$m and $\Delta_y = 8.6\,\mu$m. This analysis was performed in Milan. Before assembling the sample in our setup, we measured the guided mode also in our lab for 606 nm light, confirming the numbers measured in Milan ($\Delta_x = 11.4\,\mu$m and $\Delta_y = 8.5\,\mu$m).

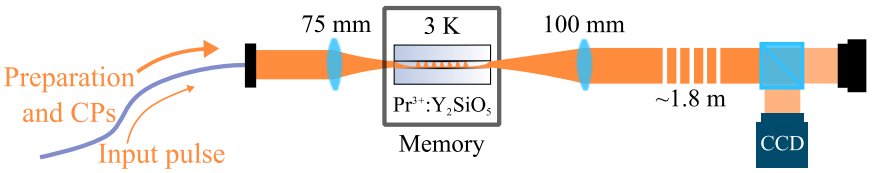

Figure 6.2: Sketch of the setup used for the measurements in Pr^{3+}:Y_2SiO_5 waveguide. The preparation light, control pulses (CPs) and input pulses come from the same beam. The Pr^{3+}:Y_2SiO_5 crystal is placed in a cryostat at a temperature <3 K. After an optical path of $\sim$ 1.8 m, the coupled light is split and detected with a camera (CCD) or a detector.

A sketch of our setup is depicted in fig. 6.2. We use the same beam for both memory preparation and input light pulses. As a consequence, we only use one AOM (contrary to all the other experiments in this thesis, see sec. 4.1). The coupling of the light into the waveguide is done by means of an external 75 mm focal length lens assembled on a translation stage. The final diameter (full width at half maximum) of the beam at the waveguide input facet is 28.3 μm. After the waveguide, the light is recollected with a 100 mm focal length lens. After $\sim$ 1.8 m, the mode coming from the waveguide is cleaned from the light scattered at the input facet with an iris and is sent to a detection stage. The detection is implemented with a CCD camera, for imaging and alignment, or with a photo-detector.

The measured transmission of the light through the optical waveguide for different input powers (see Appendix B.2), called coupling efficiency, is about C$=$ 50 %. It includes coupling mode mismatch and waveguide propagation loss. Fresnel losses at the waveguide input and output facets are quenched by a specific anti-reflection coating. The resulting waveguides support only one polarization mode (see Appendix B.2), parallel to the D_2-axis of the crystal, which interacts with Pr^{3+} ions in site 1 [172]. In

a bulk crystal, light polarized perpendicularly to the D_2-axis would only weakly interact with the Pr^{3+} ions, thus experiencing a higher transmission through the sample. In our case, as only the polarization along the D_2-axis is supported, we can confirm that the light is guided through the waveguide by rotating the polarization of 90° and checking that the transmission drops to 0 (see Appendix B.2).

6.3 Optical measurements

Coherence time, T_2

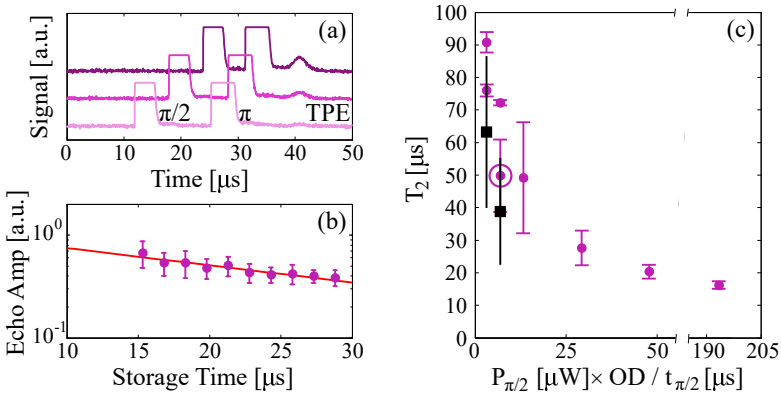

Figure 6.3: (a) Pulse sequence for the two-pulse photon echo (TPE) experiment. The three lines are measured traces for three different storage times, with an arbitrary background added for clarity. The $\pi/2-$ and $\pi-$pulse are cut because we want to zoom in the echo. (b) Echo efficiency as a function of the time delay 2τ. The fitting of the experimental data to an exponential decay is also shown (red solid line). For this set of data an optical coherence time $T_2 = 50 \pm 11\,\mu s$ is extrapolated. (c) Optical coherence times T_2 measured in the waveguide (dots) and in an equivalent bulk sample (squares) as a function of the quantity $\frac{OD \times P_{\pi/2}}{t_{\pi/2}}$.

The circled data point in panel (c) refers to the decay shown in panel (b).

To probe the coherence properties of the material after the waveguide fabrication we perform two-pulse photon echo (TPE) experiments and measure the optical coherence time T_2. The used protocol is described in sec. 3.1.5. The pulse sequence used is shown in fig. 6.3(a). When the time delay τ between the $\pi/2-$ and $\pi-$ pulse is increased, the amplitude of the echo is reduced due to the atomic decoherence. We estimate the optical coherence time T_2 from the decay of the echo (fig. 6.3(b)) by looking at the area of the pulse. We measure T_2 in single-class absorption features of different

optical depths (ODs) on the $1/2_g \rightarrow 3/2_e$ transition (prepared as explained in sec. 3.2.2) and for different powers in the $\pi/2-$pulse, $P_{\pi/2}$. To ensure efficient population transfer even when decreasing the pulse power the duration of the pulses $t_{\pi/2}$ is simultaneously increased, thus reducing their spectral bandwidth. Figure 6.3(c) summarizes the T_2 value obtained as a function of the quantity $\frac{OD \times P_{\pi/2}}{t_{\pi/2}}$, which gives a measure of the excitation intensity (purple circles). In fact, the more ions are excited the shorter are the coherence times measured due to instantaneous spectral diffusion (see sec. 2.2.2). It is worth noting that the obtained values agree with those reported as black squares in fig. 6.3(c), measured when the laser beam is shifted towards the center of the same Pr^{3+}:Y_2SiO_5 crystal, far from the laser-written waveguide, but maintaining the same focusing conditions. This demonstrates that the micromachining procedure does not affect the coherence properties of the material in the spatial mode where the light is guided.

Rabi frequency, Ω_R

The strength of the interaction between the light and the active ions is associated to the Rabi frequency Ω_R of the transition (see section 3.1).

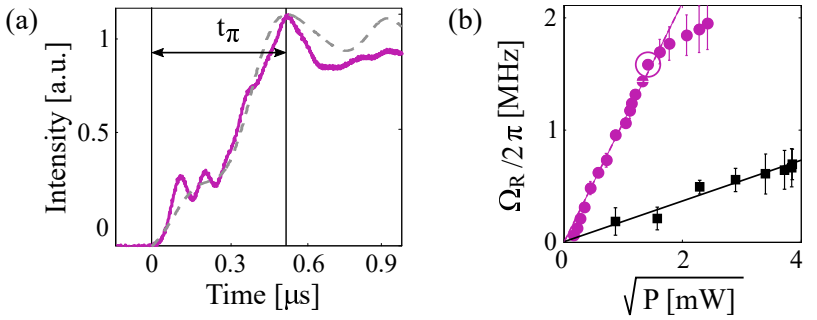

Figure 6.4: (a) Intensity of a long light pulse, $P \approx 2.6\,mW$, transmitted by a single class absorption feature with optical depth OD= 2.35. The Rabi frequency $\Omega_R^{WG} \approx 2\pi \times 1.3$ MHz $/\sqrt{\text{mW}}$ is estimated from the rising time t_π (indicated in the figure with vertical solid lines). The gray line is the trace where oscillations faster than 10MHz are removed. (b) Rabi frequency as a function of the pulse power measured in the waveguide (circles) and in the bulk (squares). The circled data point in panel (b) refers to the pulse reported in panel (a).

We measure Ω_R by means of optical nutation (see section 3.1.4): we send a long pulse resonant to a single-class feature prepared in the optical transition $1/2_g \rightarrow 3/2_e$ and we collect it at the photodiode after the transmission through the optical waveguide (solid curve in fig. 6.4(a)). The population inversion time, t_π is indicated with the solid vertical lines. We calculate the Rabi frequency from t_π, as $\Omega_R \cdot t_\pi = 5.1$ (sec. 3.1.4). The Rabi frequencies measured for different input light powers coupled in the waveguide are shown in fig. 6.4(b) as a function of the square root of the input power. For high P the pulse exhibits a fast oscillation with a frequency of about 10.2 MHz, i.e. the separation between the $1/2_g$ and $3/2_g$ ground states. We attribute the oscillation to beatings between the two transitions $1/2_g - 3/2_e$ and $3/2_g - 3/2_e$ that might be simultaneously excited by the pulse due to imperfect optical pumping. For this reason, in the present experiment the Rabi frequency is calculated in a trace corrected from the fast oscillation by removing frequencies higher than 10 MHz from the Fourier transform of the trace (gray dashed curve in fig. 6.4(a)). The error bar is given by the difference between Ω_R calculated from the measured trace and from the corrected one. For input powers up to about 2.6 mW the Rabi frequency scales as the square root of the power, as expected, but at higher powers the slope changes. This could be because the beatings between the two involved transitions becomes too high to be neglected, making our analysis too simplified. Alternatively, the deviation from the expected behavior could be caused by a saturation effect, given by the limited spectral width of the single-class absorptive feature prepared. When moving the beam into the bulk (black squares), the Rabi frequency scales with $\sqrt{P}$ with a much lower slope than that observed in the waveguide (the maximum being $\Omega_R^b \approx 0.4$ MHz at 15 mW). For input powers at which the behavior is linear, the waveguide features light-ion interaction strengths higher than in the bulk by about a factor 6, due to the efficient light confinement.

6.4 Light storage

Finally, we test the storage capabilities of our device by using the atomic frequency comb protocol [68]. We first tailor a single class $1/2_g \rightarrow 3/2_e$ transition in the center of the inhomogeneous broadening of the Pr^{3+} (following the procedure explained in sec. 3.2.2). The AFC, differently from the usual procedure (sec. 4.4), is prepared by burning the holes of the

AFC one by one in the absorption feature of the transition. The state

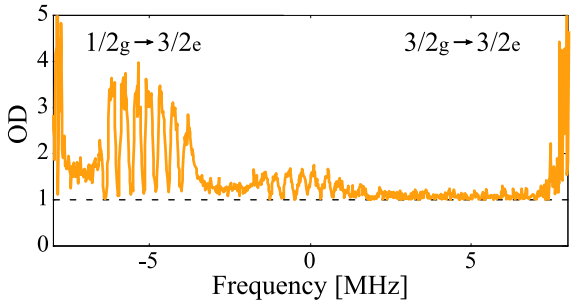

Figure 6.5: Example of a single-class AFC with $\Delta = 400\,\mathrm{kHz}$.

$3/2_g$, used for spin-wave (SW) storage, is kept empty during the preparation of the AFC by sending optical pulses resonant with the $3/2_g \rightarrow 3/2_e$ transition (see end of sec. 4.4). An example of AFC structure with periodicity $\Delta = 400\,\mathrm{kHz}$ is shown in fig. 6.5.

The results of the AFC storage experiments performed in this waveguide are shown in fig. 6.6. A Gaussian light pulse (black dashed curve, FWHM $= 345\,ns$) linearly polarized along the D_2-axis of Y_2SiO_5 is first sent through a spectral *pit* $\sim 18\,\mathrm{MHz}$-wide, prepared in the Pr^{3+} absorption line, and used as a reference. The solid lines in fig. 6.6(a) correspond to AFC echoes for different AFC spacings Δ. The internal storage and retrieval efficiency achieved, calculated as the ratio between the AFC echo and the input pulse transmitted through a transparency window, is reported in fig. 6.6(b), the maximal being $\eta_{\mathrm{AFC}} = 14.6\%$ for a storage time of $1.5\,\mu s$. The efficiency decreases when the storage time is increased due to a reduction of comb quality and finesse [68, 107]. The AFC echo, actually, decays much faster than the coherence time T_2 of the transition, namely $7.1\ \mu s$ as extracted from the fit of fig. 6.6(b) [27], due to inefficient comb preparation. This is mostly due to a limited preparation time, as the light is coupled into the waveguide only for half of the cryostat cycle. This obliges us to increase the power during the AFC tailoring, that degrades the peaks due to power broadening. The device efficiency η_{Device}, considering our memory as a *black box*, is defined as the ratio between the AFC echo and the input pulse before the crystal and it is reported in fig. 6.8(b) (purple dots). η_{Device} can be calculated by multiplying η_{AFC} by the waveguide transmission (50 %) and by e^{-d_0}, where d_0 is the background absorption in the transparency window, due to imperfect optical pumping

(in our case $d_0 = 1$, see dashed line in fig. 6.5). We emphasize that the waveguide coupling and background losses are not fundamental limitations and can be significantly reduced, for the former by improving the mode matching and, for the latter, by using shorter waveguides and/or optimized optical pumping techniques[1]. At the end of this chapter, in section 6.5, we show unpublished results of η_{AFC}, d_0 and η_{Device} taken in a shorter sample.

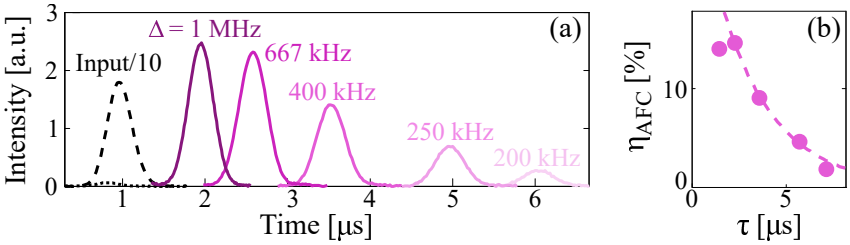

Figure 6.6: AFC storage in the excited state. (a) Temporal experimental trace. Dashed (dotted) line: 345 ns long input pulse transmitted through a spectral *pit* polarized parallel (perpendicular) to the Y_2SiO_5 crystalline D_2-axis, divided by 10 for clarity. Solid lines: AFC echoes for different comb spacings Δ. (b) Internal AFC efficiencies η_{AFC} for the different storage times τ, extracted from the traces in (a). The decay of η_{AFC} extracted from the fit (dashed line) is $7.1\mu s$.

We then perform SW storage (as explained in sec. 3.3.1 and demonstrated in Chapter 5). When a control pulse is applied before the rephasing of the atomic excitations the AFC echo is partially suppressed, as the transfer to the spin state $3/2_g$ takes place (see fig. 6.7(a)). After a controllable time T_s, a second control pulse is applied and the SW echo is retrieved (solid light blue curve). The control pulses have a Gaussian waveform and are frequency chirped by 1.5 MHz. To confirm that the input light field is stored as a spin wave, we measure its decay when increasing the spin storage time T_s (see fig. 6.7(b)). Assuming a Gaussian decay, we extract an inhomogeneous spin-broadening of $\gamma_{inh} = (23.6 \pm 7.7)$ kHz (as explained in sec. 3.3.1), compatible with those evaluated in different SW storage experiments in bulk Pr^{3+}:Y_2SiO_5 [88, 89, 24]. We observe an echo up to a total storage time of $t_s = 1/\Delta + T_s = 15\ \mu s$, more than two orders of magnitude longer that previous AFC demonstrations (at the excited state) in waveguides [82]. The maximal internal SW efficiency, calculated as the ratio between the SW echo and the input pulse transmitted through a transparency window, is $\eta_{SW} = 2\,\%$. Similarly to the storage in the excited

[1] In the present experiment the performances were probably limited also by unusual impurities in the memory crystal (see sec. 6.5).

state, waveguide and background loss have to be taken into account for estimating the device efficiency. The transfer efficiency of each control pulse is $\eta_T = 50\,\%$ for a laser power $P = 375\,\mu$W. The transfer efficiency is estimated from the formula $\eta_{SW} = \eta_{\mathrm{AFC}} \times {\eta_T}^2 \times \eta_C$ where η_C accounts for the decoherence in the spin state and is evaluated from $\eta_C = \frac{\eta_{SW}}{\eta_{SW}(0)}$, where $\eta_{SW}(0)$ is the storage efficiency at $T_s = 0$. It is worth noting that

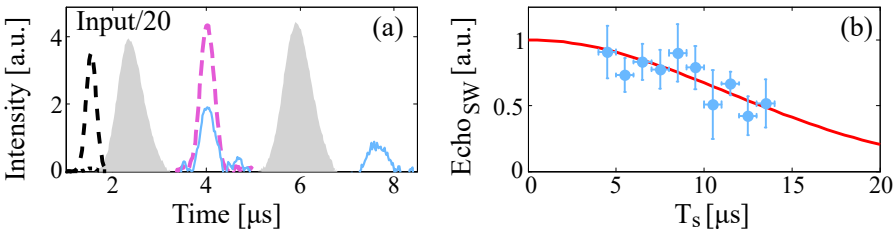

Figure 6.7: (a) Spin-wave storage. Dashed (dotted) black line: 260 ns long input pulse transmitted through a spectral *pit* polarized parallel (perpendicular) to the Y_2SiO_5 D_2-axis, divided by 20 for clarity. Purple dashed line: AFC echo for a storage time of $\tau = 2.5\,\mu$s (in absence of control pulse). The internal efficiency is $\eta_{\mathrm{AFC}} = 8.3\%$. The gray plain pulses are the control pulses, detected before the sample. The light blue solid line is the output when control pulses are applied, with a time difference of $T_S = 3.6\,\mu$s: the AFC echo is partially suppressed and a SW echo appears 6.1 μs after the input. The internal efficiency of the SW echo is 2 %. The additional noise due to the detector has been subtracted by the SW storage trace. (b) Normalized SW echo intensities as a function of the storage time T_S. The experimental data (dots) are fitted to a Gaussian decay to account for the inhomogeneous spin-broadening, from which we obtain $\gamma_{inh} = (23.6 \pm 7.7)$ kHz.

the transfer efficiencies of the CPs achieved in this waveguide sample ($\eta_T = 50\,\%$) are comparable to those obtained in the previous chapter with a bulk sample of 5 mm ($\eta_T = 73\,\%$), but the laser power of the control beam is more than 50 times lower. This result is promising in view of extending the storage protocol to the quantum regime, where the suppression of the noise induced by the control pulses is a crucial aspect [24, 90].

6.5 Type II new crystal

In 2016 our collaborators from Politecnico di Milano fabricated new type II waveguides in a new sample (again Pr^{3+}:Y_2SiO_5 with 0.05 % doping concentration from Scientific Material). The fabrication parameters are slightly different (reported in the Supplementary Material of [116]), optimized to maximize the coupling efficiency for single-mode waveguides

with different mode-sizes. The length of the new sample is 3.7 mm. The measured mode size of this new waveguide in FWHM is 8.5 μm along the horizontal direction and 7.7 μm along the vertical one (the distance between the two damage tracks is 20 μm).

A main difference regards the inhomogeneous broadening: the ions in the 1 cm sample, besides the usual inhomogeneous absorption that could be fit by a Gaussian of about 5.5 GHz, show a second broader absorption of about 25 GHz of FWHM (see Appendix B). This twofold contribution was measured only in this specific sample, both in waveguide and in the bulk crystal before the waveguides fabrication. The broader inhomogeneous line could be explained by lutetium oxyorthosilicate (Lu_2SiO_5) impurities in the Pr^{3+}:Y_2SiO_5 sample [173].

In the new waveguides we measure the optical coherence time T_2, the background optical depth d_0 and the AFC efficiency for different storage times. Much lower instantaneous spectral diffusion seems to occur while we measure the T_2, having an average of $T_2 = 72 \pm 5\,\mu$s even for a high number of atoms excited compared to the values of sec. 6.3 (see sec. B.4 in appendix).

To measure d_0 we create a spectral *pit*, like in the previous measurements, and we compare the transmitted signal through the waveguide with the input measured before the waveguide (renormalized for the coupling efficiency): the absorption into the spectral *pit* results in $d_0 = 0.27$, much lower than the $d_0 = 1$ measured in the 1 cm sample.

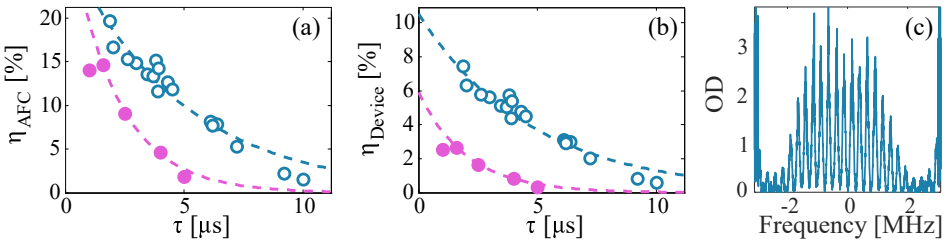

Figure 6.8: (a) AFC internal efficiencies. The filled purple points and line are taken from fig. 6.6(b); the empty circles are the efficiencies measured in a new sample 3.7 mm long. The AFC decay is 19.1μs for the new sample (7.1μs the old one). (b) Same of panel (a) considering the d_0 and coupling loss in the efficiency calculation. The measured coupling efficiency was 50% for the 1 cm sample and 49% for the 3.7 mm one. (c) Example of a single-class AFC with $\Delta = 250$ kHz measured in the new sample.

Finally we prepare different AFC features for different storage times. We use the technique described in sec. 4.4. After analyzing more carefully the transmission through the waveguide along the cryostat cycle, we optimize the pulse sequence for a faster preparation of a single-class feature, in order to have more time for the creation of the AFC. The results obtained for different storage times (again with classical light) are shown in fig. 6.8, panels (a) and (b), as empty circles (the purple points being the results for the 1 cm waveguide extracted from fig. 6.6): in panel (a) we show the η_{AFC}, being the internal efficiency of the AFC, without considering coupling efficiency and background absorption d_0; in panel (b) the total efficiency of the device, η_{Device}, considering the memory as a black box and dividing the measured echo by the input pulse measured before the cryostat. A measured trace of an AFC prepared in the new sample for a storage time $\tau = 4\,\mu$s is shown in panel (c).

6.6 Conclusions

In conclusion, we demonstrated an optical memory based on laser written waveguides in a Pr^{3+}:Y_2SiO_5 crystal. We showed that the waveguide fabrication does not alter the coherence properties of the bulk crystal, and that the light confinement in the crystal increases the light-matter interaction (as measured by the Rabi frequency) by a factor of 6 compared to a bulk crystal with the same focusing. In addition, we reported a proof-of-principle experiment of light storage using the full AFC protocol. We stored strong light pulses both in the excited and ground states of Pr^{3+} ions. The latter represents the first demonstration of an integrated on-demand spin-wave memory. We also show preliminary results on a new sample where we could perform better AFC preparation. These results show that integrated optical memories can be realized using laser written waveguides, a versatile and widely used technique in integrated quantum photonics. This opens new perspectives for the realization of long-lived integrated spin-wave quantum memories.

Chapter 7

Storage of heralded single photons in a *Type I* waveguide

In this chapter we demonstrate quantum light storage on a different type of laser-written waveguide, called type I. Differently from the waveguides described in the previous chapter, in which two tracks were fabricated along the crystal and light was guided between them, in type I waveguides only one track is required and light is directly guided into it. The new writing regime adopted allows us to attain waveguides with improved confining capabilities compared to type II ones. Apart from the increased light-matter interaction, this is important because the mode size of this kind of waveguides is compatible with the one of single mode fibers at the same wavelength. Despite the invasive fabrication process, the coherence properties of this waveguides are maintained to a high extent. Although only in the excited state and for pre-programmed storage times, we demonstrate storage times longer than previous realizations with single photons in integrated quantum memories, achieving storage efficiencies comparable to those observed in bulk samples. Our system promises to effectively fulfil the requirements for efficient and scalable integrated quantum storage devices.

The investigated type I waveguides were fabricated by our collaborators Dr. Roberto Osellame and Dr. Giacomo Corrielli at Politecnico di Milano. There they analysed the guiding properties of different type I and type II waveguides fabricated in the same sample. The characterization of the coherence of the ions in the new type II waveguides is reported at the end of the last chapter, together with the demonstration of storage (sec. 6.5).

The results of this chapter are published in Optica [116], and the photo of our waveguide was selected as the Cover of the same issue of the Journal. The content of this chapter is mostly taken from the paper. Some unpublished data are present at the end of the chapter, where we report on a new setup that we used to increase the preparation time of the AFC. Thanks to it, we could increase the time for the preparation of the AFC, reducing the power used, and we could show a significant increase of the storage time. This improvement opened the way to the realization of the experiment reported in the next chapter.

7.1 Introduction

We showed in the previous chapter that optical channel waveguides can be fabricated in the bulk of crystalline substrates by femtosecond laser micromachining (FLM). Another possibility, using the same technique, consists in adopting a different writing regime and fabricating directly the waveguide core. This is a substantially different type of waveguide, called type I. In this case, a much lower energy fluence is required for a positive refractive index change at the irradiated material volume. Identifying a processing window for fabricating type II waveguides is relatively simple, in fact they have been demonstrated in numerous different materials, including rare-earth doped crystals, mainly for integrated laser source applications [174, 175, 176]. On the contrary, the fabrication of type I waveguides in crystalline substrates is a very challenging task, since it requires finding a very narrow window of processing parameters, if any. So far, this fabrication regime has been demonstrated only in a very limited number of cases [177, 178, 179], including lithium niobate [180, 162, 181], potassium dihydrogen phosphate (KDP) [182] and polycrystalline matrices [183, 184].

We report on the realization of type I waveguides in a Pr^{3+}:Y_2SiO_5 crystal. A characterization of the light guiding properties at 633 nm was performed in Politecnico di Milano by Dr. Giacomo Corrielli. The small dimensions of the waveguide modes guarantee the compatibility with optical fibers and a significant enhancement of the light-matter interaction. Moreover, spectroscopic investigations reveal that the fabrication does not affect the measured optical properties of Pr^{3+} ions in the light guiding region. Finally, to assess the potential of our new platform as quantum memory,

we implement quantum storage of heralded single photons. The achieved storage times are 100 times longer than in previous experiments with single photons in waveguides [23, 83].

7.2 A new waveguide writing regime in Pr^{3+}:Y_2SiO_5

Fabrication of type I waveguides

Type I waveguides have been directly written by FLM in the volume of a 3.7 mm long Pr^{3+}:Y_2SiO_5 crystal with a dopant concentration of 0.05%, 100 μm below the sample top surface. The waveguide was fabricated such that only light polarized along the crystal D_2 axis is guided. The refractive index change of the core with respect to the substrate was estimated numerically from the guided mode profile (according to the method described in ref. [185]) as $\Delta n \approx 1.6 \times 10^{-3}$. As type I waveguides in crystals are often thermally unstable [181], it is worth mentioning that no visible degradation of our type I waveguides in Pr^{3+}:Y_2SiO_5 was observed, after several months of exposure to normal ambient and cryogenic conditions. More details about the fabrication of the waveguides can be found in Appendix C.

The physical mechanisms that contribute to inducing a type I waveguide in crystals strongly depend on the specific material considered, encompassing the formation of lattice defects and a local change in the material polarizability. Understanding their relative weight is a difficult task. Detailed studies performed on type I waveguides written in $LiNbO_3$ and Nd:YCOB crystals showed that the positive refractive index change in these materials results mainly from a weak lattice distortion and partial ion migration effects taking place at the irradiated area [180, 178]. Such modifications, typically observed in a regime close to the material processing threshold, essentially preserve the bulk properties of the crystal, as demonstrated for type I waveguides in $LiNbO_3$ [162]. Regarding type I waveguides in Pr^{3+}:Y_2SiO_5, a fundamental explanation of the origin of the positive index change induced by ultrafast laser irradiation is still unknown.

Benchmarking type I vs. type II waveguides

Our collaborators in Milan fabricated in the same sample different type II and type I waveguides and characterized them experimentally. All the details about the fabrications and measurements can be found in the Supplemental Material of the paper [28].

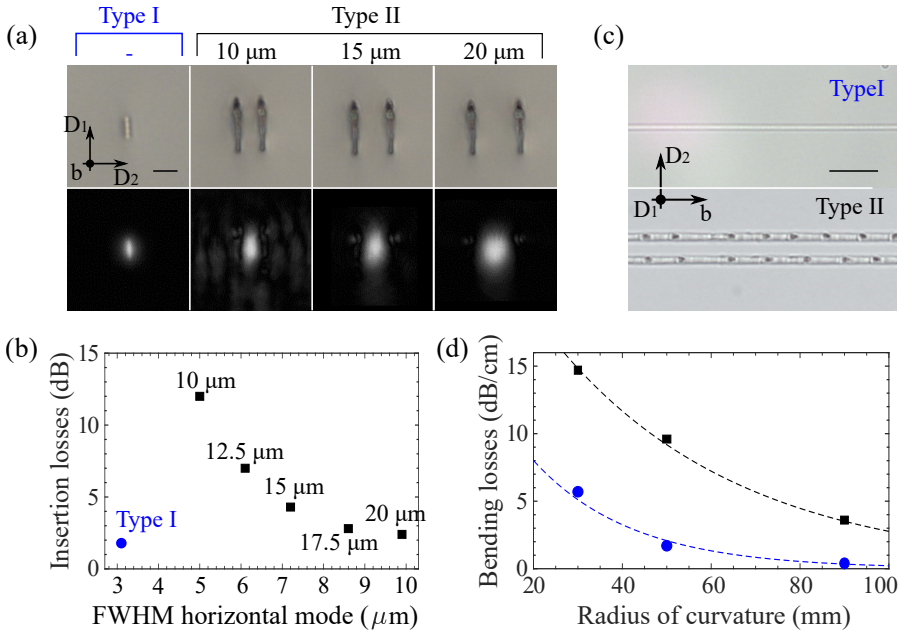

Figure 7.1: (a) Optical microscope image of the waveguide transverse cross section (top row) and guided mode intensity profile (bottom row) of all fabricated waveguides. The numbers above the figures specify the separation between the laser tracks in type II waveguides. The scale-bar is 10 μm. (b) Insertion losses vs FWHM mode diameter in horizontal direction for type I (blue circle) and type II (black squares) waveguides. (c) Microscope picture of the longitudinal profile of a type I (top) and a type II waveguide with $d = 10$ μm (bottom). The scale-bar is 20 μm. (d) Bending losses as a function of the radius of curvature for type I (blue circles) and type II (black squares) waveguides. Dashed lines are best exponential fits of experimental data [186]. Error-bars in plots (b) and (d) are smaller than the data markers.

Five type II waveguides have been compared, with different separation d between the tracks forming the cladding, ranging from 10 μm to 20 μm. Light at 633 nm from a He-Ne source, polarized along the D_2 crystal axis, was coupled into a type I and the different type II waveguides. The normalized mode intensity profile of all waveguides, measured with a CCD camera, is reported in figure 7.1(a) together with a microscope picture of

their transverse cross sections. In addition, the total insertion losses (IL), defined as the ratio between the light power measured before and after the waveguide, was measured for every waveguide. The results of this measurement as a function of the mode diameter (horizontal in FWHM) are shown in fig. 7.1(b). It is clearly visible that for the type II waveguides (black squares) the reduction of d reduces the mode size, but, at the same time, leads to a dramatic increase of IL. On the other hand, the type I waveguide (blue circle) supports the smallest mode (3.1 μm $\times$ 5.9 μm FWHM diameters) and, simultaneously, exhibits the lowest value of IL among all waveguides analyzed. This fact is readily explained by looking at the waveguides longitudinal profiles shown in fig. 7.1(c): the type I waveguide features a smooth and very uniform profile along the propagation direction, while the side tracks of type II waveguides present a rough and less uniform profile that increases light scattering, especially for small values of d. A more detailed analysis of the different contributions to the waveguide IL can be found in the Supplemental Material of the paper [28].

As a further comparison, the measured bending losses (BL) for the two types of waveguide, caused by the coupling of light to leaking modes during the propagation in a curved guided path, are shown in fig. 7.1(d). The curved waveguides were fabricated with constant radius of curvature R_C. This measurement was performed for values of R_C of 30 mm, 50 mm, and 90 mm, both on the type I and on type II waveguides with d = 20 μm, fabricated in a dedicated sample (total sample length = 9 mm). As expected, the values of BL increase for shorter R_C for both types. However, in type I waveguides the measured BL reach particularly low values, and become almost negligible for R_C >90 mm. This is to be expected, as BL decreases for increasing confinement of the guided light [186].

This experimental analysis allows us to conclude that type I waveguides in Pr^{3+}:Y_2SiO_5 show better guiding performances than their type II counterparts, both in terms of waveguide losses and in terms of light confinement. Interestingly, the measured values of BL for type I waveguides are compatible with the fabrication of complex integrated devices, i.e. directional couplers or waveguide arrays, as bending radii in the order of tens of mm allow for a flexible engineering of evanescent waveguide coupling, even in samples with a limited length.

7.3 Experimental setup

Fig. 7.2 shows the experimental setup for the spectroscopy and single photon storage measurements, presented in the next paragraphs.

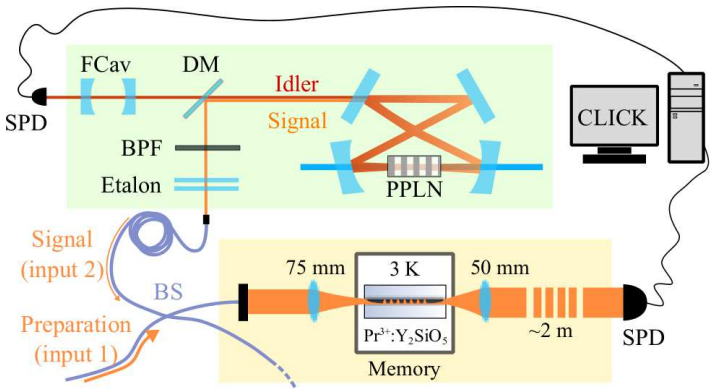

Figure 7.2: Setup: a pump laser at 426 nm (blue beam) is shined to a periodically-poled lithium niobate (PPLN) crystal in a bow-tie cavity. Photon pairs are generated by spontaneous parametric down-conversion and separated with a dichroic mirror (DM). The idler photon at 1436 nm (brown beam), is sent to a filter cavity (FCav). The signal photon at 606 nm (orange beam) passes through a band-pass filter (BPF) and an etalon and enters the input 2 of a fiber beam-splitter (BS). The signal photon and the preparation light (from input 1 of the BS) emerging from one output of the BS are coupled into the $Pr^{3+}:Y_2SiO_5$ waveguide.

The preparation pulse sequence, as usual, is produced modulating our CW laser at 606 nm with AOMs in double-pass configuration (see sec. 4.1). The preparation light is coupled into one input port of a 50:50 fiber beam splitter (BS, input 1 in fig. 7.2). The signal (either classical pulses to probe the crystal or heralded single photons to be stored) is coupled into the second input port (input 2). One output port of the fiber BS is sent to an independent optical table (yellow rectangle) where the $Pr^{3+}:Y_2SiO_5$ crystal is maintained at 2.8 K, while the second output is used as reference to monitor the pulses that we send into the waveguide. The light is coupled into the waveguide using a 75 mm lens, which focuses the beam to a waist $< 10\,\mu$m at the input facet of the crystal. The outcoming light from the waveguide is collected with a 50 mm lens and sent to a detection stage, after a path of about 2 m. The detection is implemented with a CCD camera for imaging and alignment, with a photo-detector for protocols with classical light, or with a single photon detector (SPD) for experiments with

single photons. For autocorrelation measurements a Hanbury Brown-Twiss setup is assembled with fiber beam splitters and additional SPDs. All the experiments are synchronized with the cycle of the cryostat (1.4 Hz). Because of vibrations, the light is efficiently coupled in the waveguide only for less than 300 ms in each cycle (see Appendix C.2.1).

Our heralded single photons are generated with a new generation photon-pair source build in our group by the PhD student Dario Lago Rivera (see sec. 4.3.2 for more details). It is based on cavity-enhanced type I spontaneous parametric down-conversion (CSPDC) (fig. 7.2). The bow-tie cavity (BTC), pumped with a 426 nm laser, is in resonance both with the signal photon at 606 nm and its heralding photon at 1436 nm (idler). Due to the clustering effect of the BTC the signal and idler photons are distributed along many spectral modes (an analisys of the spectrum will be performed in the next chapter). The idler photons pass through a home-made Fabry-Perot filter cavity (FCav in fig. 7.2, linewidth 80 MHz, FSR=17 GHz), to guarantee single-spectral-mode heralding. They are then coupled into a single mode fiber to an SPD. The 606 nm photons, after passing through an etalon filter, are coupled to a single-mode polarization-maintaining (PM) fiber, and then to the input 2 of the fiber BS. The heralding efficiency of the SPDC source is $\eta_H^{\mathrm{SPDC}} \sim 25\%$ after the PM fiber and $\eta_H^{\mathrm{WG}} \sim 7\%$ in front of the waveguide. The loss is due to the BS and to mode-diameter mismatch between the PM fiber and the fiber BS, and could be readily reduced by using a fiber switch.

The photons generated by this source are 1.8 MHz broad (narrower than those generated by the previous source, see Chapter 5). The overlap of these photons with our AFC (about 4.6 MHz) is estimated to be about 78 % (see inset of fig. 7.7(a)).

7.4 Spectroscopic and coherence measurements

The inhomogeneous broadening of the transition of Pr^{3+} at 606 nm in the waveguide has been estimated from the transmission of an optical pulse through the crystal while tuning the laser frequency. The full-width at half maximum (FWHM) is ~ 9 GHz in optical depth (OD) (see Appendix B.2), in good agreement with bulk samples with similar ion concentrations. Moreover it is important to note that the central frequency did not shift

with respect to the bulk. The hyperfine splitting of the levels (Appendix C.3.1) and the oscillator strength of the transitions (Appendix C.3.2), measured following the spectral hole burning experiments described in section 3.2, are also consistent with those measured in the bulk [135]. The unaltered spectroscopic properties confirm that the fabrication process does not substantially affect the crystalline structure of the irradiated region.

For quantum memory application, the coherence of the ions in the waveguide should be also maintained. Coherence and lifetime of the optical transition are measured by means of, respectively, two-pulse (TPE) [134] and three-pulse stimulated photon echo (SPE) [187] experiments.

Coherence time, T_2

The TPE technique is explained in sec. 3.1.5: two pulses separated by a time τ_2 are sent in resonance with the single-class transition $|g\rangle$-$|e\rangle$. Increasing τ_2 results in a decay of the two-pulse echo, TPE (fig. 7.3(a)). From the exponential decay of the echo intensity with increasing time τ_2 (fig. 7.3(a)) we extract the coherence time of the Pr^{3+} ions in the waveguide.

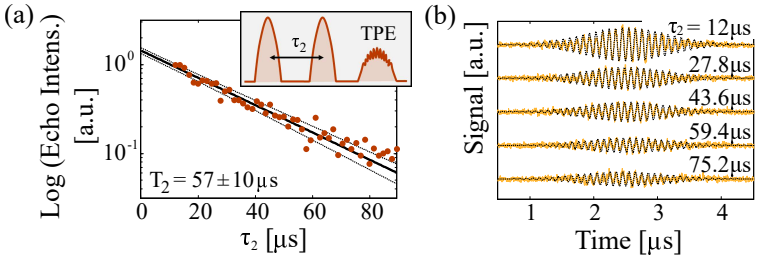

Figure 7.3: (a) Decay in the echo intensity for a two-photon echo pulse measurement. The black solid line is the fit to an exponential decay and the dotted lines indicate the error. The inset shows the temporal sequence used. The time interval between the first and the second pulse is called τ_2 (solid arrow). (b) Examples of heterodyne detected TPE at different times τ_2. The solid orange line is the experimental signal and the dotted black line the sinusoidal fit. The echo intensity is proportional to the square of the oscillation amplitude.

Usually we measure TPE with direct detection (as in Chapter 6). To keep the power of the $\pi/2$ low and thus to limit the dephasing caused by instantaneous spectral diffusion effects (sec. 2.2.2), the T_2 of fig. 7.3(a) is measured with heterodyne detection, i.e. magnifying the TPE by sending

a third pulse, detuned by 10 MHz, in the time mode where the TPE is expected. A typical pulse sequence for the heterodyne detection of the TPE is shown in the inset of fig. 7.3(a). The echo is detected in form of oscillations on a probe pulse 10 MHz detuned with respect to the excitation and rephasing pulses. Fig. 7.3(b) represents examples of heterodyne detected TPE at different storage times. The echo intensity is calculated as the square of the envelope of these oscillations. In our case, by probing a single-class absorption feature at the $1/2g - 1/2e$ transition, we measure a maximum coherence time $T_2 = 57 \pm 10\,\mu s$. This is lower than the maximal T_2 measured in bulk samples or type II waveguides (see Chapter 6). We note however that the T_2 is affected by instantaneous spectral diffusion and that higher values could in principle be achieved by decreasing the average number of atoms excited (see section 6.3).

Lifetime, T_1

To study the lifetime (T_1) of the transition and slow dephasing mechanisms, e.g. spectral diffusion (see sec. 2.2.2), we analyze the SPE. The effect of two optical pulses on an inhomogeneous transition can be imagined as the generation of a spectral grating in which the distance between the peaks is the inverse of the temporal interval between the pulses ($1/\tau_2$). If a third pulse is sent through this spectral grating it is diffracted, giving rise to an echo after a time τ_2, the SPE (fig. 7.4(b), a mathematical description can be found in [187]). During the time τ_1 between the generation of the spectral grating (second pulse) and the third pulse, atoms can fall from $|e\rangle$ to $|g\rangle$ due to spontaneous emission or other irreversible relaxation mechanisms. As a consequence, the optical contrast of the *grating* would decrease, resulting in a lower SPE.

A typical output of a SPE experiment (measured with direct detection) is shown in fig. 7.4(a) while panel (b) sketches the temporal sequence used. To reduce the errorbar, we perform these measurements with a higher excitation power than that used in the TPE measurement (i.e. interacting with more ions), thus we expect the absolute value of T_2 to be lower due to instantaneous spectral diffusion. We measure the decay of the SPE with τ_2 for different values of τ_1. By fitting these decays with exponentials, we extract the expected areas of the SPE(τ_1) for $\tau_2 = 0$, SPE$(\tau_1; \tau_2 = 0)$ (fig. 7.4(c)). The decay of SPE$(\tau_1; \tau_2 = 0)$ directly depends on the lifetime

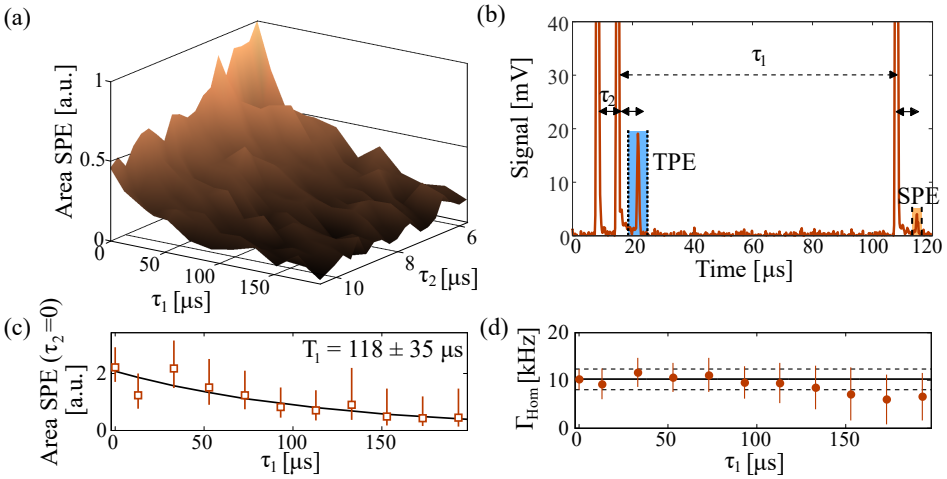

Figure 7.4: (a) Area of the stimulated photon echo (SPE), in arbitrary units, varying the times τ_1 and τ_2; (b) Temporal trace of the SPE process. The SPE signal is highlighted by the orange area. The time interval between the second and third pulse is called τ_1 (dotted arrow); (c) Values of the SPE areas at $\tau_2 = 0$ (extracted from the exponential decays of the SPE areas over τ_2) plotted as a function of τ_1. From the decay of the SPE vs τ_1 (for $\tau_2 = 0$) we extract the excited state lifetime of the ions, T_1; (d) Homogeneous broadening of the optical transition for increasing τ_1. The values are extracted from the decays of the SPE vs τ_2 for different τ_1 values. The black solid line is the value extracted from the T_2 measurement for $\tau_1 = 0$, the dashed lines indicating the error.

of the excited state $|e\rangle$, namely $T_1 = 118 \pm 35\,\mu$s. This value is lower than that obtained from previous fluorescence measurements in a different Pr^{3+}:Y_2SiO_5 crystal (about 160 μs [119]) but in good agreement with that measured with SPE in the same bulk sample, $T_1 = 103 \pm 11\,\mu$s (measured in the middle of the bulk crystal, focusing with an incoupling lens with focal length of 20 cm). In presence of spectral diffusion, the ions could experience frequency shifts induced by flips of the surrounding nuclear spins. This would cause a slow broadening of the ions linewidth, Γ_{hom}, for increasing τ_1 [188]. However, as we can clearly see from fig. 7.4(d), $\Gamma_{hom}(\tau_1) = 1/[\pi\, T_2(\tau_1)]$ remains consistent over time with the value at $\tau_1 = 0$ (solid line) (about 10 kHz), proving the absence of spectral diffusion in the timescale and excitation power analyzed. The same trend is observed in SPE measurements in the bulk crystal.

The T_1 of the ions in the waveguide has been measured, at a later stage,

with a fluorescence experiment (see sec. 3.1.6): after preparing a single-class feature on the $|g\rangle$-$|e\rangle$ transition, we send a resonant optical pulse exciting some of the atoms. From the exponential decay of the noise detected after the pulse, which accounts for the decay of the excited population, we extract a lifetime $T_1 = 142 \pm 11\,\mu$s (see Appendix C.3.3). This value is close to the value usually measured in bulk in our labs, $T_1 \sim 160\,\mu$s [119], but it has never been measured in the present bulk sample. The reason why the two measurement of T1 give different values is still under investigation.

Rabi frequency, Ω_R

One of the advantages of optical waveguides is the enhanced light-ions interaction due to the strong light confinement. As in the previous chapter, we quantify the strength of this interaction measuring the Rabi frequency Ω_R of the optical transition by means of optical nutation (see section 3.1.4): we prepare a single-class absorption feature on the $\pm 1/2g - \pm 3/2e$ transition and measure the population inversion time t_π induced by a long resonant probe pulse as in fig. 7.5(a). We calculate the Rabi frequency as $\Omega_R t_\pi = 5.1$ (sec. 3.1.4) for several probe powers, P (orange filled points in fig. 7.5(b)).

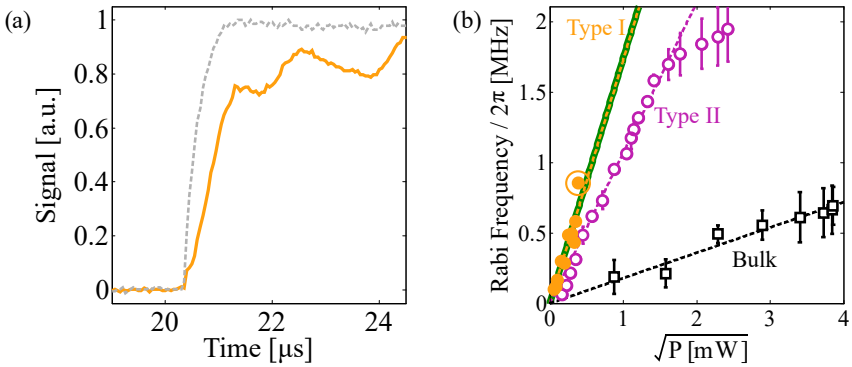

Figure 7.5: (a) A long light pulse, $P = 0.51$mW, measured before the crystal (dotted gray line) and after being transmitted by a single-class absorption feature (solid orange trace). (b) Rabi frequency as a function of the pulse power measured in the type I waveguide (filled orange circles), compared with the Ω_R of fig. 6.4, measured in a longer bulk sample (empty black squares) containing also a type II waveguide (empty purple circles). The dashed lines are the linear fits to the experimental data. The green solid line is the expected behavior for the type I waveguide from the slope of the type II fit, scaled according to the different diameters. The circled data point in panel (b) refers to the pulse in panel (a).

We show in fig. 7.5(b), for comparison, the measured Ω_R for different P in a waveguide type II and in bulk (respectively purple empty circles and black empty squares), from the previous chapter (see fig. 6.4). From the linear fit of Ω_R vs $\sqrt{P}$ for the type I (orange dotted line), we extract $\Omega_R = 2\pi \times 1.75\,\mathrm{MHz}/\sqrt{\mathrm{mW}}$, i.e. an increase of 1.6 with respect to the type II waveguide and almost one order of magnitude with respect to the bulk crystal (maintaining the same optics). This result fully matches with the expected increase due to the stronger light confinement (green solid line below the fit), which has been calculated from the fit of the type II (purple dotted line), renormalized for the different mode diameter in the waveguide type I. Moreover this value agrees quite well with that calculated from the dipole moment of the investigated transition (1.45×10^{-32} C m [189]), i.e. $2\pi \times 1.6\,\mathrm{MHz}/\sqrt{\mathrm{mW}}$. For this calculation we consider a Gaussian mode with the average FWHM diameter measured at 606 nm with the same setup used for the optical nutation measurements. For both simulations, the measured diameters (4.5 μm and 7.6 μm in the horizontal and vertical directions, respectively) are different than those quoted in fig. 7.1, being the modes in fig. 7.1 calibrated in a different setup (i.e. with different light wavelength, objective and CCD camera).

7.5 Storage of heralded single photons

Before storing the heralded signal photons, we analyse their non-classical correlations. We quantify the non-classicality of the photon-pair correlations measuring the normalized second-order cross-correlation function: $g^{(2)}_{s,i}(\Delta t)$ (see sec. 1.4.1). We build a coincidence histogram using the idler detection as start and the signal photon as stop (inset in fig. 7.6(a)). The $g^{(2)}_{s,i}$ is extracted from the coincidence histogram. The measured $g^{(2)}_{s,i}$ values for a window $\Delta t = 400$ ns for different pump powers are plotted in fig. 7.6a (empty orange circles). The highest value, $g^{(2)}_{s,i}(400\,\mathrm{ns}) = 209 \pm 9$, is achieved at the lowest measured pump power (P = 0.1 mW), and decreases while increasing P, as expected for a two-mode squeezed state (sec. 1.4.1).

We demonstrate the quantum nature of the signal-idler correlations by violating the Cauchy-Schwartz (CS) inequality. The classical bound is

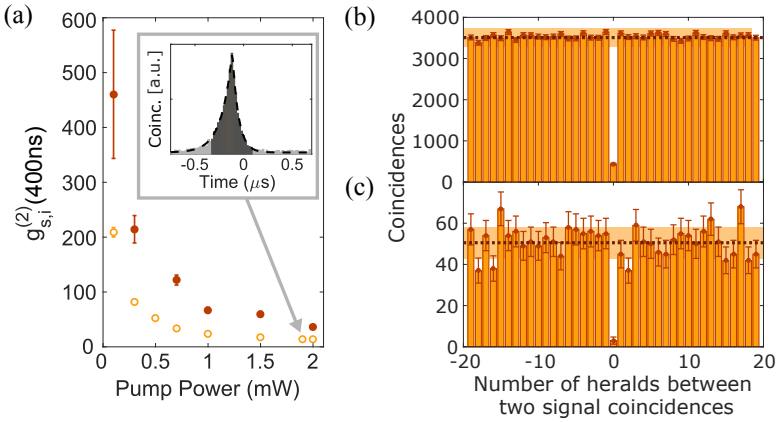

Figure 7.6: (a) Measured $g^{(2)}_{s,i}$, for different pump powers, with just the source (empty light orange dots) and after the *pit* (full brown points). The inset represents the time-resolved signal-idler coincidence histogram with just the source: the darker region is the window considered for the calculation of the $g^{(2)}_{s,i}$ (400 ns) and the black dashed line is the temporal fit of the biphoton correlation; (b, c) Coincidences between signal photons splitted with a fiber BS, respectively before and after passing through a *pit* in the waveguide, sorted by the number of heralding photons between pairs of contiguous signal counts.

given by the parameter $R = \frac{(g^{(2)}_{s,i})^2}{g^{(2)}_{s,s} \cdot g^{(2)}_{i,i}} \leq 1$, where $g^{(2)}_{s,s}$ ($g^{(2)}_{i,i}$) is the auto-correlation of the signal (idler) photons (sec. 1.4.3). The measured auto-correlations, using an integration window $\Delta t = 400$ ns for comparison with the $g^{(2)}_{s,i}$, are $g^{(2)}_{s,s}(400\,\text{ns}) = 1.051 \pm 0.002$ and $g^{(2)}_{i,i}(400\,\text{ns}) = 1.25 \pm 0.03$. Using these values we find, for the lowest pump power, $R = (3.3 \pm 0.3) \times 10^4$, surpassing the classical bound by more than 10 standard deviations. Even for the highest pump power (P = 2 mW), where the measured cross-correlation is $g^{(2)}_{s,i}(400\,\text{ns}) = 13.8 \pm 0.3$, we find $R = 145 \pm 6$, which violates the CS inequality by more than 20 standard deviations, thanks to the better statistics.

To demonstrate the single photon nature of our source we measure the heralded auto-correlation of the signal photon, $g^{(2)}_{i:s,s}(\Delta t)$ (sec. 1.4.4). This can be extracted from the histogram of fig. 7.6(b), built like in ref. [151, 141]. We find $g^{(2)}_{i:s,s}(400\,\text{ns}) = 0.12 \pm 0.01$ for a pump power of 1.7 mW. This value is considerably lower than the classical bound $g^{(2)}_{i:s,s} \geq 1$ and compatible with the single photon behavior ($g^{(2)}_{i:s,s} \leq 0.5$) [190].

Spectral pit

We then send the signal photons through the waveguide, where we hole-burn a transparency window of $\sim 16\,\text{MHz}$ (spectral pit of sec. 3.2.2, orange line in the inset of fig. 7.7(a)). We measure the $g^{(2)}_{s,i}$ vs pump power after sending the signal photons through the *pit* (full brown circles in fig. 7.6(a)). The correlations after the *pit* become remarkably higher because the crystal acts as a spectral filter: the *pit* selects a single frequency mode while all the others are absorbed by the Pr^{3+} ions spread over the whole inhomogeneously broadened absorption line [107, 142, 143] (before the crystal there is only an etalon filtering the signal photons, while the idler photons are filtered by the FCav). We find $R = 524 \pm 84$ after the *pit* for the highest measured power, violating the CS inequality by more than 6 standard deviations. As we do not have enough statistics to measure the unconditional autocorrelation of the signal photons after the pit, the R-value is calculated by assuming $g^{(2)}_{s,s} = 2$. Note that this is a consevative choice, as it increases the classical bound of the CS inequality. Finally, we measure the $g^{(2)}_{i:s,s}(\Delta t)$ of the signal photons after the *pit*: from the histogram of fig. 7.6(c), we extract $g^{(2)}_{i:s,s}(400\,\text{ns}) = 0.06 \pm 0.04$ ($\text{P} \sim 1.7\,\text{mW}$). We know that the $g^{(2)}_{i:s,s}$ is inversely proportional to $g^{(2)}_{s,i}$ for two-mode squeezed states and low pump powers [191]. This is verified in our measurement, as the heralded auto-correlation is lower after the *pit*, where the cross-correlation is higher. For a pump power of 1.7 mW, using $g^{(2)}_{s,s} = 2$ and the measured value for $g^{(2)}_{i,i}$, we find $g^{(2)\,\text{th}}_{i:s,s} = g^{(2)}_{s,s} \cdot g^{(2)}_{i,i} / g^{(2)}_{s,i} \sim 0.06$ which matches with the measured heralded auto-correlation.

Storage with AFC

The sequence of optical pulses used to create a single-class AFC is very similar to the one explained in section 4.4: after populating the $1/2g$ level with a single class of ions (duration $\sim 80\,\text{ms}$), we send a series of pulses, resonant with the $1/2g - 3/2e$ transition, whose Fourier transform is the AFC that we want to create (duration $\sim 35\,\text{ms}$). The measurement is performed in the remaining time ($\sim 150\,\text{ms}$), resulting in a duty cycle for the AFC storage of $\sim 21\%$ (accounting for the duty cycle due to the cryostat vibrations, see Appendix C.2.1). The generated feature, for a storage time of $1.5\,\mu\text{s}$, is plotted as a brown line in the inset of fig. 7.7(a),

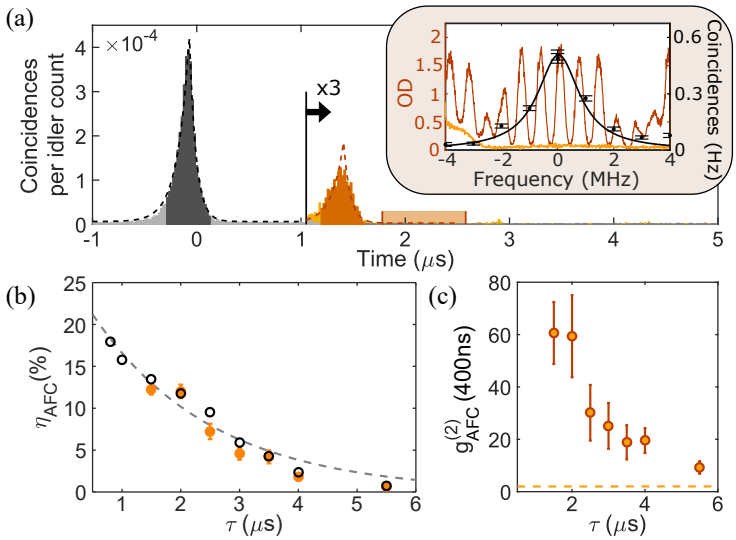

Figure 7.7: (a) Time-resolved histogram of the idler-signal coincidences for signal photons passing through the *pit* (gray histogram) or the AFC for $\tau = 1.5\,\mu$s (orange histogram). The counts in the AFC are multiplied by 3. The darker regions of the peaks show the windows considered for η_{AFC} and $g^{(2)}_{s,i}$ calculations. The black and brown dashed lines are the temporal decays of the correlations (inset of fig. 7.6(a)), renormalized for losses and efficiencies after the *pit* and the AFC, respectively. The shaded rectangle is the region in which the accidental counts for the AFC echo are measured. The absorption profiles of the *pit* (orange) and the comb (brown) are plotted in the inset, with the spectrum of the single photons (black points and line, see section 4.3.2); (b) Internal storage efficiency η_{AFC} at different storage times τ for single photons (full orange points, error bars account for Poissonian statistics) and classical light (empty black circles); (c) Cross-correlation values between idler photons and stored signal photons, $g^{(2)}_{AFC,i}$, for different τ. The dashed line is the classical upper bound, $\sqrt{g^{(2)}_{s,s} \cdot g^{(2)}_{i,i}} = 1.58 \pm 0.02$ (assuming $g^{(2)}_{s,s} = 2$).

together with the spectrum of the input photons (black line, see section 4.3.2). Thanks to the enhanced light-ions interaction, the maximum power that we inject in the waveguide during the AFC creation is $\sim 100\,\mu$W, i.e. two orders of magnitude lower than what is usually necessary in bulk, in agreement with the Ω_R increase.

When a herald is detected, an AOM in front of the pump laser is closed to reduce the noise coming from the source during the AFC echo retrieval (position of the vertical line in fig. 7.7(a)). The minimum response time of this gate is $t_P^{\text{off}} = 1.2\,\mu$s, which limits our minimum storage time to

$\tau = 1.5\,\mu$s. For longer storage times, t_P^{off} is delayed in order to maintain $\tau - t_P^{off} = 0.3\,\mu$s. The AFC echo for a storage time $\tau = 1.5\,\mu$s is shown in fig. 7.7(a) (orange trace). The exponential fit of the biphoton temporal decay, measured before the memory crystal (sec. 4.3.2, black dashed line of the inset in fig. 7.6(a)), is plotted on top of the input (black dashed line) and the AFC echo (brown dashed line), renormalized for the different count-rates. Note that the linewidth of the photons, both after the *pit* and emitted by the comb, remains similar, confirming that there is a good match between the width of the comb and the spectral profile of the photons.

We measure the coincidences between the idler photons and the signal ones transmitted through the *pit* before and after each storage experiment. We consider the average of the two as our reference input (gray peak in fig. 7.7(a)) to account for fluctuations in power. We evaluate the storage efficiency by integrating the counts of the histogram in a 400 ns window centered at the AFC echo (dark orange region at about $1.5\,\mu$s, fig. 7.7(a)) divided by the counts inside a 400 ns window centered at the input (dark gray region about $0\,\mu$s, fig. 7.7(a)), the latter normalized by the transmission through the *pit* (85%, see inset in fig. 7.7(a)). The resulting efficiency is the internal efficiency of the process, η_{AFC}. The total efficiency of our device, i.e. the ratio between the output signal and the input signal before entering the waveguide, is calculated multiplying η_{AFC} by the coupling efficiency into the waveguide ($\sim 40\%$). We perform storage experiments with an average pump power of 1.7 mW. The internal efficiencies for different storage times are shown in fig. 7.7(b) (full orange points). For comparison we measure the internal efficiency of our memory with classical pulses (empty black circles in fig. 7.7(b)), using the same comb preparation sequences, showing a good overlap between the quantum and the classical regimes. The efficiency decrease for increasing τ is fitted with an exponential decay, $e^{-4/(T_2^*\Delta)}$ [27], from which we extract the effective coherence time of our storage protocol, $T_2^* = 8\,\mu$s, much smaller than the T_2 (see section 7.4). This suggests that our storage time is at the moment limited by technical issues and not yet by the coherence time T_2 of the Pr^{3+} in the waveguide. An important contribution is probably given by instantaneous spectral diffusion and power broadening because, due to the time limit imposed by the cryostat cycle, we implement the optical pumping for the AFC preparation with relatively high power. The

remaining mismatch between T_2^* and T_2 is likely due to the finite laser linewidth. In section 7.7 we show an increase of storage time by a factor of 2 given by a longer preparation cycle.

The $g^{(2)}_{AFC,i}$ of the AFC echo is measured similarly to the one of the input: we find $p_{s,i}$ integrating the counts in a window of 400 ns centered at the AFC echo (the same region considered for η_{AFC}); $p_s \cdot p_i$ is measured integrating the accidentals coincidences after the AFC echo up to the last stored noise count, $t_P^{\text{off}} + \tau$ (light orange rectangle in fig. 7.7(a)), renormalized to a 400 ns window. Fig. 7.7(c) shows the $g^{(2)}_{AFC,i}$ values for AFC echoes measured at different τ. The cross-correlation increases after the storage up to 61 ± 12 for a storage time of 1.5μs, with respect to 36 ± 3 after the *pit*. This could be explained by the presence of broadband noise from the SPDC source, which is not in resonance with the inhomogeneous absorption line of the Pr^{3+} ions. Such noise would not be present in the temporal mode of the AFC echo, where the pump is gated off [107]. After the AFC, the $g^{(2)}_{AFC,i}$ decreases for long storage times. This happens because, as η_{AFC} decreases, our signal-to-noise ratio becomes limited by additional background noise. If we did not have any background noise, the value of the $g^{(2)}_{AFC,i}$ should remain constant for different τ, as the storage efficiency would be the same for the AFC echo and for the stored noise. Nevertheless, the $g^{(2)}_{AFC,i}$ remains higher than the classical bound (orange dashed line) for all the measured storage times up to $\tau = 5.5\,\mu$s, for which we violate the CS inequality with $R = 34 \pm 18$ (above the classical bound by almost 2 standard deviations), effectively demonstrating the longest quantum storage in an integrated solid-state optical memory (100 times longer than the previous demonstrations of single photon storage in waveguides [23, 83]). Moreover, thanks to the convenient energy level scheme, our system enables the full spin-wave AFC storage, thus giving access to both longer storage times and on-demand read-out (sec. 3.3.1).

7.6 Spin-wave storage

For the quantum repeater application we want to demonstrate in our group (section 1.2.2) we would need to store photons as spin-waves (SW), with the possibility to retrieve them on-demand, after long storage times. Some

preliminary analysis on SW storage with classical light in a type I waveguide will be described below. Nevertheless, going to single photon level would require a much longer and detailed analysis of the noise, as well as higher storage and retrieval efficiencies.

A storage sequence is shown in fig. 7.8(a). The input pulse (black line) is divided by 20 to better see the retrieved echoes. The AFC echo (orange line) is retrieved after $\tau = 2.5\,\mu$s with an internal efficiency of $\eta_{AFC} = 2.8\,\%$. This is lower than what shown in fig. 7.7 because we have to keep the spin-state empty during the preparation, loosing again time for the AFC generation. To perform SW storage we send two control pulses (CP1 and CP2, gray shaded areas). CP1 maps the excitation into the spin-state. Then the light can be retrieved on-demand by sending CP2 after a time T_s. The brown trace shows a spin-wave echo retrieved after a time $\tau+T_s = 9\,\mu$s and with an efficiency $\eta_{SW} = 0.6\,\%$. Repeating this measurement for different T_s, we can study the decay of the spin-wave echo (brown points in fig. 7.8(b)). From its fit to a Gaussian fit (black line) we exctract the inhomogeneity of the spin-state (see section 3.3.1), being $\gamma_{inhom} = 84 \pm 5$ kHz. This value is more than 3 times higher than the usual spin inhomogeneity measured in bulk (fig. 5.11(a)) and in type II waveguides (fig. 6.7(b)) and it causes a faster decay. Nonetheless, it should not represent a fundamental limit to our storage time, as it could be compensated by applying spin-echo rephasing techniques [192]. The spin-inhomogeneity measured in the bulk of the same sample after the waveguides fabrication is $\gamma_{inhom} = 12 \pm 1$ kHz (see Appendix C.3.4). This value is about half of that usually measured in bulk samples with similar ion concentration (we measured ~ 20 kHz in Chapter 5 and ~ 24 kHz in Chapter 6). This is due to a μ-metal shield placed around the crystal, which reduces the external magnetic fields [193].

Unfortunately, the γ_{inhom} had not been measured in this sample before the fabrication of the waveguide, so we can only give some tentative explanation for the inconsistency. Surface effects seem unlikely, considering that both type I and type II waveguides are fabricated at the same depth ($100\,\mu$m below the crystal surface). So far, the most likely explanation is that the sample where the type I waveguide were fabricated had been obtained by cutting a bigger one, without proper annealing treatments. Further investigations are being carried on at the time of writing.

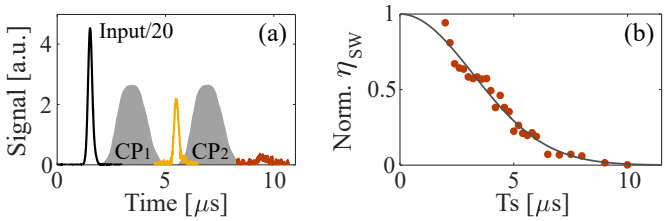

Figure 7.8: (a) Spin-wave storage. The black curve is the input optical pulse (divided by 20 for clarity). The light orange line is the AFC echo (for $\tau = 2.5\,\mu$s, internal efficiency of $\eta_{AFC} = 2.8\%$) in absence of control pulses. The gray plain pulses are a sketch of the control pulses. The brown line is the spin-wave echo, retrieved when control pulses are applied. The time difference between the control pulses is $T_S = 5.5\,\mu$s. The internal efficiency of the spin-wave echo is 0.6 %. (b) Normalized spin-wave echo intensities as a function of the storage time T_S. The experimental data (dots) are fitted to a Gaussian decay to account for the inhomogeneous spin-broadening, from which we obtain $\gamma_{inh} = (84 \pm 5)$ kHz.

We performed a few measurements with weak coherent states to measure the μ_1 of our system, i.e. the number of photons required in the input to have a signal-to-noise ratio of 1 in the retrieved SW echo [24]. Similarly to Chapter 5, we add a second crystal that we use as a tunable spectral filter (filter crystal, 5 mm long in the present experiment); moreover, we place before it an AOM which acts as a fast temporal gate. With a mean value of 122 photons per pulse in the input (a Gaussian of FWHM $\sim$ 300 ns), we measured a signal-to-noise ratio of 4.1, corresponding to a $\mu_1 = 29.9$ (summing the counts in a window of 720 ns around the echo, $\eta_{\mathrm{SW}} = 0.6\%$). Note that these measurements are just preliminary. To store real single photons we need to prepare better combs (i.e. to increase η_{AFC}) and to reduce the population in the spin state. To achieve this goal we need longer preparation time, limited in this moment by the vibrations of the cryostat. Having a fiber pig-tailed sample would be a fundamental step along this direction. Also the transfer efficiency of the CPs is very limited, meaning that they have to be further optimized (which would probably help also to better clean $|s\rangle$). If these solutions would not be enough, other filtering strategies will be considered, as, for example, a longer filter crystal to increase the absorption at the unwanted frequencies (in the SW storage experiment described in Chapter 5 we used a 3 mm-long filter crystal).

7.7 Higher AFC efficiency (counter-propagating preparation)

As discussed in section 7.5, the main motivation for our fast decay of the AFC efficiency with storage time is given by our limited preparation time. In fact, having little available time, we have to increase the optical power used for the preparation of the AFC. As a consequence, instantaneous spectral diffusion effects and power broadening increase, degrading our optimal AFC.

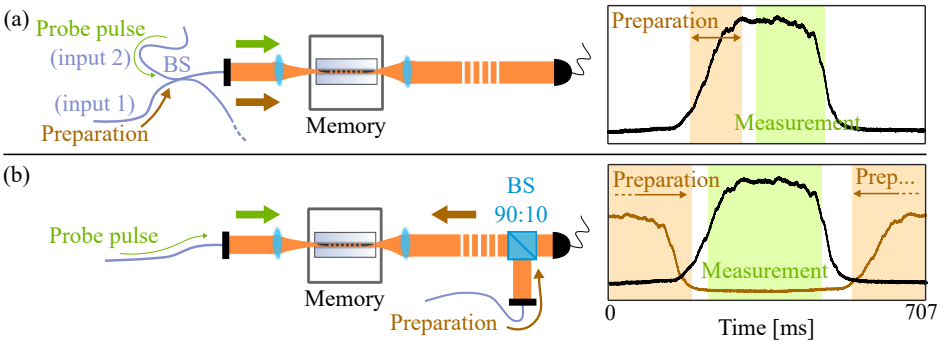

Figure 7.9: Sketch of two different setups used for measurements in waveguide type I. (a) The preparation and probe beam are coupled into the waveguide from the same optical path, coming from two different ports of a fiber BS. (b) The preparation beam is aligned counter-propagating to the probe light thanks to a 90:10 (T:R) BS. In this way the two beams can be coupled into the waveguide independently, during the two different phases defined by the cryostat cycle. The insets are the measured transmissions for each beam (both in CW) vs time, being the black line the probe beam and the brown one the preparation light. The green area describes the moment in which the measurement is performed, the brown one defines the preparation phase.

To have more time for the preparation of the AFC (as well as for the measurement), we send the preparation beam couter-propagating to the probe, making them independent. The old and new setups are sketched, respectively, in the panels (a) and (b) of fig. 7.9. Having two independent paths, we can align the preparation beam and the probe in order to couple them into the waveguide during two different phases of the cryostat cycle (see insets on the right). In the experiment presented so far in this chapter the two beams were coupled simultaneously (black trace), and we had to use that limited time both to prepare the memory (orange area) and to probe it (green area). In the second situation, the memory is prepared

when only the preparation beam is coupled into the waveguide (brown trace). When, due to vibrations of the cryostat, its coupling is lost, the probe beam is coupled (black trace) and the measurement starts.

This gives us a much longer time to prepare the memory, together with a longer duty cycle for the experiment (300 ms/ 707ms). The best efficiencies measured in the two different situations are plotted in fig. 7.10: our old efficiencies (filled points, taken from fig. 7.7(b)) decay with a $T_2^* = 8 \pm 1\,\mu s$, while the measurements done with the new setup (empty points, measured with classical light) show a $T_2^* = 16 \pm 1\,\mu s$, which represents an increase by a factor of 2 in decay time.

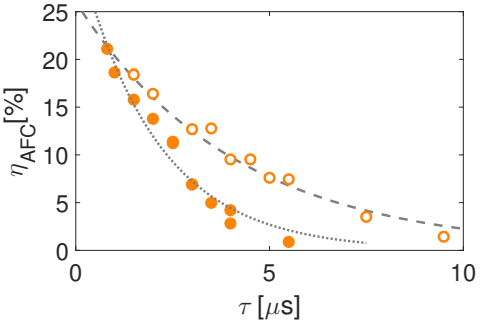

Figure 7.10: Decays of η_{AFC} for AFCs prepared with the setup sketched in panel (a) (full points) and (b) (empty points) of fig. 7.9.

The experiment described in the next Chapter will be performed with the setup sketched in panel (b) of fig. 7.9.

7.8 Conclusion and Outlook

In this chapter we proposed a new platform for the implementation of integrated quantum storage devices. We demonstrated the generation of type I waveguides in a Pr^{3+}:Y_2SiO_5 crystal using fs-laser micromachining in a new writing regime. We showed that the fabrication of type I waveguides preserves the measured spectroscopic properties of Pr^{3+}. We implemented a quantum storage protocol for heralded single photons, observing high non-classical correlations for storage times 100 times longer than in previous waveguide demonstrations. We show some preliminary results on SW storage experiments in these kind of waveguides. The use of type I waveguides in Pr^{3+}:Y_2SiO_5 gives several advantages with respect

to type II ones. In type I waveguides, the guided mode is in general sensibly smaller than what obtainable in a type II waveguide with comparable losses. This yields an enhancement in the interaction of the guided light with the rare earth dopants. Moreover, the mode matching between type I waveguides and standard single mode optical fibers would allow us to glue directly the Pr^{3+}:Y_2SiO_5 samples to fiber patch cords with low coupling losses, greatly simplifying the procedure of light coupling inside the cryostat and avoiding the temporal constraints on the photon storage given by the cryostat vibrations. We show, in fact, that having longer memory preparation times would allow us to burn better AFCs. High-quality type I waveguides will also allow to produce linear cavities with high quality factors by directly writing Bragg gratings superimposed to the waveguide [194]. In addition, type I waveguides in Pr^{3+}:Y_2SiO_5 could also be easily interfaced with laser written optical circuits in glass, potentially opening the way to the realization of integrated hybrid glass/crystal platforms [195] embedding quantum memories. Remarkably, taking advantage of the intrinsic three-dimensional capabilities of FLM, one can envision high spatial multiplexing by an efficient exploitation of the substrate volume, with matrices of quantum memories interconnected to linear fiber arrays by glass circuits. Finally, for this kind of waveguides, the absence of lateral damage tracks (present in the type II counterpart) enables greater freedom in engineering the evanescent coupling of light between different waveguides. This, together with the tighter bending radii achievable in type I waveguides, permits to easily inscribe optical circuits in Pr^{3+}:Y_2SiO_5 crystals embedding directional couplers and other integrated optics devices, for performing complex tasks besides quantum light storage, fully on chip.

Chapter 8

Quantum storage of frequency-multiplexed heralded single photons

In this chapter I report on the quantum storage of a heralded frequency-multiplexed single photon in an integrated laser-written waveguide fabricated in a rare-earth doped crystal. The single photon contains 15 discrete frequency modes separated by 261 MHz and spanning across 4 GHz. It is obtained from the non-degenerate photon pair created using a source based on cavity-enhanced spontaneous down conversion, where the heralding photon is at telecom wavelength and the heralded photon is at 606 nm. Both the type I waveguide and the photon pair source are the same as the previous chapter. The frequency-multimode photon is stored by creating multiple AFCs within the inhomogeneous broadening of the crystal. Thanks to the intrinsic temporal multimodality of the AFC scheme, each spectral bin also includes 9 temporal modes, such that the total number of stored modes is about 130. We demonstrate that the storage preserves the non-classical properties of the single photon, and its normalized frequency spectrum.

The results reported in this chapter are published in [40]. The content of this chapter is mostly taken from the paper and its supplementary material.

8.1 Introduction

We showed in the first chapter that multimode QMs would greatly help the scaling of quantum networks by decreasing the entanglement distribution time between remote quantum nodes [19, 15]. Current research focuses mostly on time multiplexing in rare-earth doped crystals [20, 21, 22, 23, 24, 26, 27, 28, 29, 30, 31] and in spatial multiplexing in atomic gases [32, 36, 37, 33, 34, 35]. Beyond these demonstrations, rare-earth doped crystals represent a unique quantum system thanks to their wide inhomogeneous broadening, which could also add another degree of freedom for multiplexing, i.e. the storage of multiple frequency modes [18]. The ability to perform frequency-multiplexed storage allows for a QR architecture to be built based on active feed-forward and QMs with only pre-programmed storage times, without the need for QMs with an on-demand retrieval capability [18]. This unique ability could also enable the generation of high-dimensional light-matter frequency entanglement [196]. Furthermore, it could provide a QM for frequency bin-encoded qubits, which are gaining interest both in quantum information and computation [197, 198, 196, 199, 200].

Very few experiments have explored the storage of frequency-multiplexed photonic states. Qubits encoded with weak coherent states have been stored in up to 26 frequency modes in the excited state of a Tm-doped waveguide [18], and up to two modes in the spin state of a Pr-doped crystal [31]. Parts of the spectrum of a broadband single photon were also stored in up to 6 frequency bins in an Er-doped optical fiber [39]. In contrast, our source naturally generates photon pairs in discrete frequency bins [116] that can all be stored in our crystal.

In this chapter I report on the first demonstration of quantum storage of a frequency-multiplexed single photon into a laser-written waveguide integrated in a Pr^{3+}:Y_2SiO_5 crystal (sec. 7.2). We demonstrate the non classicality of the correlations of the multiplexed biphoton after a pre-programmed storage time of 3.5 μs. We also show that the normalized spectrum of our single photon is well preserved during the storage. The multimode capability of our memory is further increased thanks to the intrinsic temporal multimodality of the AFC protocol (sec. 3.3). The great advantage of using waveguides is that the power required to prepare

the quantum memory is strongly reduced due to the increased light-matter interaction. This enables simultaneous preparation of several memories at different frequencies, with a moderate laser power.

8.2 Experimental setup

The setup, fig. 8.1(a), consists of two main parts: the photon-pair source and the memory. The first is based on cavity-enhanced spontaneous parametric down conversion (CSPDC) (explained in detail in sec. 4.3). The cavity, resonant both with the idler (at 1436 nm, telecom E-band) and the signal (606 nm) frequencies, redistributes the bi-photon spectrum in narrow frequency modes (fig. 8.1(b)). These modes are separated by the cavity free spectral range (FSR = 261.1 MHz) and have a linewidth of 1.8 MHz (measured in sec. 4.3.2). Because the signal and idler photons have different FSR, only a few modes (15 in our case) are generated [140] (a more detailed explanation in Appendix D.1). So far, only the central frequency mode (at frequency 0 in fig. 8.1(b)) was heralded and stored (Chapters 5 and 7). For most of the measurements reported in this chapter, the idler photon is directly sent to a single photon detector (SPD), resulting in a frequency-multimode heralding (MMi). Occasionally, a home-made Fabry-Perot filter cavity (FCav in fig. 8.1(a)) is used to provide a single frequency heralding (SMi).

The signal photon, filtered with an etalon, is coupled into a SM fiber and sent to the memory optical table. We store the signal photons in the same Pr^{3+}:Y_2SiO_5 -based type I waveguide of Chapter 7 (at cryogenic temperature, ∼2.8 K). The setup of the memory, shown in fig. 8.1(a), is described in detail in the previous chapter, sec. 7.7. If we want the photons to be transmitted through the waveguide, we produce a spectral pit around the signal frequency mode. The implemented storage protocol is the atomic frequency comb (AFC) technique (see sec. 3.3). To store the whole spectrum of the frequency-multiplexed photons, we send the preparation beam to two cascaded electro-optical modulators ($EOM_{1,2}$) with resonance frequencies equal to 1×FSR and 3×FSR of the CSPDC source, respectively (see spectrum in fig. 8.1(d)). With this method, using the same preparation time that we would need to prepare just one comb, we simultaneously tailor many AFCs (up to 15 demonstrated here), all for the

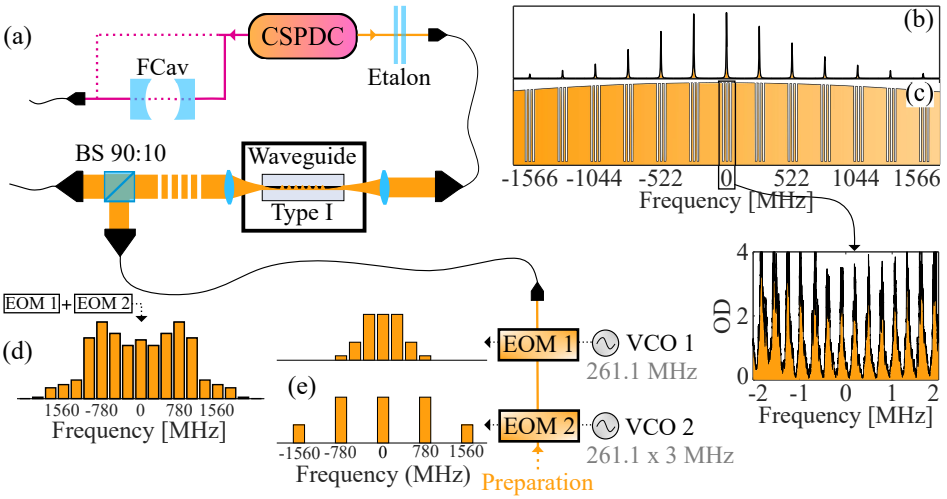

Figure 8.1: (a) Experimental setup. From the photon-pair source (CSPDC) the idler photon (purple beam) is coupled to a fiber, either directly or after passing through a filter cavity (FCav). The signal photon (orange beam) is sent through an etalon and then to the memory crystal (waveguide type I). The preparation light (bottom) is modulated with two EOMs: EOM_1 (EOM_2) is driven with a voltage controlled oscillator VCO_1 @261.1 MHz (VCO_2 @3x261.1 MHz). A 90:10 (T:R) beam splitter couples 10% of the preparation beam into the waveguide, counter-propagating with the signal photons. The modulation given by each EOM is in (e), the resulting spectral distribution of the preparation light after both EOM is shown in (d). (b) Sketch of the generated bi-photon spectrum. (c) Sketch of the inhomogeneous broadening, tailored with many atomic frequency combs (AFCs). The inset is a trace of a measured AFC in OD ($\tau = 3.5\,\mu s$, measured internal efficiency $\eta_{AFC} = 8.5\%$, see sec. D.2 of the appendix for more details).

same τ (3.5 μs) and with the same internal efficiency ($\eta_{AFC} = 8.5\%$) within the inhomogeneous absorption profile of Pr^{3+} (fig. 8.1(c), the inset shows a measured AFC trace). Hence, to perform multimode storage (MMs) we switch on both EOMs, while we switch them off to store just a single mode (SMs).We note that this method has a very favorable scalability, as the number of spectral modes stored scale exponentially with the number of EOMs used ($> 3^{\#\text{EOMs}}$). The total efficiency of the storage, considering the memory as a black box, is given by η_{AFC} times the coupling of the photon into and out of the waveguide, which is measured to be 40% in the present experiment (see sec. D.2 of the appendix for more details).

8.3 Non-classical nature of the heralded photon before and after the memory

As a figure of merit for our photon pairs we use the second-order normalized cross-correlation function between signal and idler fields, $g^{(2)}_{s,i}(\Delta t)$ (see sec. 1.4.1). We measured $g^{(2)}_{s,i}$ vs pump power (P) of the heralded photons before and after the storage (brown empty and orange full dots in fig. 8.2(a), respectively). Here, both the idler and signal photons are multimode (MMi - MMs). An example of a trace from which we extract the $g^{(2)}_{s,i}$ is shown in the inset of fig. 8.2(a): the brown and orange traces represent coincidence histograms between idler and signal photons (P=3 mW) measured before the memory setup and after the storage, respectively. The coincidence window considered, $\Delta t = 400$ ns, is shown as a darker region in both the traces. Thanks to the intrinsic temporal multimodality of the AFC scheme [68] and to the CW nature of the CSPDC source, we store $\tau/\Delta t = 3.5\,\mu s/400\,ns \sim 9$ distinguishable temporal modes. Note that the temporal coherence of our heralded photon is 120 ns; we could consider smaller detection windows, thus increasing both the $g^{(2)}_{s,i}$ and the number of temporal modes stored at the cost of a slightly lower storage efficiency. As expected for a two-mode squeezed state (sec. 1.4.1), the $g^{(2)}_{s,i}$ increases while decreasing P (fig. 8.2(a)). Except for the point at 0.5 mW, where the coincidence rate becomes comparable to the noise rate, the $g^{(2)}_{s,i}$ after the storage follows the same behaviour of the measurement with the source only. All the data points are above the classical limit (gray dotted line), defined by the Cauchy-Schwarz inequality as $\sqrt{g^{(2)}_{i,i} \cdot g^{(2)}_{s,s}}$ (sec. 1.4.2). The expected autocorrelation for the photon x (x = s, i), multiplexed over N modes, is $g^{(2)}_{x,x} = 1 + 1/N$ [114]. Moreover, the $g^{(2)}_{x,x}$ is considered in a 400 ns window, further approaching the expected value to 1. For simplicity, in the plot, we do the consevative choice of assuming a classical limit of 2 (expected value for a single mode thermal state, see sec 1.4.2).

To fully characterize the non-classicality of the bi-photon, we measured the heralded autocorrelation of the signal photon $g^{(2)}_{i:s,s}(\Delta t)$ [151] (sec. 1.4.4). Here again, both the heralding and the signal photons are multimode (MMi - MMs). A $g^{(2)}_{i:s,s}(\Delta t)$ histogram measured before the memory setup for P = 0.25 mW is reported in fig. 8.2(c). The $g^{(2)}_{i:s,s}(\Delta t)$ has been measured before the memory setup for different P, the lowest point (extracted from

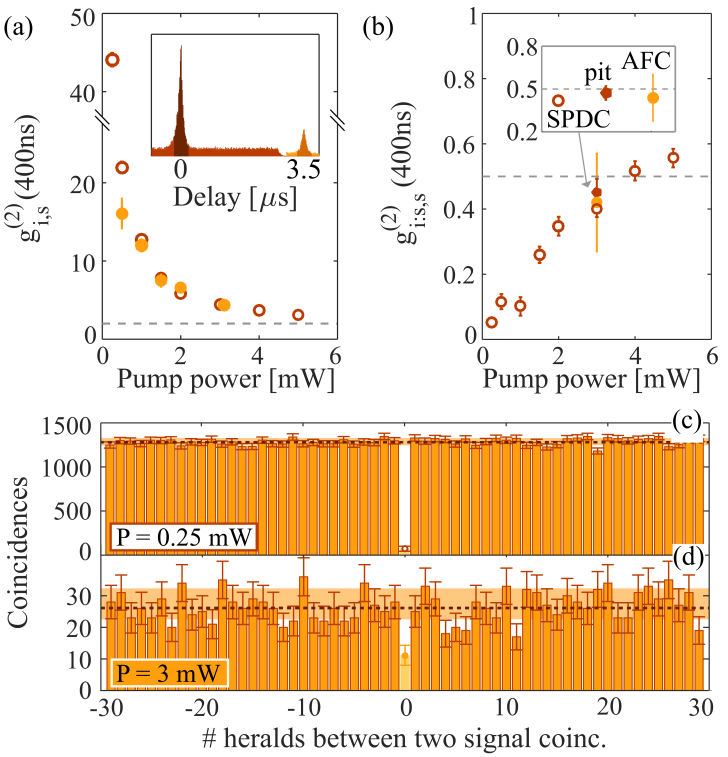

Figure 8.2: (a) Second order cross-correlation value $g^{(2)}_{s,i}(\Delta t)$ vs pump power (P) for the photon-pair source alone (empty brown circles) and after the storage of the signal (plain orange points). The inset shows a temporal coincidence histogram between signal and idler photons at P=3 mW (the input photon in brown and AFC echo in orange). (b) Conditional autocorrelation of the signal photon $g^{(2)}_{i:s,s}(400ns)$ vs P for the source alone (empty brown circles). $g^{(2)}_{i:s,s}(400ns)$ for the signal photon transmitted through a spectral pit (plain brown dots) or after storage (plain orange points) are also shown for P = 3 mW (magnified in the inset). (c) Conditional autocorrelation histogram for the source alone for P = 0.25 mW. (d) Conditional autocorrelation histogram of the stored signal photons for P = 3 mW (measurement time > 44 hours).

fig. 8.2(c)) being $g^{(2)}_{i:s,s}(400\text{ ns}) = 0.052 \pm 0.007$, widely in the single photon regime. To overcome the low statistics, we repeated the measurement of the $g^{(2)}_{i:s,s}(\Delta t)$ for P = 3 mW sending the signal photons to the memory setup, and preparing a multimode spectral pit or AFC. The comparison of the results for the same pump power is shown in the inset of fig. 8.2(b). All the measured data points of fig. 8.2(b) are below the classical limit of 1. Moreover the $g^{(2)}_{i:s,s}(\Delta t)$ measured at 3 mW after the spectral pit ($g^{(2)}_{i:s,s}(400\text{ ns}) = 0.45 \pm 0.04$) or after the storage in the AFC

($g^{(2)}_{i:s,s}(400\text{ ns}) = 0.42 \pm 0.15$) are both compatible with the measurement performed before the memory setup ($g^{(2)}_{i:s,s}(400\text{ ns}) = 0.40 \pm 0.03$). We thus conclude that the storage in the memory does not degrade the statistics of the single photons.

8.4 Number of effective modes

As the spectrum of our bi-photon is not flat (fig. 8.1(b)), the count rate does not increase linearly with the number of stored modes. We define an *effective mode* as a mode whose count rate is the same as the one of the central frequency mode. Hence, if we store just the central mode (SMs), we store 1 effective mode. On the other hand, the whole spectrum of the photon (15 spectral modes) will be equivalent to 5.6 effective modes. By using different EOM configurations (as sketched in fig. 8.3(c)), we can vary the number of effective modes stored (N_{eM}, more details in Appendix D.2.2). The light orange data points in fig. 8.3(a) show the measured coincidence rate in the retrieved AFC echo versus N_{eM}. For this measurement the idler photon is not filtered (MMi).

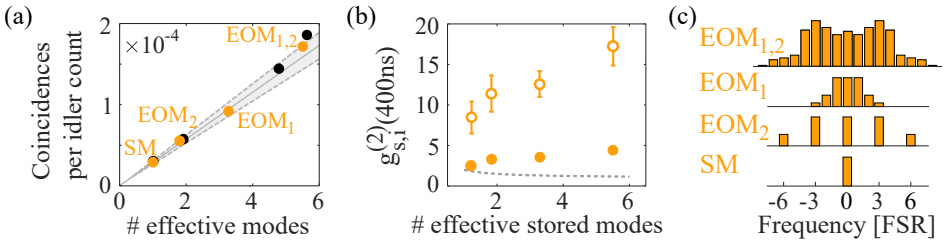

Figure 8.3: (a) Normalized coincidences between idler detections and signal photons, either after being transmitted through a spectral pit (black dots) or being stored (orange dots), versus number of effective modes N_{eM}. The gray line is a linear regression fixed to pass through the origin and the first orange point ($N_{eM} = 1$), the gray area being the error. The coincidence rate after the spectral pit is multiplied by the storage internal efficiency ($\eta_{AFC} = 8.5\%$), to compare all the results with the same line. (b) $g^{(2)}_{s,i}$ versus number of effective stored modes. The orange full (empty) points are measured with P=3 mW (1 mW). The gray dotted line is the theoretical classical limit, which scales with the number of modes N as 1+1/N (the real bound would be lower, due to noise and a finite detection window of 400 ns). (c) Sketch of the different EOMs configurations.

When increasing N_{eM}, the coincidence rate increases linearly, as expected. The same measurement is performed by preparing a multimode spectral pit (black dots in fig. 8.3(a)). For each EOM configuration considered in

fig. 8.3(a), we also measure the cross-correlation of the AFC echo (full points of fig. 8.3(b)). In this case, the $g^{(2)}_{s,i}$ increases with N_{eM} because, even if both the coincidences and the stored noise increase linearly, there is a part of uncorrelated noise (due to dark counts or broadband noise), which remains constant (see sec. D.9 in Appendix).

8.5 Temporal beating between spectral modes

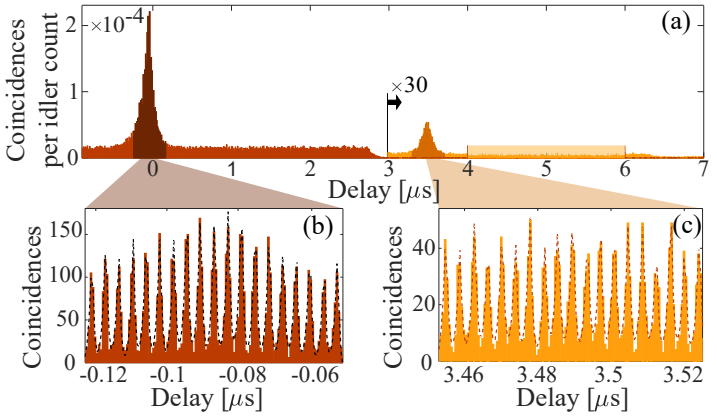

Figure 8.4: (a) Temporal coincidence histogram between idler and signal photons after the source (brown) or after storage (orange). The rectangle between 4 and 6 μs is the stored noise, i.e. the accidental counts $p_s p_i$ in the $g^{(2)}_{s,i}$ of the AFC echo (the accidental counts for the input are measured before the brown peak). (b), (c) zoom in the peaks, where the beating between the spectral modes is visible.

We now study the spectrum of our signal photons, before and after the storage. A signature of the presence of different frequency modes is the beating between them in the temporal $g^{(2)}_{s,i}$ function (fig. 8.4(a)). As described in the supplementary material of [106], the $g^{(2)}_{s,i}$ in the case of doubly-resonant CSPDC takes the form:

$$g^{(2)}_{s,i}(\tau) \propto \left| \sum_{m_s,m_i=0}^{\infty} \begin{cases} e^{-2\pi\Gamma_s(\tau-(\tau_0/2))}\mathrm{sinc}(i\pi\tau_0\Gamma_s) & \tau \geqslant \frac{\tau_0}{2} \\ e^{+2\pi\Gamma_i(\tau-(\tau_0/2))}\mathrm{sinc}(i\pi\tau_0\Gamma_i) & \tau < \frac{\tau_0}{2} \end{cases} \right|^2, \qquad (8.1)$$

where $m_{s,i}$ are the mode indices, τ_0 is the transit time difference between the signal and idler photons through the SPDC crystal and $\Gamma_{s,i} = \gamma_{s,i}/2 + i\, m_{s,i}\, \mathrm{FSR}_{s,i}$, being $\gamma_{s,i}$ the cavity damping rates for signal and

idler and $\mathrm{FSR}_{s,i}$ their free spectral ranges. The expected beating in the $g^{(2)}_{s,i}$ histogram, thus, has a periodicity of $\sim 1/\mathrm{FSR} = 3.8\,\mathrm{ns}$. We thus recalculate the histograms with increased resolution (fig. 8.4(b) before the storage, fig. 8.4(c) after). The clear beating in the AFC echo, with the expected periodicity, is a strong signature that the storage protocol preserves the frequency multimodality of the photon. We show in the Appendix, sec. D.4, that if we store only one frequency mode (SMs) the beating disappears as expected.

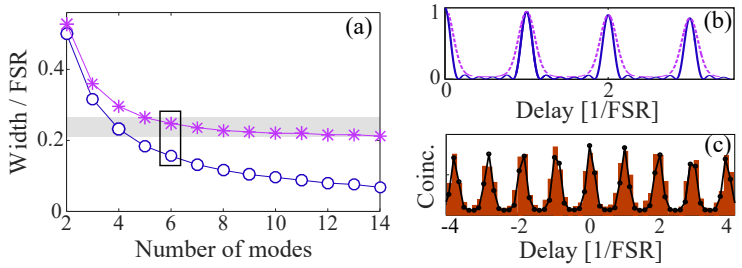

Figure 8.5: (a) In blue (empty circles), the theoretical prediction of the scaling of the ratio between the width of our beating and the FSR of our source versus the number of spectral modes interfering. In purple (stars), the expected behavior given our experimental jitter. The shaded area corresponds to the points compatible with the error of the fit reported in fig. 8.4(b). (b) Comparison of the simulated beatings for 6 spectral modes with (dotted line) and without jitter (solid line). (c) Same histogram as the one of fig. 8.4(b). Here the line corresponds to the simulated behavior expected for 6 spectral modes.

From eq. 8.1 we expect the width of the oscillation peaks to decrease with the number of spectral modes interfering. The width (in FSR unit) vs the number of modes is reported as blue empty circles in figure 8.5(a) (the solid line in panel (b) representing the corresponding interference peaks). We expect a width of 600 ps for a beating of 6 spectral modes (close to our effective stored modes). This is comparable to the time jitter of our detection system, namely 730 ps (measurement in Appendix D.3). If we convolute the theoretical beating (blue solid line in the inset) with the measured jitter (fig. D.3 of the appendix), the expected width of the beating peaks increases, as can be seen in purple in fig. 8.5 (stars in panel (a) and dotted line in (b)). The shaded area in fig. 8.5(a) is the width of the beating-peaks extracted from the fits in panels (b) and (c) of fig. 8.4, namely 910 ps, which agrees with the 970 ps expected when taking the jitter into consideration.

From this measurement it is difficult to extract the number of spectral modes involved, but we can give a lower bound of 5. Moreover, without making any consideration on the temporal jitter of our detection system, we can infer that the interfering modes are at least 4 (being our measurement compatible with the theoretical expectation for 4 modes, blue line of fig. 8.5(b)). Figure 8.5(c) reports the same beating histogram shown in fig. 8.4(b). In this case the black line is the expected beating for 6 modes, taking into account our jitter (purple dotted line of fig. 8.5(b)), plotted with the same bin-size of the measured histogram (567 ps).

8.6 Biphoton spectrum scanning the filter cavity

To quantify the number of generated and stored frequency modes we send the idler photons into the FCav (fig. 8.1(a)) that we scan about 4 GHz to cover its whole spectrum. We thus herald different signal frequency modes at different times. The coincidences detected before and after the storage are plotted in figs. 8.6(a) and 8.6(b) in brown and orange, respectively. In the SMs case, we just detect coincidences when the FCav is in resonance with the stored mode (fig. 8.6a); if we switch on the two EOMs (MMs), we can store and retrieve the whole spectrum of the signal photon (fig. 8.6(b)), i.e. about 15 spectral modes. As the spectrum of the preparation beam is almost flat for the nine central modes (fig. 8.1(d)), the biggest part of the spectrum is stored with the same efficiency of the SMs case. Despite the lower preparation power, also the other modes are stored with comparable efficiencies (see Appendix D.2).

We quantify the similarity between the normalized spectrum of the heralded photon before and after the storage from the measurements shown in fig. 8.6(b). To do so we create one idler list for each spectral mode. In this way we want to post process a single mode idler case. In the Appendix (sec. D.7) we show that the analysis is not equivalent to having a single-mode configuration in the idler, due to the cross-talk between the modes. However we can compare the coincidence rates (fig. 8.6(c)) and $g^{(2)}_{s,i}$ (fig. 8.6(d)) for each frequency mode, between the post-processed idler lists and the signals in three different cases: just the source, black bars in the plots; sending the signals through spectral pits, brown bars; storing

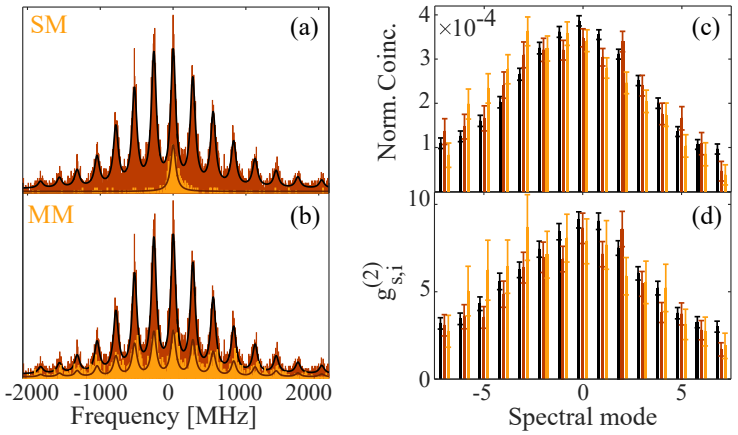

Figure 8.6: (a)-(b) Heralded signal detections triggered to the scan of the FCav in the case of SM and MM storage, respectively. The brown (orange) histogram is measured with the source alone (after the storage). The solid lines are fits to the brown histogram, renormalized to overlap with the orange trace (see sec. D.6 in appendix for more details). (c) Relative amplitude of the count rates if we isolate the contribution of each spectral mode in post processing. The black and brown bars are renormalized to the average of the orange ones in order to better compare the spectrum. (d) Cross correlation of each spectral mode after post processing individually each of them. In both (c) and (d) the signal photons are measured right after the source (plotted in black), after passing through a spectral pit (brown bars) and after the AFC (orange bars).

the signals with AFC, light orange bars. From both plots, it is possible to see that the shape of the spectrum is maintained after the storage.

We call $\mathbf{CR}_{\mathrm{CSPDC}}$ the vector containing the coincidence rates between the signals and idlers for each spectral mode with just the source (black bars in fig. 8.6(c)) and $\mathbf{CR}_{\mathrm{AFC}}$ the one measured after the storage (light orange bars). $\mathbf{CR}_{\mathrm{CSPDC}}$, in the figure, is normalized to the average $\mathbf{CR}_{\mathrm{AFC}}$ in order to compare the two spectra. The two vectors are then normalized as: $\mathbf{CR}_x = \mathbf{CR}_x/\sqrt{\mathbf{CR}_x \cdot \mathbf{CR}_x}$. We quantify the overlap between the spectrum before and after the storage by measuring the scalar product between the vectors $\mathbf{CR}_{\mathrm{CSPDC}}$ and $\mathbf{CR}_{\mathrm{AFC}}$. We find $\mathbf{CR}_{\mathrm{CSPDC}} \cdot \mathbf{CR}_{\mathrm{AFC}} = 0.97 \pm 0.03$. The overlap has been measured in the same way for the $g^{(2)}_{s,i}$ measurement, again with the $g^{(2)}_{s,i}$ between signal and idler measured with just the source ($\mathbf{g}^{(2)}_{s,i\,\mathrm{CSPDC}}$, black bars in fig. 8.6(d)) and after the storage ($\mathbf{g}^{(2)}_{s,i\,\mathrm{AFC}}$, light orange bars). We find $\mathbf{g}^{(2)}_{s,i\,\mathrm{CSPDC}} \cdot \mathbf{g}^{(2)}_{s,i\,\mathrm{AFC}} = 0.98 \pm 0.06$. As in the previous case, each vector is renormalized to its modulus.

The spectrum of the stored and retrieved photons has been measured in the different EOMs configurations (see sec. D.8 of the Appendix).

8.7 Discussion, conclusions and outlook

The multimode storage technique demonstrated in this paper is directly suitable for storing the frequency bin entanglement naturally generated by our source [196]. For that purpose it is desirable to reach higher values of $g^{(2)}_{s,i}$. An easy way to increase the $g^{(2)}_{s,i}$ without destroying the entangled state is to reduce the pump power of the source (as shown in fig. 8.2). We measure the $g^{(2)}_{s,i}$ versus N_{eM}, for P = 1 mW (empty orange points in 8.6(d)). Despite the fact that the coincidence rate decreases with P, the $g^{(2)}_{s,i}$ increases remarkably with respect to the previous measurement. The $g^{(2)}_{s,i}$ would increase further by filtering broadband noise before the idler detection with an etalon.

Another possible application of frequency multimode storage is to use each spectral channel as an independent quantum memory, leading to spectral multiplexing, e. g. for quantum repeaters (sec. 1.2). For this purpose we should distinguish the different heralding frequency modes, i.e. separate the modes of the idler photon [201]. This would destroy the frequency bin entanglement, but the count rate and duty cycle of the experiment would increase, without decreasing the $g^{(2)}_{s,i}$. We perform a series of measurements to validate our statement. In table 8.1 we compare the $g^{(2)}_{s,i}$ measured with a single mode (SM_i) or multimode heralding photon (MM_i), storing either one mode (SM_s) or the whole spectrum (MM_s) of the signal photon.

SM_s	MM_i	2.48 ± 0.17
MM_s	MM_i	4.35 ± 0.22
MM_s	SM_i	15.8 ± 1.5
SM_s	SM_i	72 ± 12

Table 8.1: Measured $g^{(2)}_{s,i}$ after storage in different configurations for P = 3 mW.

We note that, by distinguishing the spectral modes of the heralding detections (SM_i), the $g^{(2)}_{s,i}$ of the retrieved multimode echo would increase. Moreover, if we could retrieve independently the different modes of the signal (fourth case), the $g^{(2)}_{s,i}$ for each spectral mode would be increased by

a factor of 16, without decreasing the experiment count rate. With current technology it is challenging to distinguish the different idler frequency modes due to their small separation. Being able to do it, we could find different applications for the signal photon stored into the memory. For example we could perform spin-wave storage [88, 28] addressing spin-states for each frequency mode individually, e.g. using serrodyne frequency shifting of the control beams [202], having therefore a SM_s SM_i configuration.

In conclusion, we demonstrated quantum storage of a frequency multiplexed single photon, counting 15 spectral modes over 4 GHz, in an integrated rare-earth-doped laser-written waveguide. Our work opens prospects for the realization of frequency multiplexed quantum repeaters, and for the demonstration of high dimensional frequency entanglement between light and matter. Together with the 9 temporal modes stored as an intrinsic property of the AFC protocol, we demonstrate the storage of more than 130 individual modes. Our results show that integrated waveguides in rare-earth doped crystals can be used as versatile light-matter interaction platforms with both time and frequency multiplexing capabilities. Moreover, the unique 3-dimensional fabrication capability of laser-written waveguides [203] also holds promises for implementing large memory arrays in one crystal and allows fabrication of optical angular momentum compatible waveguides [204]. The ability to combine several multiplexing capabilities in one system would open the door to the realization of massively multiplexed quantum memories.

This experiment is a rather complete highlight of the advantages of our system. The generation of narrowband, highly-nondegenerate photons in CSPDC naturally results in frequency-multiplexed photons. In REDCs we can take advantage of the intrinsic inhomogeneous broadening to store the whole spectrum of the photon. Moreover, solid-state systems allow us to implement integrated devices. The confinement of light given by waveguides increases the light-matter interaction by a factor of 10. Thanks to it we can generate simultaneously one AFC per spectral mode of the multiplexed heralded photon without loosing in preparation time or measurement duty cycle, one of our biggest limiting factors at this moment. These waveguides can provide high spatial multimodality (thanks to the 3-dimensional capability of fs-laser micromachining); namely we can have one fiber pigtailed waveguide type I each 127 μm ($\sim$ 62 waveguides per

mm^2). The AFC protocol is the best candidate for temporal multimodality (as shown in Chapter 5). Finally, the problem of demultiplexing the stored frequency modes could be solved with spin-wave storage, which would allow us to retrieve the photons separately and on-demand.

Chapter 9

Conclusions and Outlook

The work presented in my thesis followed two main paths. The first one was to realize a multimode quantum memory for real single photons based on a solid state system. Secondly, we wanted to demonstrate quantum storage on a new kind of integrated memory. The memory used in all the experiments is based on a rare-earth doped crystal, namely Pr^{3+}:Y_2SiO_5. This crystal already showed great promise, due to its long storage times [72], high efficiency [65] and on-demand operation at the single photon level [24]. Here I summarize the main results of the thesis and, then, I give an outlook for the next possible steps, both on the short and long term.

9.1 Main results of the thesis

Firstly we measured non-classical correlations between a single spin wave in a quantum memory and a telecom photon. In this experiment, published in [28] and reported in Chapter 5, we demonstrated half a node of the quantum repeater link described in sec. 1.2.2. The used protocol, the atomic frequency comb (AFC) technique, is intrinsically temporal multimode. This allowed us to store and retrieve on demand 14 temporal modes in a long-lived state. This experiment represented the first (and only until now) absorptive quantum memory for real quantum states of light based on rare-earth doped crystals.

A main reason to invest on solid-state quantum systems is their easier scalability and miniaturization, which would bring the idea of a quantum internet closer to a physical realization. This motivated our parallel research projects aimed at demonstrating new kinds of integrated memories.

In these works, carried out in collaboration with Dr. Roberto Osellame and Dr. Giacomo Corrielli at Politecnico di Milano, we demonstrated two different kinds of laser-written waveguides, called type II and type I. These waveguides have been fabricated by our collaborators with fs-laser micromachining. In both types we could show that the fabrication does not significantly degrade the coherence and spectral properties of the ions and we demonstrated spin-wave storage of classical light. These results, as measured in the type II waveguide, are published in [137] and reported in Chapter 6. In the type I waveguide we moved forward, demonstrating the storage of heralded single photons for a pre-programmed storage time in the excited state of the ions and measuring the longest quantum storage achieved in an integrated memory, about 100 times longer than any other demonstration with single photons up to now. These results are published in [116] and reported in Chapter 7.

Waveguide-based memories provide an increase in the light-matter interaction, resulting from the tight confinement of the guided light along the whole length of the crystal. This important advantage, together with the large inhomogeneous broadening present in rare earth doped crystals, allowed us to store the whole spectrum of a frequency-multiplexed photon (15 modes), spanning about 4 GHz of frequency. This experiment is reported in Chapter 8 and published in [40]. There we could demonstrate a storage of about 130 modes, 15 spectral and 9 temporal, in the excited state of the ions.

9.2 Outlook

Both research directions aimed at the same objective, namely realizing the quantum repeater link described in sec. 1.2.2. A few more steps are necessary to reach this ambitious goal. First of all, longer storage times have to be achieved. The quantum memory, in fact, has to store the quantum state for a time long enough for the heralding telecom photon to travel to the measurement stage and for the information on the detection event to come back to the station where the memory is placed, the lab in the first instance of the experiment. For a distance of 50 km between the memory station and the detection stage, we would need a minimum storage time of about 500 μs, which corresponds to the T_2 of the spin transition

in Pr^{3+}:Y_2SiO_5. In order to reach this storage time, it is required to overcome the inhomogeneous broadening of the spin transition, that can be done thanks to spin echo techniques. Longer storage times can be achieved in our system by means of dynamical decoupling techniques and, if necessary, by applying external magnetic fields to reach the ZEFOZ points (sec. 2.2.2).

A second necessary step will focus on increasing the successful count rates detected after the memory. This can be done by improving the storage efficiency and multimodality. One way to increase drastically the efficiency of our memory could be to embed it in an impedance-matched cavity [77]; in our system and at the actual conditions we could arrive to $> 80\%$ storage efficiency, and this option is currently investigated as the PhD project of a student in our group. On the short term we can further improve the linewidth of our preparation laser and our AFC preparation sequence. A notable limiting factor for the latter is the limited preparation time imposed by the cryostat cycle. This would not be present in the case of a fiber-pigtailed waveguide-based memory.

In fact, the next natural step for type I waveguides will be the demonstration of a fiber-pigtailed memory. This will be an improvement in terms of mechanical stability of the system (which could become independent on the cryostat cooling cycle), optical alignment and scalability. On the long term, this demonstration would open the way to embedding our quantum memory in more complex optical circuits. Moreover, working in waveguides would allow us to fabricate matrices of spatially multiplexed memories, thanks to the unique 3D capability of the laser-writing technique [203].

Finally, the demonstration of spin-wave storage at the single photon level in an integrated quantum memory will be a fundamental step to boost waveguide-based quantum memories beyond their equivalent in bulk crystals. Spin-wave storage is already a very challenging task in bulk crystals because of the noise generated by the strong optical control pulses (see Chapter 5). Filtering this noise becomes more difficult in waveguide, as spatial filtering is not as straightforward as in the bulk case. Nevertheless, a fiber-pigtailed memory, where the protocol-preparation light is uniformly coupled along the whole cryostat cooling cycle, would allow us to

optimize the preparation sequence to further reduce the atomic population in the spin-state, decreasing the fluorescence generated by the control pulses. Moreover, a longer filter crystal would increase the extinction ratio of the spectral filter. In case of a successful spin-wave storage of heralded photons, we could demonstrate an AFC-DLCZ memory in waveguide, which was already demonstrated in a bulk Pr^{3+}:Y_2SiO_5 [29] and in another rare-earth doped crystal [30]. The possibility to have an integrated emissive quantum memory based on our waveguides would pave the way to a scalable spatially-multiplexed quantum repeater, as the memory would provide itself the heralding photon. Matrices of quantum memories, moreover, would provide a very important tool for the generation of multi-photon states [205] and cluster states [206].

The experiment on frequency-multimode storage described in Chapter 8 can follow two different paths. One would be the demonstration of frequency multiplexing in a real quantum repeater scenario. As pointed out in sec. 8.7, unfortunately, the frequency modes of the heralding photons are too close in frequency to be easily separated with present day technology, meaning that currently we cannot herald separately the different frequency modes of the stored signal to be retrieved. Nevertheless, with the technique used in the present experiment we can demonstrate light-matter frequency entanglement, namely entanglement between a frequency multiplexed telecom photon and collective atomic excitations at different frequencies. In fact, this entanglement should be preserved by the storage protocol, as almost the whole spectrum of the photon is stored uniformly and all the frequency modes are retrieved at the same time. This entanglement has already been demonstrated with our photon-pair source [196]. A violation of the Bell inequality was also demonstrated in the context of the Big Bell Test, a worldwide quantum experiment involving many research groups, powered by human randomness [207]. I took part to that experiment, helping to automatize the software.

Until now we have demonstrated storage of up to 130 modes (Chapter 8). In Appendix E I show that we could store more than 10^5 different modes in our system, among the temporal, spectral and spatial domains. Provided that in a realistic situation we have to account for photon losses through the fiber, finite storage efficiencies and non-perfect optical elements and

detectors, such high multimodality will be necessary to realize a quantum repeater scheme with success probability per attempt very close to 1.

Appendix A

Further details for Chapter 5

A.1 Control Pulses

The waveform that we use to generate our control pulses (CPs) is a Gaussian (blue dashed trace in fig. A.1) with full-width at half maximum FWHM = 2.4 μs. As the AOM that we use to modulate the amplitude and frequency of the pulses has a non-linear response, the output waveform looks more squarish (gray solid trace). The FWHM, though, remains almost the same. This shape increases the efficiency of the CPs, so that we can take advantage of having shorter waveforms. This is important in particular for the semi-conditional storage (section 5.4.3), in which we have to send the CPs as fast as possible after the heralding detection. In this case using longer waveforms means having the second CP closer to the echo, thus increasing the noise floor. These CPs are frequency chirped with a hyperbolic tangent (red dotted trace in fig. A.1), that makes the transfer more effective around the central frequency [208, 209].

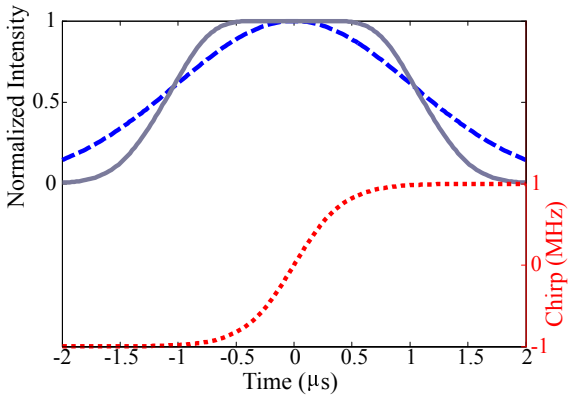

Figure A.1: Control pulse waveform. The blue dashed trace is the waveform fed into the AOM. The resulting shape of the CPs looks like the gray solid trace. The CPs are chirped following the red dotted trace.

The transfer efficiency of the control pulses η_T is measured by preparing an AFC and sending the first control pulse before the rephasing of the atoms: calling η_{AFC} the efficiency of the AFC storage and η'_{AFC} the efficiency of the AFC rephasing after the control pulse, we have: $\eta_T = 1 - \frac{\eta'_{AFC}}{\eta_{AFC}} = (72.5 \pm 1.3)\,\%$.

A.1.1 Noise generated by the control pulses

We use a semi-conditional sequence (explained in more detail in section 5.4.3) to measure the noise generated by the first control pulse and by both of them. Each time that we detect a heralding photon we send a CP, then the temporal gate is opened in the position of the AFC echo and closed before the second CP is sent. We open it again and measure the noise generated by both pulses in the temporal mode of the spin wave echo (fig. A.2). The noise generated by the first control pulse is higher than the noise after both CPs. Specifically the noise after the two CPs (red trace around 18 μs) is $(2.3 \pm 0.1) \times 10^{-3}$ photons per storage trial, i.e. 86% of the noise after the first CP (red trace about 7.3 μs), measured in the position of the AFC.

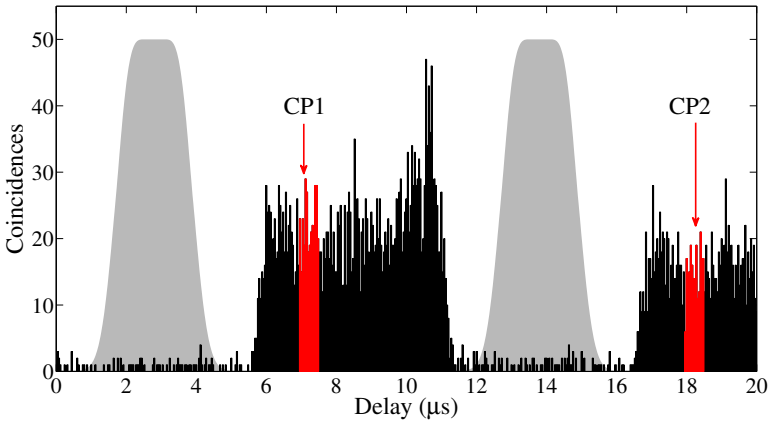

Figure A.2: Trace of the noise generated by one control pulse (CP1 is the temporal mode of the AFC echo) and by both control pulses (CP2 being the position of the spin wave echo).

If the $3/2_g$ spin state is not well cleaned, a portion of the remaining atoms depending on the transfer efficiency, is promoted to the excited state by the first control pulse, possibly giving rise to incoherent fluorescence. This

excess of population at the excited state might then be coherently transferred to the ground state by the second control pulse, thus decreasing the contribution to the noise.

A.2 Comb analysis

The efficiency of the AFC echo can be predicted by analyzing the trace of the comb (fig. 5.4(c)) according to the model described in ref. [68]. Assuming Gaussian peaks, we express the AFC internal efficiency with the following equation:

$$\eta_{AFC}^{int} = \tilde{d}^2 e^{-\frac{7}{F^2}} e^{-\tilde{d}} e^{-d_0},$$

where $\Delta = 1/\tau$ is the distance between the peaks of the comb, γ is their full width at half maximum, $F = \Delta/\gamma$ is the comb finesse, $\tilde{d} = OD/F$ is the effective optical depth, and d_0 is the absorption background due to imperfect optical pumping. The total efficiency that we measure is reduced by a factor $\eta_{BW} \approx 66\,\%$, due to the bandwidth mismatch between photons and comb (see sec. 5.3). Assuming for the comb reported in fig. 5.4 a finesse $F = 3.8 \pm 0.3$, average optical depth and linewidth of the peaks $OD = 3.5 \pm 0.2$ and $\gamma = (36 \pm 3)$ kHz, respectively, and a background $d_0 = 0.27 \pm 0.1$, the expected total efficiency is $\eta_{AFC} = (10.7 \pm 1.3)\,\%$ which agrees very well with the experimentally measured $\eta_{AFC}^{exp} = (11.0 \pm 0.5)\,\%$. With the same comb parameters, the expected internal efficiency, assuming no loss due to the bandwidth mismatch, would be $\eta_{AFC}^{int} = (16 \pm 2)\,\%$.

The AFC efficiency can be separated into different contributions as follows:

$$\eta_{AFC} = \eta_{abs}\eta_{reph}\eta_{loss},$$

where η_{abs} (η_{reph}) is the absorption (rephasing) efficiency of the comb. The factor η_{loss} accounts for the loss due to absorption in the background. The absorption efficiency in the comb can be calculated as $\eta_{abs} = (1 - e^{-\tilde{d}})\eta_{BW} = 43\,\%$. The rephasing efficiency of the comb is thus $\eta_{reph} = 34\,\%$.

The spin wave efficiency can be analogously expressed as $\eta_{\mathrm{SW}} = \eta_{\mathrm{AFC}}\,\eta_{\mathrm{T}}^2\,\eta_{\mathrm{C}}$, assuming the transfer efficiency η_T be the same for both control pulses and the spin state exhibit a Gaussian inhomogeneous broadening leading to a decoherence effect quantified by $\eta_C = exp\left(-\frac{(T_s \cdot \Gamma_{inhom})^2}{2 \cdot log(2))} \cdot \pi^2\right) = 87.3\,\%$

[88, 89, 24]. The expected value of the spin wave efficiency is $\eta_{sw} = (5.2 \pm 0.6)\,\%$. The small mismatch with the experimentally measured one, $\eta_{sw}^{exp} = 3.6 \pm 0.2\,\%$, can be due to the fact that our chosen coincidence window, ΔT_d, contains about 80 % of the echo and that the filter crystal might have residual background due to imperfect optical pumping.

Given the control pulse efficiency $\eta_T = 72.5\,\%$ (see section A.1), we define a spin wave write and read-out efficiency as $\eta_W = \eta_{abs}\eta_T$ and $\eta_{RO} = \eta_T\eta_{reph}$, respectively (thus rewriting the total spin-wave efficiency as $\eta_{sw} = \eta_{loss}\eta_W\eta_C\eta_{RO}$), which we estimate to be 31 % and 24 %, respectively. Taking this into account and considering that the first control pulse gives a measured noise floor of $(2.3 \pm 0.1) \times 10^{-3}$, we infer non-classical correlation between the single telecom photons and the collective spin excitations during the storage with a $g_{sw,i}^{(2)}$ of the order of 20.

A.3 $g_{s,i}^{(2)}$ and $\eta_{\mathbf{AFC}}$ for different detection windows

In this section we show a plot of the measured $g_{swe,i}^{(2)}$ value, along with the spin wave efficiency, as a function of the integration window $\Delta(t_s)$. The results are shown in fig. A.3(c).

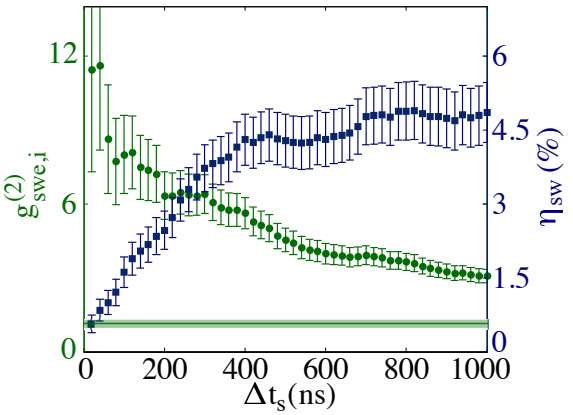

Figure A.3: Second order cross-correlation between idler and retrieved signal (circles) and spin-wave echo efficiency (squares) as a function of the integration window, Δt_d.

Appendix B

Further details for Chapter 6

B.1 Type II waveguide fabrication

Each track is fabricated by focusing a femtosecond laser beam (a home made Yb:KYW oscillator, λ=1030 nm, pulse duration τ=300 fs) inside the crystal volume, with optimized irradiation parameters: energy per pulse of 570 nJ, repetition rate of 20 kHz, uniform sample translation along the *b*-axis at the speed of 57 μm/s. A microscope objective with 50x magnification and 0.6 numerical aperture is used as focusing optics. Note that, for higher laser repetition rates and equal energy deposited per unit volume (at a fixed pulse energy) we observed the formation of periodic disruptions along the damage tracks [210], which degrade the waveguide homogeneity and increase significantly the waveguide propagation losses. During the fabrication, the crystal orientation is such that the fs-pulsed laser beam is parallel to the D_1-axis.

B.2 Type II waveguide characterization

We characterize the transmission through the waveguide for different powers (fig. B.1(a)) and for different polarization (fig. B.1(b)). In both the measurements we couple into the waveguide our laser @ 606 nm in CW. In fig. B.1(a) we can see that the coupled light is linearly proportional to the input light. The coupling efficiency, i.e. the ratio between the measured power after and before the waveguide, is, in average, $\sim 50\%$.

In fig. B.1(b) we show that the guiding property of the waveguide is highly dependent on the polarization of the coupled light. In fact, just a specific linear polarization is guided. The measured extinction ratio between the two orthogonal polarization coupled into the waveguide is 98% (99.9% from the fit).

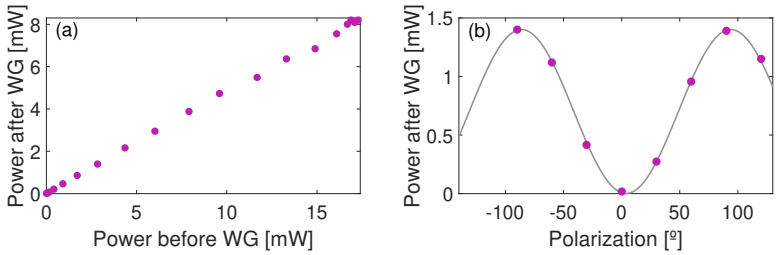

Figure B.1: Measured intensity of CW light at 606 nm after being coupled in a type II waveguide plotted either versus the input power (a), or versus the incoming polarization (b).

B.3 Inhomogeneous broadening

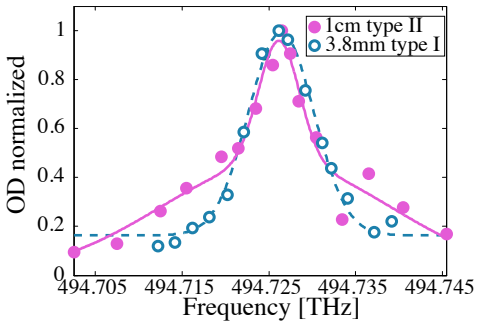

Figure B.2: Inhomogeneous broadening measured in optical depth OD. The purple points are measured in the 1 cm sample, the empty circles are measured in a new sample 3.8 mm long.

We measure the OD of the ions in our waveguides around the usual center of their inhomogeneous broadening ($\sim$ 494.726 THz). The same measurement has been performed both for the type II waveguide in the 1 cm sample (see Chapter 6) and for the type I waveguide in the 3.7 mm sample (Chapters 7 and 8). The center of the inhomogeneous broadening is not shifted in any of the waveguides, and the width of the absorption line is consistent with the usual values measured in crystals with the same doping concentration. The double Gaussian measured for the type II was measured also in the same bulk sample before the fabrication of the waveguides. One possible explanation for the broader inhomogeneity, as explained in the main text in section 6.5, is an unwanted amount of LSO impurities in the YSO substrate [173].

B.4 T_2 in the new sample

We measured the coherence time of the optical transition $\pm 1/2g \rightarrow \pm 3/2e$ for the type II waveguides in the 3.7 mm sample (sec. 6.5). This has been measured for different powers and duration of the $\pi/2-$pulse while keeping fixed the OD of the prepared single-class transition (0.6).

The results are shown in fig. B.3, together with those of sec. 6.3.

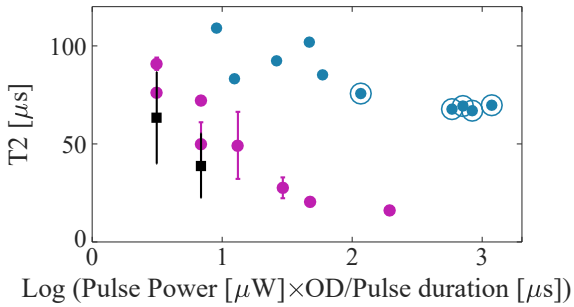

Figure B.3: Optical coherence times T_2 measured in the 1 cm (purple points, waveguide, and black squares, bulk, sec. 6.3) and in type II waveguides fabricated in a new sample (blue points, sec. 6.5), as a function of the quantity $\mathrm{Log}_{10}\left(\frac{OD \times P_p}{t_p}\right)$. The circled data points are the measurements considered to extract the mean T_2 reported in sec. 6.5.

Appendix C

Further details for Chapter 7

C.1 Type I waveguide fabrication

Type I waveguides have been directly written by FLM in the volume of a 3.7 mm long Pr^{3+}:Y_2SiO_5 crystal with a dopants concentration of 0.05%. A fs-pulsed laser, highly focused on the sample, is shined along the crystal D_1 axis, while the sample is translated along the b crystallographic direction. The laser pulses are focused 100 μm below the sample top surface. The optimal irradiation parameters for obtaining high quality optical waveguides which supports a single optical mode at the wavelength of 606 nm are reported in the Supplemental Material of the paper [28].

C.2 Type I waveguide characterization

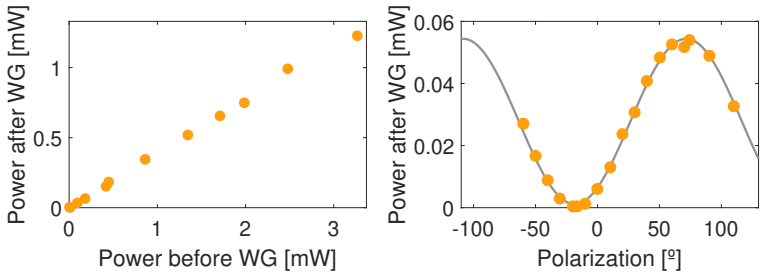

Figure C.1: Measured intensity of CW light at 606 nm after being coupled in a type I waveguide plotted either versus the input power (a), or versus the incoming polarization (b).

We characterize the transmission through the waveguide for different powers (fig. C.1(a)) and for different polarization (fig. C.1(b)). In both the measurements we couple into the waveguide our laser @ 606 nm in CW. In fig. C.1(a) we can see that the coupled light is linearly proportional to the input light. The coupling efficiency, i.e. the ratio between the measured

power after and before the waveguide, is, in average, $\sim 40\%$. The maximum transmission achieved without the cryostat for the same waveguide and with the same optics is $\sim 60\%$. The coupling drops down to $\sim 40\%$ as soon as we close the cryostat, probably due to a distortion in the beam profile given by the windows of the cryostat.

In fig. C.1(b) we show that the guiding of the waveguide is highly dependent on the polarization of the coupled light. In fact, just a specific linear polarization is guided (along the crystal D_2, interacting with Pr^{3+} ions in site 1). The measured extinction ratio between the two orthogonal polarization coupled into the waveguide is 99% (98% from the fit).

C.2.1 Coupling during the cryostat cycle

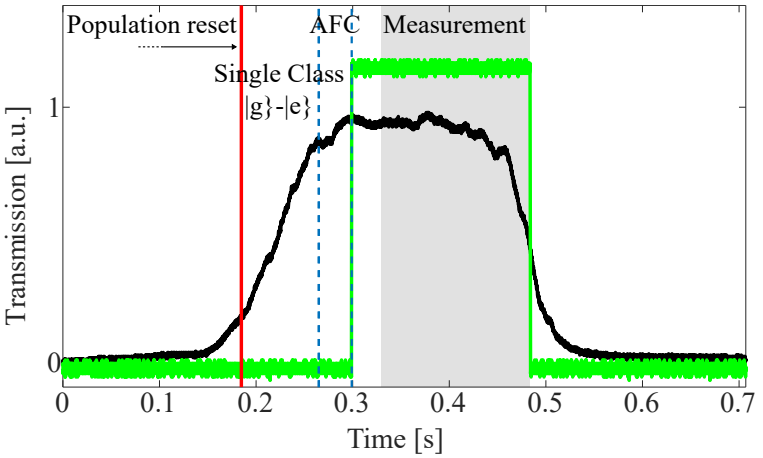

Figure C.2: Measured intensity of CW light coupled to the type I waveguide during the cycle of the cryostat. The vertical lines define the different stages of the optical sequence for the preparation of a single-class AFC feature. The green trace is the TTL signal used to gate the APDs and the mechanical shutters during the single photon measurements. The gray rectangle defines the time during which the measurements are performed.

Due to vibrations induced by the cryostat, we can optimze the coupling of light into the waveguide for a limited amount of time per cycle. Fig. C.2 shows the transmission of CW light coupled into the waveguide and measured after an imaging path of about 2m (see fig. 7.2).

C.3 Spectroscopic and coherence properties

C.3.1 Level scheme via hole burning

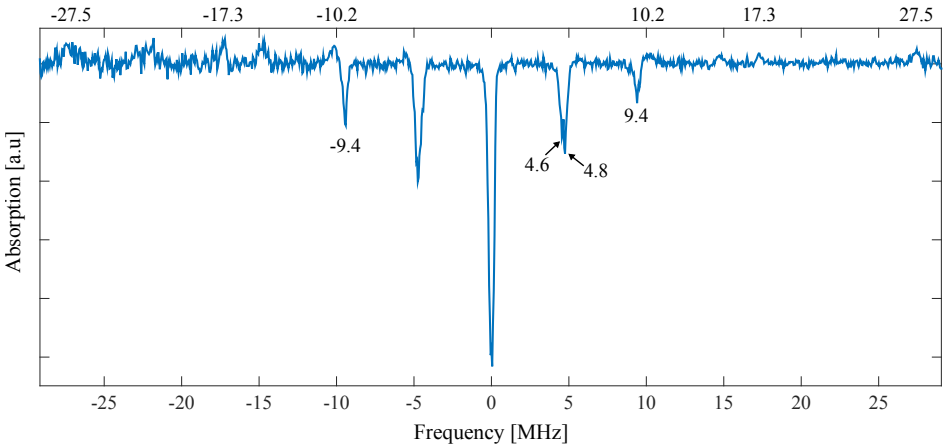

Figure C.3: Holes and antiholes generated in the absorption line of a Pr^{3+}:Y_2SiO_5-based waveguide with spectral hole burning shining a pulsed sequence at frequency 0.

A single spectral hole is generated within the inhomogeneous profile of a Pr^{3+}:Y_2SiO_5-based waveguide type I. The process is explained in sec. 3.2. When a hole is generated in the absorption line of the ions (at 0-frequency of fig. C.3), from the resulting holes and antiholes it is possible to reconstruct the level scheme of the ions involved, as highlighted in fig. C.3.

C.3.2 Relative oscillation strength of the transitions

Here we measure the relative oscillation strength of the transitions of interest in a Pr^{3+}:Y_2SiO_5-based waveguide type I, following the measurements described in [135]. The results are shown as blue empty points in fig. C.4. The red points, for comparison, are the values reported in [135].

We start by creating a spectral pit and applying a burn-back pulse, as described in sec. 3.2.2. As a first measurement we empty the $\pm 1/2g$ level for a single class of atoms. With a burn-back pulse we repopulate it. We then read with a weak pulse the antiholes relative to the three transitions starting from the $\pm 1/2g$ state. In transmission we measure the area of these generated antiholes and we reconstruct the relative strength of the

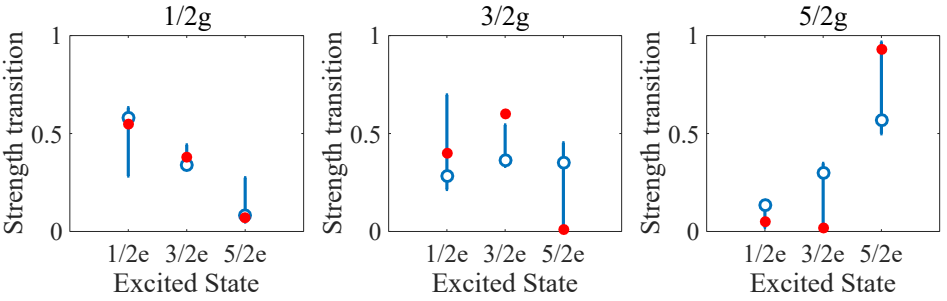

Figure C.4: Relative oscillation strength of the transitions shown in fig. 2.2. The points refer to transitions between the ground states indicated at the top of the three figures and the excited states written in the x-axis of the plots. In blue we report the data measured in our sample, in red the values published in [135] for comparison.

three transitions. The sum of their oscillation strengths is renormalized to 1. The same is done for single class transitions starting form the $\pm 5/2g$ level. The oscillation strength of the transitions starting from the level $\pm 3/2g$ are derived from the other 6, thanks to the fact that the strength of the three transitions arriving to the same excited level also are normalized to 1 [135].

C.3.3 T_1 from fluorescence

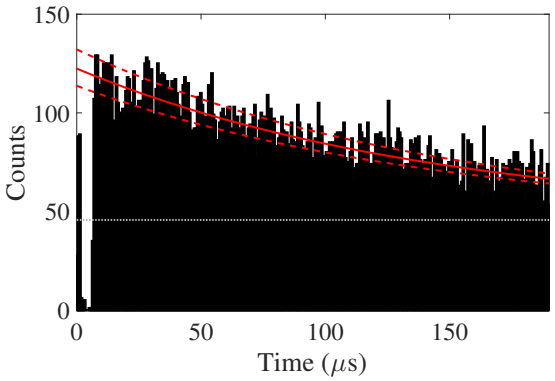

Figure C.5: Fluorescence measurement. Decay of the population (black histogram) excited to $|e\rangle$ by a Gaussian pulse at time 0 (leakage in the black histogram). The AOM, used as a fast temporal gate, is switched on after $\sim 10\,\mu$s. The gray dotted line is the offset of our measurement, measured switching on the AOM without sending any transfer pulse. The red solid line is an exponential fit to the decay, the dotted lines being the error of the fit.

In section 7.4 we measured the lifetime (T_1) and coherence time (T_2) of the ions excited in the $|g\rangle$-$|e\rangle$ transition by means of two-pulse and (three-pulse) stimulated photon echo. A more direct way of measuring the T_1, is performing a fluorescence measurement (see Section 3.1.6). As in sec. 7.4 we populate a single-class transition $|g\rangle$-$|e\rangle$. At time 0 we send a Gaussian pulse resonant with the transition. The population transferred to the excited state will decay to the ground-state, generating photons. We measure this decay with an SPD (fig. C.5). From the fit (red solid line) we estimate a $T_1 = 142 \pm 11\,\mu$s. For this measurement, an AOM was placed in front of the SPD and used as temporal gate, the +1 mode aligned to the detector, to prevent burning the SPD while sending the Gaussian pulse at time 0 (the leakage can be seen in fig. C.5).

C.3.4 Spin-inhomogeneity in the bulk sample

We measured the spin-inhomogeneity in the bulk of the sample in which the type I waveguides analysed in this Appendix has been fabricated. The optics used is not the same one used for coupling into the waveguide. The 75 mm lens of fig. 7.2 was removed, and the light was coupled into the sample using a 20 cm lens. The AFC was prepared for a storage time of $\tau = 2.5\,\mu$s ($\eta_{AFC} = 0.8\%$). The efficiency of the spin-wave echo was 0.3 % for $T_s = 5\,\mu$s. We measure a spin inhomogeneity smaller than what we usually measure in bulk samples with similar ion concentration. This is probably due to the presence of a layer of μ-metal inside the radiation shield of the cryostat, which reduces the external magnetic fields in the position of the memory crystal.

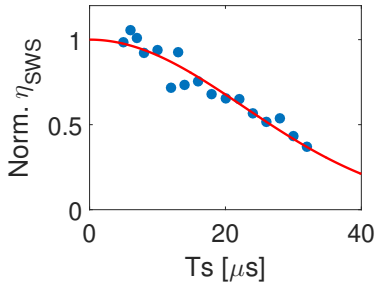

Figure C.6: Normalized spin-wave echo intensities vs T_s. From the fit to the experimental data (dots) we extract an inhomogeneous spin-broadening $\gamma_{inhom} = 12 \pm 1$ kHz.

Appendix D

Further details for Chapter 8

D.1 Frequency multiplexed photon pair source

To produce narrow single photons we embed a type-I periodically-poled lithium niobate (PPLN) crystal inside an optical cavity. The effect of a cavity around the crystal is that only photons compatible with the resonator spectrum (linewidth 1.8 MHz) will be generated. In our case, we pump the cavity-enhanced spontaneous parametric downconversion (CSPDC) source with a cw laser at 426 nm producing a pair of photons at 606 nm (signal) and 1436 nm (idler).

Having a double resonance with non-degenerate photons has a fundamental implication for this work. The refractive index of the nonlinear crystal is slightly different for 606 nm and for 1436 nm. This implies that the free spectral range (FSR) of the two different wavelengths, being the distance in frequency between the spectral modes transmitted by the cavity, will be also slightly different (as sketched in fig. D.1). Due to the double lock of the cavity, only the pairs where both photons are resonant are extracted. This creates a clustering effect [140]. The size of the cluster depends on the relation between the linewidth of the photons and the FSR. In our case the biphoton linewidth is measured to be 1.8 MHz and the FSR 261.1 MHz.

Measurements performed also within Chapter 8 with a spectrum analyser (FCav in fig. 8.1, linewidth = 80 MHz, FSR = 17 GHz) revealed that our source generates up to 15 spectral modes within the central cluster.

For our measurements we switch off the pump laser of the CSPDC source triggered on the detections of idler photons to reduce broadband uncorrelated noise while the AFC echo is expected. Before sending the signal

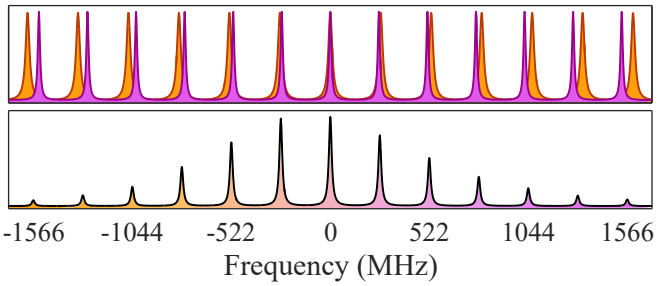

Figure D.1: Top: sketch of the spectral modes structure of the 606 nm photons (orange) and 1436 nm photons (purple) that have slightly different FSR inside our cavity. Bottom: sketch of the photon pairs generated inside the cavity, given by the overlap between signal and idler spectra. The linewidth of the individual modes was increased on purpose for the sake of clarity.

photon to the memory table, we filter it from broadband noise with an etalon (fig. 8.1(a), linewidth 4.25 GHz, FSR 100 GHz).

D.2 AFC efficiency and spectral pit transmission for different spectral modes

As we do not access independently the different spectral modes of the signal photons, the storage efficiency and the transmission through the spectral pit are not measured directly for each of them. Our calibration involves only the central mode: we prepare the AFC and spectral pit, in a single mode configuration ($EOM_{1,2}$ off), for different preparation powers. The results (measured with classical light) are shown in figs. D.2(a) and D.2(b), respectively. The power that we want to have, for each of the 9 central spectral modes of the preparation, is 160 μW before the waveguide (this is what we call 1 in the x-axis of the figures). For this power, in a single mode configuration, we measured an internal efficiency $\eta_{AFC} = 8.5\%$, reported as a dotted line in fig. D.2(a). This efficiency takes into account only the losses in the memory crystal, without considering the coupling efficiency in the waveguide (C = 40%). The total efficiency, called device efficiency, i.e. considering our device a black box, can be calculated dividing the light in the AFC echo time window measured after the cryostat by the input light measured in front of the cryostat. In practice this can be calculated from each point of fig. D.2(a) by multiplying $\eta^{int}_{AFC} \times$ C.

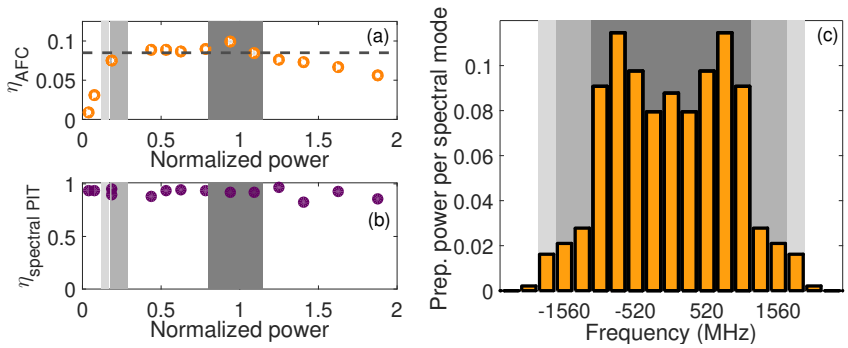

Figure D.2: Calibration measurements to estimate the expected efficiency of the pit and the AFC for the different spectral modes. (a) Dependence of the AFC efficiency on the power that we use to prepare it. (b) Dependence of the transmission efficiency through the pit on the power that we use to prepare it. For (a) and (b) in the x axis a value of 1 corresponds to the optimum value of power to send to the waveguide. (c) Amplitude (normalized to the input power) of the spectral modes of the preparation light after the two EOMs. Gray rectangles are used to guide the reader to the expected efficiency for each mode.

When we switch on the EOMs, the preparation power is shared between many spectral modes. The power in each mode, for the decided configuration of our experiment, is described in figure D.2(c). From this calibration, we can infer the expected storage efficiency and transmission through the spectral pit for the central 9 modes (dark gray region in fig. D.2), the modes ± 5 and ± 6 (gray region) and the modes ± 7 (light gray region). We note that the efficiency of the AFC seems to get visibly lower only for the modes ± 7 (fig. D.2(a)), while the spectral pit does not worsen while decreasing the power (in the range of powers analyzed).

An equivalent calibration was performed for the cases of only EOM_1 on or EOM_2 on: in the single EOM case, the central 5 modes are stored with almost flat efficiency; the modes ± 3, where the preparation power is about 10% of the central ones, are also stored, but with a much lower expected efficiency ($\sim 3.5\%$).

D.2.1 AFC efficiency (SM): comb analysis

The internal efficiency of an AFC with Gaussian peaks [68] can be calculated using the formula:

$$\eta_{AFC}^{int} = \tilde{d}^2 e^{-\frac{7}{F^2}} e^{-\tilde{d}} e^{-d_0},$$

being $\Delta = 1/\tau$ the distance between the peaks of the comb, γ their full width at half maximum, $F = \Delta/\gamma$ the finesse of the comb, $\tilde{d} = OD/F$ the effective optical depth and d_0 the absorption background. The experimental values, extracted from the measured AFC trace (inset of fig. 8.1(c) of the main text), are: $\gamma = 560$ kHz, $OD = 3.15$ and $d_0 = 0.29$, from which $F = 5.09$ and $\tilde{d} = 0.62$. Knowing that $\Delta = 1/(3.5\mu\text{s})$ we find $\eta_{AFC}^{int} = 11.8\%$. Due to the bandwidth mismatch between the photons (Lorentians with 1.8 MHz of FWHM) and the comb (about 4.2 MHz broad), the efficiency is reduced by about 76%, resulting in an expected $\eta_{AFC}^{int} = 9\%$, which agrees very well with the experimental measurement.

We can separate the AFC efficiency into three different contributions:

$$\eta_{AFC}^{int} = \eta_{abs}\eta_{reph}\eta_{loss},$$

with η_{abs} (η_{reph}) the absorption (rephasing) efficiency of the comb and η_{loss} the loss due to absorption background d_0. Knowing that $\eta_{abs} = (1 - e^{-\tilde{d}}) = 46\,\%$ (35 % if we consider the bandwidth mismatch), the rephasing efficiency of the AFC is thus $\eta_{reph} = 34\,\%$.

The achievable efficiency with the present optical depth (3.15) is about 34% for a comb with square peaks and with a finesse of about 2.4. To tailor such an AFC we would need longer preparation times, otherwise we are obliged to increase the preparation power, which degrades our AFC peaks mostly due to power broadening and instantaneous spectral diffusion. Other limitations involve the limited linewidth of our laser (about 25 kHz) and the temporal shape of the pulses that we use to tailor the AFC, which could be further optimized following [27].

D.2.2 Number of Effective Modes, N_{eM}

As the spectrum of our bi-photon is not flat, the count rate does not increase linearly with the number of stored modes. Hence, for the analysis of fig. 8.3, we define a quantity that we call *effective mode*, which is a mode whose count rate is the same as the one of the central frequency mode. If we store just the central mode, we store 1 effective mode. On the other hand, the whole spectrum of the photon (15 spectral modes) is equivalent to 5.6 effective modes.

By using different EOM configurations, we can vary the number of effective modes stored, N_{eM}. This quantity is calculated starting from the spectrum of the photon and of the preparation beam in all the EOMs configurations. Knowing these quantities, we estimate the storage efficiency or transmission through the spectral pit for each mode, using the method described in the previous subsection. For example, in fig. 8.3(a), the points, from left to right, are measured with both EOMs off ($N_{eM} = 1$), EOM_2 on ($N_{eM} = 1.8$, as we store mainly the modes with low count rate), EOM_1 on ($N_{eM} = 3.3$, bigger than EOM_2 as we store the central part of the spectrum) and both EOMs on ($N_{eM} = 5.5$, different than the case of the only source because the modes ± 7 are stored with a slightly lower efficiency), respectively.

D.3 Temporal jitter of our detection system

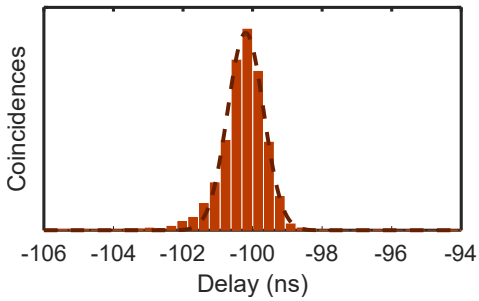

Figure D.3: Measured temporal jitter of our detection system.

As explained in [106], the width of the peaks in the beating of the second-order cross-correlation measurement gives information about the number of modes that are coherently interfering. However, in our case, the time resolution required to perform this measurement is comparable to the temporal jitter of our detection system.

To measure the time resolution of our detectors, we measure photon pairs coming directly from a SPDC process in a similar non-linear crystal. Their bandwidth corresponds to hundreds of GHz. Therefore, the time width of the measured correlation peak will correspond to the convolution of all the experimental jitters that are affecting our measurements. This measurement (brown histogram) together with its fit to a Gaussian function (black dotted line) is shown in fig. D.3. From the fit we extract a jitter of 730 ps.

D.4 Single mode and multimode comparison

In this section we check that the beating vanishes for the storage of only 1 frequency mode.

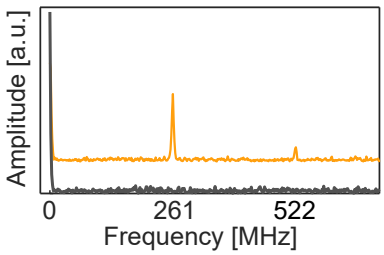

Figure D.4: Fourier transform of the correlations histogram around the AFC echo. The light orange line (shifted vertically for semplicity) corresponds to the case where we store all the spectral modes and the dark gray line to the case where we only store 1 spectral mode.

In fig. D.4 we report the Fourier transform of the coincidence histogram between the idler photon and the stored signal, around the correlations peak at 3.5 μs: in light orange, with an arbitrary vertical offset, for the case of multimode AFC preparation (MM_s), in dark gray for the storage of only 1 frequency mode (SM_s).

D.5 Spectrum analysis of the heralded photons

In this section I explain how we build the histogram of fig. 8.6(a) and (b) (and fig. D.7 of this Appendix).

To analyse the spectrum of our photon pair we use a Fabry-Perot cavity with 80 MHz of linewidth (Lorentzian) and a FSR of 17 GHz, installed in the idler optical path (FCav in fig. 8.1).

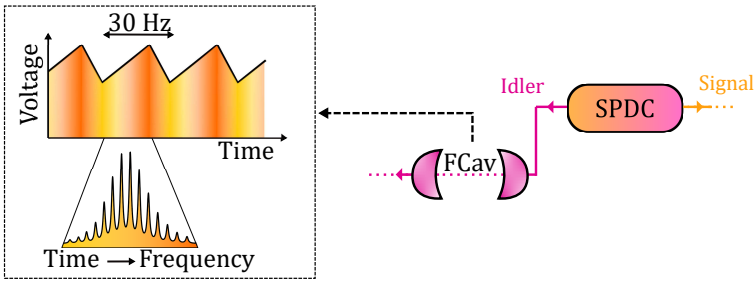

Figure D.5: Schematic of our spectrum analyser.

By scanning the FCav we are able to sweep in time the spectrum of the idler photons. In fact, at a specific time, only one specific frequency will be resonant with the cavity and thus detected. We post-select only the signal photons that are correlated with the detected idler photons. Consequently we are able to build a histogram by correlating the trigger of the scan with the heralded signal list. This histogram will correspond to the convolution between the spectrum of the photons and the spectrum of the FCav (see sec. D.7 of this Appendix).

We scan a piezoelectric element installed in one of the mirrors of the FP cavity. We send an asymmetric ramp signal generated in a function generator that we map into a voltage ranging from 0 V to 150 V. The frequency of the scan is 30 Hz. We tune the offset of the signal in order to center the spectrum of our photons to the center of the slow part of the sweep (see fig. D.5). For all the measurements performed in this work, we scanned the FCav over ~ 4 GHz, that should be enough to observe all the spectral modes of our photons.

D.6 Fit to the spectrum of the CSPDC

This section explains the fits that we used for fig. 8.6(a) and (b) and for fig. D.7 of this Appendix.

We compare the spectrum of the stored frequency multiplexed heralded single photons with the photons right after the CSPDC source. For this propose, we fit the spectrum of the photons after the CSPDC source to a

train of Lorentzian functions:

$$S = \sum_{i=1}^{14} a_i \frac{\sigma/2}{(x-b_i)^2 + (\sigma/2)^2} + d. \tag{D.1}$$

Note that, since we use a Fabry-Perot cavity that is much broader than the photons to perform this measurement, it is fair the fit to Lorentzian functions (given that the spectrum of a Fabry-Perot cavity is Lorentzian).

For comparison with the spectrum after the storage, instead of doing a new fit we just re-scaled the original fit while preserving the same relative amplitudes.

D.7 Post-processed analysis of the spectrum before and after the storage

By scanning the idler spectrum with a filter cavity, we are in resonance at different times with different spectral modes. This means that at different times our idler detections herald different modes in the signal path. We plot a coincidence histogram between the triggers and the idler detections. We then cut the idler list around each spectral mode and create one idler list for each spectral mode. In this way we want to post process a single mode idler case. Just for comparison we report in figure D.6 the spectrum of the photon (a), the simulated spectrum scanning the cavity (b), and the spectrum that we would have by locking the cavity to the central mode (c). In figure D.6(b), the background in the central mode is given only by the sum of the contribution of the other modes.

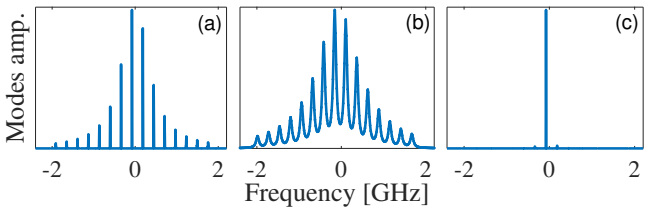

Figure D.6: (a) Frequency spectrum of the generated photons. (b)-(c) Simulated spectrum of the photons after a Fabry-Perot filter cavity (FCav) with 80 MHz of linewidth, scanned over the spectrum or locked to the central mode, respectively.

In sec. 8.7 we state that the $g^{(2)}_{s,i}$ expected in the case of a SM_i for the central mode is 15.8 ± 1.5 (see table 8.1). This is actually the measured value with the idler passing through the FC locked around the central mode. When we scan the filter cavity, an important contribution around the frequency of the central mode is given by the other spectral modes. Taking those contributions into consideration, we expect a $g^{(2)}_{s,i} = 9.8 \pm 1.1$ for the central mode in the case of just the source. This value matches with the measured value of 9.1 ± 0.5.

D.8 Different EOM combinations

We show here the spectrum of the retreived photons for all the EOMs combinations: in the main text we focus our analysis to the case where we store all the modes of the incoming spectrum (fig. 8.6(b), reported here as fig. D.7(d)) and we compared it with the single mode case (fig. 8.6(a) of the main text, reported here as D.7(a)). If we switch on just the EOM_1, that we drive with an RF signal at 261.1 MHz, we prepare the AFC for $5 \div 7$ spectral modes (for the same reason explained in section D.2) separated by 261.1 MHz (fig D.7(b)). If we just switch on the EOM_2, that we drive at 783.3 MHz, we prepare our AFCs for modes separated by 783.3 MHz (fig D.7(c)).

The results have been fitted according to the criteria introduced in the Section D.6, keeping the same parameters of the fit extracted from the brown trace and suppressing the contribution of the non-stored modes.

D.9 Scaling of $g^{(2)}_{s,i}(\Delta t)$ with the number of effective modes

From fig. 8.3(b) we see that the value of the cross correlation depends on the number of effective modes (N_{eM}). In this section we are going to explain the reason of this behaviour.

The expression for the cross correlation is: $g^{(2)}_{s,i}(\Delta t) = p_{s,i}/(p_s \cdot p_i)$. We call M the number of modes generated by our source. For the measurement of fig. 8.3(b), only a band-pass filter was used in the idler arm (>1 nm of linewidth), therefore all the spectrum of the idler photons was measured.

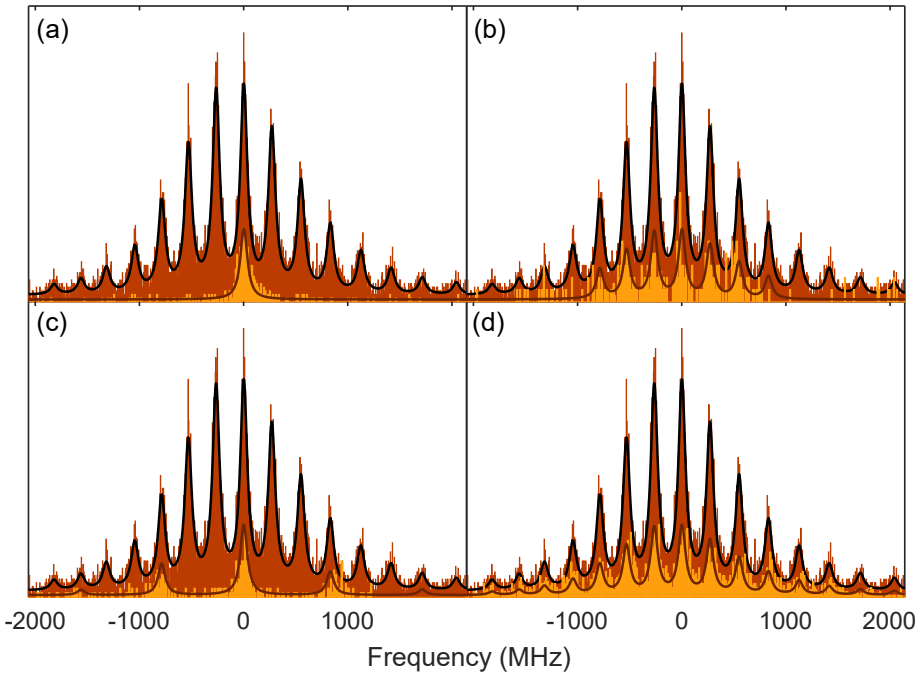

Figure D.7: Spectrum of the stored photons for different cases: (a) Both EOMs off, single mode case. (b) Just EOM_1 on. (c) Just EOM_2 on. (d) Both EOM on, fully multimode case.

N_{eM} is the number of modes addressed in the storage. We call $p_{s,i}$ the coincidence probability for the case of $N_{eM} = 1$ and $p_{s(i)}$ the probability to detect independently a signal (idler) photon in a certain time window Δt, again for $N_{eM} = 1$. We can rewrite the expression of the cross correlation as a function of N_{eM} and M as:

$$g^{(2)}_{N_{eM}s,Mi}(\Delta t) = \frac{N_{eM}p_{s,i}}{N_{eM}p_s \cdot Mp_i} = \frac{p_{s,i}}{p_s \cdot Mp_i} \tag{D.2}$$

So far, according to the previous expression, the cross correlation should not depend on N_{eM}. But we are considering the case of no dark counts in the detectors and no broadband noise. Both of them will add non correlated counts to the measurements. Since the idler detection does not depend on N_{eM}, we will consider that it is already intrinsic to the

expression Mp_i. We can introduce the noise in the signal arm as:

$$g^{(2)}_{\mathrm{N}_{eM}s,Mi}(\Delta t) = \frac{\mathrm{N}_{eM}p_{s,i}}{(\mathrm{N}_{eM}p_s + B)\cdot Mp_i}, \tag{D.3}$$

where B represents the probability of both detecting dark counts or broadband non-correlated noise. If B is comparable with p_s, the effect of this term will only affect our measurements for small values of N_{eM}. While our N_{eM} increases we see an asymptotic trend towards the value of eq. D.2.

Appendix E

Multimodality in our system

- **Temporal multimodality**

The AFC storage time τ is ultimately limited by the coherence time of the optical transition. Assuming an AFC echo decay consistent with the maximally measured coherence time in Pr^{3+}:Y_2SiO_5, $T_2 = 111\,\mu s$ [126], the storage efficiency would decay as a function of τ as in fig. E.1(a) [27].

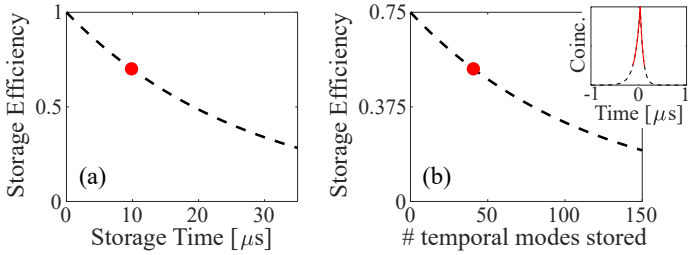

Figure E.1: (a) AFC maximal storage efficiency in the excited state vs storage time τ. The decay assumes an AFC effective coherence time equal to $111\mu s$. The considered storage time of $10\,\mu s$ is highlighted with a red point. (b) As in panel (a), with the number of temporal modes in the x-axis. In the inset the shape of the considered photons (sec. 4.3.2), with, in red, the chosen temporal window for each temporal mode.

The heralded photons generated by our photon pair source (sec. 4.3.2) are reported in the inset of fig. E.1(b). The coherence time of the photon is about $\tau_c = 120\,ns$. In terms of rate we would like to consider a big window of interest, Δt, around the peak of the photon, in order not to loose counts. On the other hand, the bigger the window considered, the less the number of modes stored, namely $N=\tau/\Delta t$. In the inset we consider a window $\Delta t= 2\tau_c = 240\,ns$ (red solid line). As a consequence, I report in (b) the same plot as in panel (a), but with the number of temporal modes in the

x-axis and with a maximal efficiency limited by the considered temporal window Δt.

• Spectral multimodality

In the inhomogeneous broadening we can create a single class AFC each $\sim$ 80 MHz. I report in fig. E.2(a) the OD along the inhomogeneously broadened absorption profile of the ions, being a Gaussian of about 9 GHz (as measured in Chapter 7). The maximum OD considered (10) is the expected OD for a 5 mm sample like ours, calculated as OD=αL, where α is the absorption coefficient (23/cm[119]) and L is the length of the crystal. For a fixed OD, the maximum AFC efficiency that we can get is defined by the formula $\eta_{AFC} = \tilde{d}^2\, e^{-\tilde{d}}\, \mathrm{sinc}^2(\pi/\mathrm{F})\, e^{-d_0}$, where F is the finesse of the peaks of the comb and $\tilde{d}$ =OD/F and considering a square comb with a null backgroud OD, $d_0 = 0$ [68]. I plot the maximum efficiency achievable along the inhomogeneous broadening of panel (a) in panel (b) versus the number of frequency modes, considering 1 mode each 80 MHz [31]. With the photon-pair source that we have in our lab, we would need a bow-tie cavity as long as 3.75 m in order to have such a FSR. The dotted line in panel (b) is the achievable efficiency in case of $d_0 = 0.25$, the usually measured d_0 in our lab.

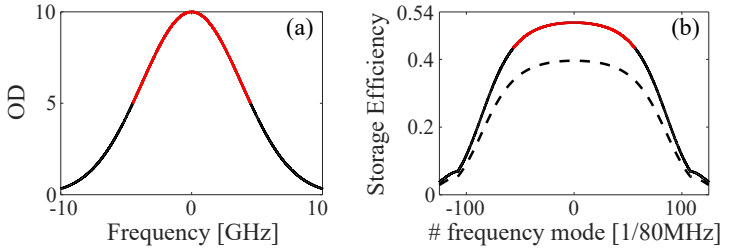

Figure E.2: (a) Inhomogeneously broadened absorption profile (Gaussian, 9 GHz in FWHM) in OD. (b) Maximal AFC storage efficiency in the excited state vs frequency modes (the dotted line is calculated for $d_0 = 0.25$). The x-axis is the same as in panel (a), divided by 80 MHz (minimum spacing between single-class AFCs [31]). In both panels, the spectral bandwidth considered within the inhomogeneous broadening of the memory is highlighted in red.

It can be noticed that, within the FWHM of the inhomogeneous broadening (in red in fig. E.2), the efficiency per spectral mode is almost flat (the average efficiency along the red line being 49%). Note that the AFC protocol is limited to 54% efficiency for storage in the excited state [68],

and it can be higher in the case of backretrieval of the stored light (for example with SW storage).

For both temporal and frequency multiplexing, the bigger the number of modes we want to store, the lower is the total storage efficiency. In a real scenario we will have to find a threshold between the number of stored modes and the efficiency. In fig. E.3 I put together the analysis done in figs. E.1 and E.2. The efficiency considered for the frequency modes is the average efficiency (each mode will have a slightly different efficiency, see fig. E.2(b)).

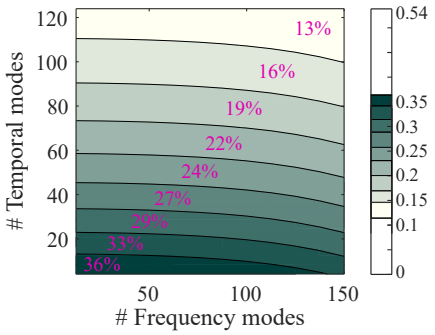

Figure E.3: AFC storage efficiency vs number of temporal (vertical axis) and frequency (horizontal) modes stored. The plot puts together the analysis of fig. E.1(b) and E.2(b).

• Spatial multimodality

I want to consider the spatial multimodality on its own. With memories integrated in fiber-pigtailed waveguides the spatial multimodality scales as 62 modes per mm^2 of crystal surface (see fig. E.4). This is because the standard distance of commercial fiber arrays is 127 μm. For spatial multiplexing the storage efficiency does not change with the number of modes, differently from the other two cases.

In the case of emissive quantum memories [2, 29, 30], in which the QM itself generates the photon correlated with a stored state, spatial multiplexing would be an ideal solution. In case of absorptive QM, to use it in our QR link scenario (see sec. 1.2.2), we would need to couple each waveguide with a different photon-pair source, making this solution less scalable. However, even in our proposal, spatial multiplexing can be very useful to reduce drastically the problem of the duty cycle of the memory. In fact each

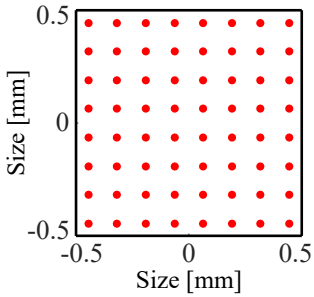

Figure E.4: Spatial modes (red dots) in case of a standard matrix of fiber-pigtailed waveguides.

cycle of the cryostat we need a few hundreds of ms to prepare the memory (~ 400 ms, usually). The storage is performed during the following ~ 100 to 200 ms. Moreover, as described in Chapter 5, each time that we perform SW storage, we cannot perform any other storage trial until we do not retrieve the stored quantum state. In this view, each time that a memory is not available for storage, we could use another spatial mode, approaching our duty-cycle to 1. Other important applications that we can imagine is the generation of cluster states or multiphoton states.

• Possible number of stored modes

We consider for the temporal modes the storage time highlighted in red in fig. E.1, namely 10 μs. With this we can store about 41 temporal modes with 50% of the total achievable efficiency. The frequency modes that we can store within the FWHM of the inhomogeneous broadening (red in fig. E.2) are about 113, with an average storage efficiency of 49% (38% in case of $d_0 = 0.25$). Adding 62 spatial modes per mm^2 of crystal surface, we can store a total of $41 \cdot 113 \cdot 62/\text{mm}^2 \sim 290\,000$ modes/mm^2, with a maximum storage efficiency of $\sim 25\%$, for storage in the excited state. With a CSPDC as long as ours (261 MHz in FSR), the number of modes that we could store would decrease to about $90\,000/\text{mm}^2$.

If we want to store polarization qubits, or add 2 polarization modes ([41, 42, 44]) we would need two waveguides for each polarization as our waveguides are polarization sensitive. In laser written waveguides, moreover, orbital angular momentum states have been coupled (only 3 until now [204]). In the future, maybe, this degree of freedom could be added to our system, further increasing the multiplexing capabilities.

Bibliography

[1] N. Gisin and R. Thew: *Quantum communication*, Nature photonics **1**, 165 (2007). 3

[2] L.-M. Duan, M. D. Lukin, J. I. Cirac, and P. Zoller: *Long-distance quantum communication with atomic ensembles and linear optics*, Nature **414**, 413 (2001). 3, 5, 8, 12, 13, 14, 151

[3] K. Azuma, K. Tamaki, and H.-K. Lo: *All-photonic quantum repeaters*, Nature communications **6**, 6787 (2015). 3, 5, 12

[4] J. Yin, Y. Cao, Y.-H. Li, S.-K. Liao, et al.: *Satellite-based entanglement distribution over 1200 kilometers*, Science **356**, 1140 (2017). 3, 12

[5] P. C. Humphreys, N. Kalb, J. P. Morits, R. N. Schouten, et al.: *Deterministic delivery of remote entanglement on a quantum network*, Nature **558**, 268 (2018). 3, 12, 15

[6] V. Krutyanskiy, M. Meraner, J. Schupp, V. Krcmarsky, et al.: *Light-matter entanglement over 50 km of optical fibre*, arXiv preprint arXiv:1901.06317 (2019). 3, 12, 15

[7] Http://quantum-internet.team/. 3

[8] Https://qt.eu/. 3

[9] H. J. Kimble: *The quantum internet*, Nature **453**, 1023 (2008). 3

[10] J. Yin, Y. Cao, Y.-H. Li, J.-G. Ren, et al.: *Satellite-to-Ground Entanglement-Based Quantum Key Distribution*, Phys. Rev. Lett. **119**, 200501 (2017). 3

[11] S.-K. Liao, W.-Q. Cai, J. Handsteiner, B. Liu, et al.: *Satellite-Relayed Intercontinental Quantum Network*, Phys. Rev. Lett. **120**, 030501 (2018). 3

[12] T. Inagaki, N. Matsuda, O. Tadanaga, M. Asobe, et al.: *Entanglement distribution over 300 km of fiber*, Optics express **21**, 23241 (2013). 3

[13] M. Zukowski, A. Zeilinger, M. A. Horne, and A. K. Ekert: *"Event-ready-detectors" Bell experiment via entanglement swapping*, Phys. Rev. Lett. **71**, 4287 (1993). 4

[14] Y. Hasegawa, R. Ikuta, N. Matsuda, K. Tamaki, et al.: *Experimental time-reversed adaptive Bell measurement towards all-photonic quantum repeaters*, Nature communications **10**, 378 (2019). 5, 12

[15] N. Sangouard, C. Simon, H. de Riedmatten, and N. Gisin: *Quantum repeaters based on atomic ensembles and linear optics*, Rev. Mod. Phys. **83**, 33 (2011). 6, 12, 13, 14, 70, 104

[16] M. Afzelius, N. Gisin, and H. de Riedmatten: *Quantum memory for photons*, Physics Today **68**, 42 (2015). 6, 54

[17] F. Bussières, N. Sangouard, M. Afzelius, H. de Riedmatten, et al.: *Prospective applications of optical quantum memories*, Journal of Modern Optics **60**, 1519 (2013). 6, 7, 70

[18] N. Sinclair, E. Saglamyurek, H. Mallahzadeh, J. A. Slater, et al.: *Spectral Multiplexing for Scalable Quantum Photonics using an Atomic Frequency Comb Quantum Memory and Feed-Forward Control*, Phys. Rev. Lett. **113**, 053603 (2014). 6, 7, 10, 104

[19] C. Simon, H. de Riedmatten, M. Afzelius, N. Sangouard, et al.: *Quantum Repeaters with Photon Pair Sources and Multimode Memories*, Phys. Rev. Lett. **98**, 190503 (2007). 6, 12, 13, 54, 64, 68, 104

[20] I. Usmani, M. Afzelius, H. de Riedmatten, and N. Gisin: *Mapping multiple photonic qubits into and out of one solid-state atomic ensemble*, Nat Commun **1**, 12 (2010). 7, 10, 104

[21] M. Bonarota, J.-L. L. Gouët, and T. Chanelière: *Highly multimode storage in a crystal*, New Journal of Physics **13**, 013013 (2011). 7, 10, 104

[22] C. Clausen, I. Usmani, F. Bussieres, N. Sangouard, et al.: *Quantum storage of photonic entanglement in a crystal*, Nature **469**, 508 (2011). 7, 9, 15, 54, 104

[23] E. Saglamyurek, N. Sinclair, J. Jin, J. A. Slater, et al.: *Broadband waveguide quantum memory for entangled photons*, Nature **469**, 512 (2011). 7, 9, 11, 15, 54, 70, 83, 97, 104

[24] M. Gündoğan, P. M. Ledingham, K. Kutluer, M. Mazzera, et al.: *Solid State Spin-Wave Quantum Memory for Time-Bin Qubits*, Phys. Rev. Lett. **114**, 230501 (2015). 7, 9, 11, 16, 49, 54, 56, 67, 68, 77, 78, 99, 104, 117, 126

[25] J.-S. Tang, Z.-Q. Zhou, Y.-T. Wang, Y.-L. Li, et al.: *Storage of multiple single-photon pulses emitted from a quantum dot in a solid-state quantum memory*, Nature communications **6**, 8652 (2015). 7

[26] A. Tiranov, P. C. Strassmann, J. Lavoie, N. Brunner, et al.: *Temporal multimode storage of entangled photon pairs*, Physical review letters **117**, 240506 (2016). 7, 104

[27] P. Jobez, N. Timoney, C. Laplane, J. Etesse, et al.: *Towards highly multimode optical quantum memory for quantum repeaters*, Phys. Rev. A **93**, 032327 (2016). 7, 10, 51, 76, 96, 104, 140, 149

[28] A. Seri, A. Lenhard, D. Rieländer, M. Gündoğan, et al.: *Quantum Correlations between Single Telecom Photons and a Multimode On-Demand Solid-State Quantum Memory*, Phys. Rev. X **7**, 021028 (2017). 7, 8, 9, 12, 15, 20, 42, 54, 84, 85, 104, 115, 117, 131

[29] K. Kutluer, M. Mazzera, and H. de Riedmatten: *Solid-state source of nonclassical photon pairs with embedded multimode quantum memory*, Physical review letters **118**, 210502 (2017). 7, 8, 16, 104, 120, 151

[30] C. Laplane, P. Jobez, J. Etesse, N. Gisin, et al.: *Multimode and long-lived quantum correlations between photons and spins in a crystal*, Physical review letters **118**, 210501 (2017). 7, 8, 16, 104, 120, 151

[31] T.-S. Yang, Z.-Q. Zhou, Y.-L. Hua, X. Liu, et al.: *Multiplexed storage and real-time manipulation based on a multiple degree-of-freedom quantum memory*, Nature communications **9**, 3407 (2018). 7, 104, 150

[32] S.-Y. Lan, A. G. Radnaev, O. A. Collins, D. N. Matsukevich, et al.: *A multiplexed quantum memory*, Opt. Express **17**, 13639 (2009). 7, 104

[33] Y. Pu, N. Jiang, W. Chang, H. Yang, et al.: *Experimental realization of a multiplexed quantum memory with 225 individually accessible memory cells*, Nature communications **8**, 15359 (2017). 7, 10, 104

[34] R. Chrapkiewicz, M. Dąbrowski, and W. Wasilewski: *High-capacity angularly multiplexed holographic memory operating at the single-photon level*, Physical review letters **118**, 063603 (2017). 7, 10, 104

[35] L. Tian, Z. Xu, L. Chen, W. Ge, et al.: *Spatial Multiplexing of Atom-Photon Entanglement Sources using Feedforward Control and Switching Networks*, Physical review letters **119**, 130505 (2017). 7, 104

[36] A. Nicolas, L. Veissier, L. Giner, E. Giacobino, et al.: *A quantum memory for orbital angular momentum photonic qubits*, Nat Photon **8**, 234 (2014). 7, 104

[37] D.-S. Ding, W. Zhang, Z.-Y. Zhou, S. Shi, et al.: *Quantum Storage of Orbital Angular Momentum Entanglement in an Atomic Ensemble*, Phys. Rev. Lett. **114**, 050502 (2015). 7, 104

[38] Z.-Q. Zhou, Y.-L. Hua, X. Liu, G. Chen, et al.: *Quantum storage of three-dimensional orbital-angular-momentum entanglement in a crystal*, Physical review letters **115**, 070502 (2015). 7, 10, 15

[39] E. Saglamyurek, M. G. Puigibert, Q. Zhou, L. Giner, et al.: *A multiplexed light-matter interface for fibre-based quantum networks*, Nature communications **7**, 11202 (2016). 7, 10, 11, 12, 54, 70, 104

[40] A. Seri, D. Lago-Rivera, A. Lenhard, G. Corrielli, et al.: *Quantum Storage of Frequency-Multiplexed Heralded Single Photons*, arXiv:1902.06657 (2019). 7, 20, 103, 118

[41] M. Gündoğan, P. M. Ledingham, A. Almasi, M. Cristiani, et al.: *Quantum Storage of a Photonic Polarization Qubit in a Solid*, Phys. Rev. Lett. **108**, 190504 (2012). 7, 16, 152

[42] C. Clausen, F. Bussières, M. Afzelius, and N. Gisin: *Quantum Storage of Heralded Polarization Qubits in Birefringent and Anisotropically Absorbing Materials*, Phys. Rev. Lett. **108**, 190503 (2012). 7, 152

[43] Z.-Q. Zhou, W.-B. Lin, M. Yang, C.-F. Li, et al.: *Realization of reliable solid-state quantum memory for photonic polarization qubit*, Phys. Rev. Lett. **108**, 190505 (2012). 7

[44] C. Laplane, P. Jobez, J. Etesse, N. Timoney, et al.: *Multiplexed on-demand storage of polarization qubits in a crystal*, New Journal of Physics **18**, 013006 (2016). 7, 54, 152

[45] S. Massar and S. Popescu: *Optimal Extraction of Information from Finite Quantum Ensembles*, Phys. Rev. Lett. **74**, 1259 (1995). 7

[46] A. Orieux and E. Diamanti: *Recent advances on integrated quantum communications*, Journal of Optics **18**, 083002 (2016). 7

[47] J. Dajczgewand, J.-L. Le Gouët, A. Louchet-Chauvet, and T. Chanelière: *Large efficiency at telecom wavelength for optical quantum memories*, Optics letters **39**, 2711 (2014). 7, 8

[48] P. Farrera, N. Maring, B. Albrecht, G. Heinze, et al.: *Nonclassical correlations between a C-band telecom photon and a stored spin-wave*, Optica **3**, 1019 (2016). 7, 12, 15, 54

[49] H. P. Specht, C. Nolleke, A. Reiserer, M. Uphoff, et al.: *A single-atom quantum memory*, Nature **473**, 190 (2011). 8

[50] S.-P. Yu, J. D. Hood, J. A. Muniz, M. J. Martin, et al.: *Nanowire photonic crystal waveguides for single-atom trapping and strong light-matter interactions*, Applied Physics Letters **104** (2014). 8

[51] B. Julsgaard, J. Sherson, J. I. Cirac, J. Fiurášek, et al.: *Experimental demonstration of quantum memory for light*, Nature **432**, 482 (2004). 8

[52] T. Chanelière, D. N. Matsukevich, S. D. Jenkins, S.-Y. Lan, et al.: *Storage and retrieval of single photons transmitted between remote quantum memories*, Nature **438**, 833 (2005). 8

[53] M. D. Eisaman, A. André, F. Massou, M. Fleischhauer, et al.: *Electromagnetically induced transparency with tunable single-photon pulses*, Nature **438**, 837 (2005). 8

[54] E. Togan, Y. Chu, A. S. Trifonov, L. Jiang, et al.: *Quantum entanglement between an optical photon and a solid-state spin qubit*, Nature **466**, 730 (2010). 8

[55] H. Bernien, B. Hensen, W. Pfaff, G. Koolstra, et al.: *Heralded entanglement between solid-state qubits separated by three metres*, Nature **497**, 86 (2013). 8

[56] D. G. England, K. A. G. Fisher, J.-P. W. MacLean, P. J. Bustard, et al.: *Storage and Retrieval of THz-Bandwidth Single Photons Using a Room-Temperature Diamond Quantum Memory*, Phys. Rev. Lett. **114**, 053602 (2015). 8

[57] K. De Greve, L. Yu, P. L. McMahon, J. S. Pelc, et al.: *Quantum-dot spin-photon entanglement via frequency downconversion to telecom wavelength*, Nature **491**, 421 (2012). 8, 54

[58] X.-H. Bao, A. Reingruber, P. Dietrich, J. Rui, et al.: *Efficient and long-lived quantum memory with cold atoms inside a ring cavity*, Nat Phys **8**, 517 (2012). 8

[59] K. R. Ferguson, S. E. Beavan, J. J. Longdell, and M. J. Sellars: *Generation of light with multimode time-delayed entanglement using storage in a solid-state spin-wave quantum memory*, Physical review letters **117**, 020501 (2016). 8, 15, 54, 65

[60] S. E. Harris: *Electromagnetically induced transparency*, in *Quantum Electronics and Laser Science Conference*, QTuB1, Optical Society of America (1997). 8

[61] M. Fleischhauer, A. Imamoglu, and J. P. Marangos: *Electromagnetically induced transparency: Optics in coherent media*, Rev. Mod. Phys. **77**, 633 (2005). 8

[62] J. Nunn, I. A. Walmsley, M. G. Raymer, K. Surmacz, et al.: *Mapping broadband single-photon wave packets into an atomic memory*, Phys. Rev. A **75**, 11401 (2007). 8

[63] K. Kutluer, M. F. Pascual-Winter, J. Dajczgewand, P. M. Ledingham, et al.: *Spectral-hole memory for light at the single-photon level*, Phys. Rev. A **93**, 040302 (2016). 8, 9

[64] M. Hosseini, B. M. Sparkes, G. Hetet, J. J. Longdell, et al.: *Coherent optical pulse sequencer for quantum applications*, Nature **461**, 241 (2009). 8

[65] M. P. Hedges, J. J. Longdell, Y. Li, and M. J. Sellars: *Efficient quantum memory for light*, Nature **465**, 1052 (2010). 8, 9, 65, 68, 117

[66] V. Damon, M. Bonarota, A. Louchet-Chauvet, T. Chaneliere, et al.: *Revival of silenced echo and quantum memory for light*, New Journal of Physics **13**, 093031 (2011). 8

[67] D. McAuslan, P. M. Ledingham, W. R. Naylor, S. Beavan, et al.: *Photon-echo quantum memories in inhomogeneously broadened two-level atoms*, Physical Review A **84**, 022309 (2011). 8

[68] M. Afzelius, C. Simon, H. de Riedmatten, and N. Gisin: *Multimode quantum memory based on atomic frequency combs*, Phys. Rev. A **79**, 52329 (2009). 8, 10, 13, 32, 39, 40, 41, 42, 54, 64, 75, 76, 107, 125, 140, 150

[69] Y.-F. Hsiao, P.-J. Tsai, H.-S. Chen, S.-X. Lin, et al.: *Highly Efficient Coherent Optical Memory Based on Electromagnetically Induced Transparency*, Phys. Rev. Lett. **120**, 183602 (2018). 9

[70] Y. Wang, J. Li, S. Zhang, K. Su, et al.: *Efficient quantum memory for single-photon polarization qubits*, Nature Photonics (2019). 9

[71] Y. O. Dudin, L. Li, and A. Kuzmich: *Light storage on the time scale of a minute*, Phys. Rev. A **87**, 031801 (2013). 9

[72] G. Heinze, C. Hubrich, and T. Halfmann: *Stopped Light and Image Storage by Electromagnetically Induced Transparency up to the*

Regime of One Minute, Phys. Rev. Lett. **111**, 033601 (2013). 9, 15, 41, 68, 117

[73] Y.-W. Cho, G. T. Campbell, J. L. Everett, J. Bernu, et al.: *Highly efficient optical quantum memory with long coherence time in cold atoms*, Optica **3**, 100 (2016). 9

[74] M. Hosseini, B. M. Sparkes, G. Campbell, P. K. Lam, et al.: *High efficiency coherent optical memory with warm rubidium vapour*, Nat Commun **2**, 174 (2011). 9

[75] H. de Riedmatten, M. Afzelius, M. U. Staudt, C. Simon, et al.: *A solid-state light-matter interface at the single-photon level*, Nature **456**, 773 (2008). 9

[76] M. Sabooni, Q. Li, S. Kröll S., and L. Rippe: *Efficient Quantum Memory Using a Weakly Absorbing Sample*, Phys. Rev. Lett. **110**, 133604 (2013). 10, 68

[77] M. Afzelius and C. Simon: *Impedance-matched cavity quantum memory*, Phys. Rev. A **82**, 22310 (2010). 10, 119

[78] J. Nunn, K. Reim, K. C. Lee, V. O. Lorenz, et al.: *Multimode Memories in Atomic Ensembles*, Phys. Rev. Lett. **101**, 260502 (2008). 10

[79] D. England, P. Michelberger, T. Champion, K. Reim, et al.: *High-fidelity polarization storage in a gigahertz bandwidth quantum memory*, Journal of Physics B: Atomic, Molecular and Optical Physics **45**, 124008 (2012). 10

[80] M. U. Staudt, M. Afzelius, H. de Riedmatten, S. R. Hastings-Simon, et al.: *Interference of multimode photon echoes generated in spatially separated solid-state atomic ensembles*, Phys. Rev. Lett. **99**, 173602 (2007). 11, 70

[81] M. U. Staudt, S. R. Hastings-Simon, M. Nilsson, M. Afzelius, et al.: *Fidelity of an Optical Memory Based on Stimulated Photon Echoes*, Phys. Rev. Lett. **98**, 113601 (2007). 11, 70

[82] E. Saglamyurek, N. Sinclair, J. A. Slater, K. Heshami, et al.: *An integrated processor for photonic quantum states using a broadband*

light–matter interface, New Journal of Physics **16**, 065019 (2014). 11, 70, 77

[83] M. F. Askarani, M. Pugibert, T. Lutz, V. B. Verma, et al.: *Storage and retrieval of heralded telecommunication-wavelength photons using a solid-state waveguide quantum memory*, arXiv preprint arXiv:1804.05699 (2018). 11, 83, 97

[84] L. Veissier, M. Falamarzi, T. Lutz, E. Saglamyurek, et al.: *Optical decoherence and spectral diffusion in an erbium-doped silica glass fiber featuring long-lived spin sublevels*, Physical Review B **94**, 195138 (2016). 11, 26, 70

[85] N. Sinclair, D. Oblak, C. W. Thiel, R. L. Cone, et al.: *Properties of a rare-earth-ion-doped waveguide at sub-kelvin temperatures for quantum signal processing*, Physical review letters **118**, 100504 (2017). 11, 70

[86] T. Zhong, J. M. Kindem, E. Miyazono, and A. Faraon: *Nanophotonic coherent light-matter interfaces based on rare-earth-doped crystals*, Nat Commun **6**, (2015). 11, 70

[87] T. Zhong, J. M. Kindem, J. G. Bartholomew, J. Rochman, et al.: *Nanophotonic rare-earth quantum memory with optically controlled retrieval*, Science **357**, 1392 (2017). 11, 70

[88] M. Afzelius, I. Usmani, A. Amari, B. Lauritzen, et al.: *Demonstration of Atomic Frequency Comb Memory for Light with Spin-Wave Storage*, Phys. Rev. Lett. **104**, 040503 (2010). 11, 41, 42, 77, 115, 126

[89] M. Gündogan, M. Mazzera, P. M. Ledingham, M. Cristiani, et al.: *Coherent storage of temporally multimode light using a spin-wave atomic frequency comb memory*, New Journal of Physics **15**, 45012 (2013). 11, 77, 126

[90] P. Jobez, N. Timoney, C. Laplane, J. Etesse, et al.: *Towards highly multimode optical quantum memory for quantum repeaters*, ArXiv: 1512.02936 10 (2015). 11, 54, 68, 78

[91] S. Marzban, J. G. Bartholomew, S. Madden, K. Vu, et al.: *Observation of Photon Echoes From Evanescently Coupled Rare-Earth Ions in a Planar Waveguide*, Phys. Rev. Lett. **115**, 013601 (2015). 12, 70

[92] G. Corrielli, A. Seri, M. Mazzera, R. Osellame, et al.: *An Integrated Optical Memory based on Laser Written Waveguides*, ArXiv: 1512.09288 (2015). 12, 20

[93] C. Simon: *Towards a global quantum network*, Nature Photonics **11**, 678 (2017). 12

[94] P. R. Tapster and J. G. Rarity: *Photon statistics of pulsed parametric light*, Journal of Modern Optics **45**, 595 (1998). 13, 18, 62

[95] C. W. Chou, H. de Riedmatten, D. Felinto, S. V. Polyakov, et al.: *Measurement-induced entanglement for excitation stored in remote atomic ensembles*, Nature **438**, 828 (2005). 14

[96] C. W. Chou, J. Laurat, H. Deng, K. S. Choi, et al.: *Functional Quantum Nodes for Entanglement Distribution over Scalable Quantum Networks*, Science **316**, 1316 (2007). 14

[97] H.-J. Briegel, W. Dür, J. I. Cirac, and P. Zoller: *Quantum Repeaters: The Role of Imperfect Local Operations in Quantum Communication*, Phys. Rev. Lett. **81**, 5932 (1998). 14

[98] Z.-S. Yuan, Y.-A. Chen, B. Zhao, S. Chen, et al.: *Experimental demonstration of a BDCZ quantum repeater node*, Nature **454**, 1098 (2008). 14

[99] B. Hensen, H. Bernien, A. E. Dréau, A. Reiserer, et al.: *Loophole-free Bell inequality violation using electron spins separated by 1.3 kilometres*, Nature **526**, 682 (2015). 15

[100] A. Dréau, A. Tchebotareva, A. E. Mahdaoui, C. Bonato, et al.: *Quantum Frequency Conversion of Single Photons from a Nitrogen-Vacancy Center in Diamond to Telecommunication Wavelengths*, Phys. Rev. Applied **9**, 064031 (2018). 15

[101] B. Albrecht, P. Farrera, X. Fernandez-Gonzalvo, M. Cristiani, et al.: *A waveguide frequency converter connecting rubidium-based quantum memories to the telecom C-band*, Nat Commun **5**, (2014). 15, 54

[102] Y. Yu, F. Ma, X.-Y. Luo, B. Jing, et al.: *Entanglement of two quantum memories via metropolitan-scale fibers*, arXiv preprint arXiv:1903.11284 (2019). 15

[103] I. Usmani, C. Clausen, F. Bussieres, N. Sangouard, et al.: *Heralded quantum entanglement between two crystals*, Nat Photon **6**, 234 (2012). 15

[104] F. Bussières, C. Clausen, A. Tiranov, B. Korzh, et al.: *Quantum teleportation from a telecom-wavelength photon to a solid-state quantum memory*, Nat Photon **8**, 775 (2014). 15

[105] K. Kutluer, E. Distante, B. Casabone, S. Duranti, et al.: *Time Entanglement between a Photon and a Spin Wave in a Multimode Solid-state Quantum Memory*, arXiv preprint arXiv:1904.02537 (2019). 16

[106] J. Fekete, D. Rielander, M. Cristiani, and H. de Riedmatten: *Ultranarrow-Band Photon-Pair Source Compatible with Solid State Quantum Memories and Telecommunication Networks*, Phys. Rev. Lett. **110**, 220502 (2013). 16, 46, 47, 55, 56, 110, 141

[107] D. Rieländer, K. Kutluer, P. M. Ledingham, M. Gündoğan, et al.: *Quantum Storage of Heralded Single Photons in a Praseodymium-Doped Crystal*, Phys. Rev. Lett. **112**, 040504 (2014). 16, 43, 54, 56, 59, 76, 94, 97

[108] M. Fox: *Quantum optics: an introduction*, vol. 15, OUP Oxford (2006). 16, 18

[109] H. Riedmatten and M. Afzelius: *Engineering the Atom-Photon Interaction: Controlling Fundamental Processes with Photons, Atoms and Solids*, chap. Quantum Light Storage in Solid State Atomic Ensembles, 241–273, Springer International Publishing, Cham (2015). 16, 42

[110] A. Kuzmich, W. P. Bowen, A. D. Boozer, A. Boca, et al.: *Generation of nonclassical photon pairs for scalable quantum communication with atomic ensembles*, Nature **423**, 731 (2003). 17, 18, 19

[111] P. Sekatski, N. Sangouard, F. Bussières, C. Clausen, et al.: *Detector imperfections in photon-pair source characterization*, Journal of

Physics B: Atomic, Molecular and Optical Physics **45**, 124016 (2012). 17

[112] R. H. Brown and R. Twiss: *A test of a new type of stellar interferometer on Sirius*, Nature **178**, 1046 (1956). 18

[113] R. Loudon: *The quantum theory of light*, OUP Oxford (2000). 18, 19

[114] A. Christ, K. Laiho, A. Eckstein, K. N. Cassemiro, et al.: *Probing multimode squeezing with correlation functions*, New Journal of Physics **13**, 033027 (2011). 18, 107

[115] F. Chen and J. R. Aldana: *Optical waveguides in crystalline dielectric materials produced by femtosecond-laser micromachining*, Laser & Photonics Reviews **8**, 251 (2014). 20, 71

[116] A. Seri, G. Corrielli, D. Lago-Rivera, A. Lenhard, et al.: *Laser-written integrated platform for quantum storage of heralded single photons*, Optica **5**, 934 (2018). 20, 78, 82, 104, 118

[117] M. Mazzera: *Fourier transform spectroscopy of Rare Earths in insulating materials for photonics*, Ph.D. thesis (2006). 21, 23, 24

[118] R. Capelletti, A. Baraldi, E. Buffagni, N. Magnani, et al.: *Rare earths as a probe of environment and electron-phonon interaction in optical materials: high resolution absorption spectroscopy and theoretical analysis Rare earths: Research and Applications*, Nova Science Publishers, Inc.: New York (2008). 21

[119] M. Gündoğan: *Solid-state quantum memory for photonic qubits*, Ph.D. thesis (2015). 21, 35, 36, 42, 56, 90, 91, 150

[120] S. Cotton: *Lanthanide and actinide chemistry*, John Wiley & Sons (2013). 21

[121] A. J. Freeman and R. Watson: *Theoretical investigation of some magnetic and spectroscopic properties of rare-earth ions*, Physical Review **127**, 2058 (1962). 22

[122] G. Miessler, P. Fischer, and D. Tarr: *Inorganic Chemistry*, Pearson advanced chemistry series, Pearson (2014). 23

[123] *https://www.webelements.com/praseodymium/isotopes.html*. 24

[124] C. Li, C. Wyon, and R. Moncorge: *Spectroscopic properties and fluorescence dynamics of Er^{3+} and Yb^{3+} in Y_2SiO_5*, IEEE journal of quantum electronics **28**, 1209 (1992). 24

[125] L. Allen and J. Eberly: *Optical Resonance and Two-level Atoms*, Dover books on physics and chemistry, Dover (1987). 25, 32

[126] R. W. Equall, R. L. Cone, and R. M. Macfarlane: *Homogeneous broadening and hyperfine structure of optical transitions in Pr^{3+}:Y_2SiO_5*, Phys. Rev. B **52**, 3963 (1995). 25, 34, 35, 41, 149

[127] E. Fraval, M. J. Sellars, and J. J. Longdell: *Method of Extending Hyperfine Coherence Times in Pr^{3+}:Y_2SiO_5*, Phys. Rev. Lett. **92**, 77601 (2004). 26, 41

[128] E. Fraval, M. J. Sellars, and J. J. Longdell: *Dynamic Decoherence Control of a Solid-State Nuclear-Quadrupole Qubit*, Phys. Rev. Lett. **95**, 30506 (2005). 26, 42

[129] C. Foot: *Atomic physics*, Oxford master series in physics, Oxford University Press (2005). 27, 30, 31

[130] R. R. Reibel: *High bandwidth optical coherent transient true-time delay* (2002). 27, 31

[131] L. Rippe: *Quantum computing with naturally trapped sub-nanometre-spaced ions*, Ph.D. thesis (2006). 27, 31, 32

[132] N. Sangouard, C. Simon, M. Afzelius, and N. Gisin: *Analysis of a quantum memory for photons based on controlled reversible inhomogeneous broadening*, Phys. Rev. A **75**, 32327 (2007). 32, 34

[133] Y. Sun, G. M. Wang, R. L. Cone, R. W. Equall, et al.: *Symmetry considerations regarding light propagation and light polarization for coherent interactions with ions in crystals*, Phys. Rev. B **62**, 15443 (2000). 32, 33

[134] A. V. Durrant, J. Manners, and P. M. Clark: *Understanding optical echoes using Schrodiner's equation: I. Echoes excited by two optical pulses*, Eur. J. Phys. **10**, 291 (1989). 34, 88

[135] M. Nilsson, L. Rippe, S. Kröll, R. Klieber, et al.: *Hole-burning techniques for isolation and study of individual hyperfine transitions in inhomogeneously broadened solids demonstrated in $Pr^{3+}:Y_2SiO_5$* , Phys. Rev. B **70**, 214111 (2004). 35, 88, 133, 134

[136] J. Nunn, K. Reim, K. C. Lee, V. O. Lorenz, et al.: *Multimode Memories in Atomic Ensembles*, Phys. Rev. Lett. **101**, 260502 (2008). 41

[137] G. Corrielli, A. Seri, M. Mazzera, R. Osellame, et al.: *Integrated Optical Memory Based on Laser-Written Waveguides*, Phys. Rev. Applied **5**, 054013 (2016). 42, 67, 69, 118

[138] L. Viola and S. Lloyd: *Dynamical suppression of decoherence in two-state quantum systems*, Phys. Rev. A **58**, 2733 (1998). 42

[139] M. Bonarota, J. Ruggiero, J.-L. Le Gouët, and T. Chanelière: *Efficiency optimization for atomic frequency comb storage*, Phys. Rev. A **81**, 33803 (2010). 42

[140] E. Pomarico, B. Sanguinetti, C. I. Osorio, H. Herrmann, et al.: *Engineering integrated pure narrow-band photon sources*, New Journal of Physics **14**, 33008 (2012). 47, 105, 137

[141] D. Rieländer, A. Lenhard, M. Mazzera, and H. de Riedmatten: *Cavity enhanced telecom heralded single photons for spin-wave solid state quantum memories*, New Journal of Physics **18**, 123013 (2016). 47, 48, 49, 55, 58, 62, 93

[142] H. Zhang, M. Sabooni, L. Rippe, C. Kim, et al.: *Slow light for deep tissue imaging with ultrasound modulation*, Applied Physics Letters **100**, (2012). 49, 94

[143] S. E. Beavan, E. A. Goldschmidt, and M. J. Sellars: *Demonstration of a dynamic bandpass frequency filter in a rare-earth ion-doped crystal*, J. Opt. Soc. Am. B **30**, 1173 (2013). 49, 94

[144] N. Maring, D. Lago-Rivera, A. Lenhard, G. Heinze, et al.: *Quantum frequency conversion of memory-compatible single photons from 606nm to the telecom C-band*, Optica **5**, 507 (2018). 50

[145] J. Nunn: *A Solid Footing for a Quantum Repeater*, Physics **10**, 55 (2017). 54

[146] B. Lauritzen, J. Minar, H. de Riedmatten, M. Afzelius, et al.: *Telecommunication-Wavelength Solid-State Memory at the Single Photon Level*, Phys. Rev. Lett. **104**, 080502 (2010). 54

[147] R. Riedinger, S. Hong, R. A. Norte, J. A. Slater, et al.: *Non-classical correlations between single photons and phonons from a mechanical oscillator*, Nature **530**, 313 (2016). 54

[148] A. G. Radnaev, Y. O. Dudin, R. Zhao, H. H. Jen, et al.: *A quantum memory with telecom-wavelength conversion*, Nat Phys **6**, 894 (2010). 54

[149] N. Maring, K. Kutluer, J. Cohen, M. Cristiani, et al.: *Storage of up-converted telecom Photon in a doped crystal*, New Journal of Physics **16**, 113021 (2014). 54

[150] R. Ikuta, T. Kobayashi, K. Matsuki, S. Miki, et al.: *Heralded single excitation of atomic ensemble via solid-state-based telecom photon detection*, Optica **3**, 1279 (2016). 54

[151] S. Fasel, O. Alibart, S. Tanzilli, P. Baldi, et al.: *High-quality asynchronous heralded single-photon source at telecom wavelength*, New Journal of Physics **6**, 163 (2004). 62, 93, 107

[152] P. Sekatski, N. Sangouard, N. Gisin, H. de Riedmatten, et al.: *Photon-pair source with controllable delay based on shaped inhomogeneous broadening of rare-earth-metal-doped solids*, Phys. Rev. A **83**, 053840 (2011). 65

[153] P. Jobez, I. Usmani, N. Timoney, C. Laplane, et al.: *Cavity-enhanced storage in an optical spin-wave memory*, New Journal of Physics **16**, 083005 (2014). 68

[154] M. Zhong, M. P. Hedges, R. L. Ahlefeldt, J. G. Bartholomew, et al.: *Optically addressable nuclear spins in a solid with a six-hour coherence time*, Nature **517**, 177 (2015). 68

[155] K. M. Davis, K. Miura, N. Sugimoto, and K. Hirao: *Writing waveguides in glass with a femtosecond laser*, Optics letters **21**, 1729 (1996). 70

[156] G. D. Valle, R. Osellame, and P. Laporta: *Micromachining of photonic devices by femtosecond laser pulses*, Journal of Optics A: Pure and Applied Optics **11**, 013001 (2009). 70

[157] T. Gorelik, M. Will, S. Nolte, A. Tuennermann, et al.: *Transmission electron microscopy studies of femtosecond laser induced modifications in quartz*, Applied Physics A **76**, 309 (2003). 70

[158] R. R. Thomson, S. Campbell, I. J. Blewett, A. K. Kar, et al.: *Optical waveguide fabrication in z-cut lithium niobate ($LiNbO_3$) using femtosecond pulses in the low repetition rate regime*, Applied Physics Letters **88**, 111109 (2006). 70

[159] R. Keil, M. Heinrich, F. Dreisow, T. Pertsch, et al.: *All-optical routing and switching for three-dimensional photonic circuitry*, Scientific reports **1** (2011). 70

[160] J. Liu, Z. Zhang, S. Chang, C. Flueraru, et al.: *Directly writing of 1-to-N optical waveguide power splitters in fused silica glass using a femtosecond laser*, Optics communications **253**, 315 (2005). 70

[161] Y. Liao, J. Xu, Y. Cheng, Z. Zhou, et al.: *Electro-optic integration of embedded electrodes and waveguides in $LiNbO_3$ using a femtosecond laser*, Optics letters **33**, 2281 (2008). 70

[162] R. Osellame, M. Lobino, N. Chiodo, M. Marangoni, et al.: *Femtosecond laser writing of waveguides in periodically poled lithium niobate preserving the nonlinear coefficient*, Applied physics letters **90**, 241107 (2007). 70, 82, 83

[163] J. Burghoff, C. Grebing, S. Nolte, and A. Tünnermann: *Efficient frequency doubling in femtosecond laser-written waveguides in lithium niobate*, Applied physics letters **89**, 81108 (2006). 70

[164] G. D. Marshall, A. Politi, J. C. F. Matthews, P. Dekker, et al.: *Laser written waveguide photonic quantum circuits*, Optics express **17**, 12546 (2009). 70

[165] G. Vest, M. Rau, L. Fuchs, G. Corrielli, et al.: *Design and evaluation of a handheld quantum key distribution sender module*, Selected Topics in Quantum Electronics, IEEE Journal of **21**, 1 (2015). 70

[166] A. Crespi, R. Osellame, R. Ramponi, D. J. Brod, et al.: *Integrated multimode interferometers with arbitrary designs for photonic boson sampling*, Nature Photonics **7**, 545 (2013). 70

[167] M. Tillmann, B. Dakić, R. Heilmann, S. Nolte, et al.: *Experimental boson sampling*, Nature Photonics **7**, 540 (2013). 70

[168] T. Calmano, J. Siebenmorgen, O. Hellmig, K. Petermann, et al.: *Nd: YAG waveguide laser with 1.3 W output power, fabricated by direct femtosecond laser writing*, Applied Physics B **100**, 131 (2010). 71

[169] T. Calmano, J. Siebenmorgen, A.-G. Paschke, C. Fiebig, et al.: *Diode pumped high power operation of a femtosecond laser inscribed Yb: YAG waveguide laser [Invited]*, Optical Materials Express **1**, 428 (2011). 71

[170] Y. Tan, Y. Jia, F. Chen, J. R. de Aldana, et al.: *Simultaneous dual-wavelength lasers at 1064 and 1342 nm in femtosecond-laser-written Nd: YVO_ 4 channel waveguides*, J. Opt. Soc. Am. B **28**, 1607 (2011). 71

[171] S. Müller, T. Calmano, P. Metz, N.-O. Hansen, et al.: *Femtosecond-laser-written diode-pumped Pr: LiYF_ 4 waveguide laser*, Optics letters **37**, 5223 (2012). 71

[172] Y. Sun: *'Rare Earth Materials in Optical Storage and Data Processing Applications' in G Liu and B Jacquir (Eds) 'Spectroscopic Properties of Rare Earths in Optical Materials'*, Springer-Verlag, Berlin Heidelberg (2005). 72

[173] Private discussions with Zachary Cole, director of Scientific Materials. 79, 128

[174] Y. Tan, A. Rodenas, F. Chen, R. R. Thomson, et al.: *70% slope efficiency from an ultrafast laser-written Nd: GdVO 4 channel waveguide laser*, Optics express **18**, 24994 (2010). 82

[175] T. Calmano, J. Siebenmorgen, F. Reichert, M. Fechner, et al.: *Crystalline Pr: SrAl 12 O 19 waveguide laser in the visible spectral region*, Optics letters **36**, 4620 (2011). 82

[176] C. Grivas, C. Corbari, G. Brambilla, and P. G. Lagoudakis: *Tunable, continuous-wave Ti: sapphire channel waveguide lasers written by femtosecond and picosecond laser pulses*, Optics letters **37**, 4630 (2012). 82

[177] T. Calmano and S. Müller: *Crystalline waveguide lasers in the visible and near-infrared spectral range*, IEEE Journal of Selected Topics in Quantum Electronics **21**, 401 (2015). 82

[178] A. Rodenas and A. K. Kar: *High-contrast step-index waveguides in borate nonlinear laser crystals by 3D laser writing*, Optics express **19**, 17820 (2011). 82, 83

[179] L. Li, W. Nie, Z. Li, C. Romero, et al.: *Laser-writing of ring-shaped waveguides in BGO crystal for telecommunication band*, Optics Express **25**, 24236 (2017). 82

[180] J. Burghoff, S. Nolte, and A. Tünnermann: *Origins of waveguiding in femtosecond laser-structured LiNbO3*, Applied Physics A **89**, 127 (2007). 82, 83

[181] R. Thomson, S. Campbell, I. Blewett, A. Kar, et al.: *Optical waveguide fabrication in z-cut lithium niobate (LiNbO 3) using femtosecond pulses in the low repetition rate regime*, Applied Physics Letters **88**, 111109 (2006). 82, 83

[182] L. Huang, P. Salter, M. Karpiński, B. Smith, et al.: *Waveguide fabrication in KDP crystals with femtosecond laser pulses*, Applied Physics A **118**, 831 (2015). 82

[183] A. Rodenas, A. Benayas, J. Macdonald, J. Zhang, et al.: *Direct laser writing of near-IR step-index buried channel waveguides in rare earth doped YAG*, Optics letters **36**, 3395 (2011). 82

[184] J. Macdonald, R. Thomson, S. Beecher, N. Psaila, et al.: *Ultrafast laser inscription of near-infrared waveguides in polycrystalline ZnSe*, Optics letters **35**, 4036 (2010). 82

[185] I. Mansour and F. Caccavale: *An improved procedure to calculate the refractive index profile from the measured near-field intensity*, Journal of Lightwave Technology **14**, 423 (1996). 83

[186] R. G. Hunsperger: *Integrated optics*, vol. 4, Springer (1995). 84, 85

[187] A. V. Durrant, J. Manners, and P. M. Clark: *Understanding optical echoes using Schrodiner's equation: II. Three pulse echoes and collision effects*, Eur. J. Phys. **12**, 234 (1991). 88, 89

[188] R. Yano, M. Mitsunaga, and N. Uesugi: *Stimulated-photon-echo spectroscopy. I. Spectral diffusion in* Eu^{3+} : $YAlO_3$, Phys. Rev. B **45**, 12752 (1992). 90

[189] M. Nilsson and S. Kröll: *Solid state quantum memory using complete absorption and re-emission of photons by tailored and externally controlled inhomogeneous absorption profiles*, Optics Communications **247**, 393 (2005). 92

[190] A. Seri, G. Corrielli, D. Lago-Rivera, A. Lenhard, et al.: *Supplementary content for the paper "Laser-written integrated platform for quantum storage of heralded single photons"*, Optica **5**, 934 (2018). 93

[191] C. W. Chou, S. V. Polyakov, A. Kuzmich, and H. J. Kimble: *Single-Photon Generation from Stored Excitation in an Atomic Ensemble*, Phys. Rev. Lett. **92**, 213601 (2004). 94

[192] P. Jobez, C. Laplane, N. Timoney, N. Gisin, et al.: *Coherent Spin Control at the Quantum Level in an Ensemble-Based Optical Memory*, Phys. Rev. Lett. **114**, 230502 (2015). 98

[193] M. Valentini: *Spin rephasing techniques for long-lived solid-state quantum memories*, Master's thesis (2018). 98

[194] G. D. Marshall, P. Dekker, M. Ams, J. A. Piper, et al.: *Directly written monolithic waveguide laser incorporating a distributed feedback waveguide-Bragg grating*, Optics Letters **33**, 956 (2008). 102

[195] S. Atzeni, A. S. Rab, G. Corrielli, E. Polino, et al.: *Integrated sources of entangled photons at the telecom wavelength in femtosecond-laser-written circuits*, Optica **5**, 311 (2018). 102

[196] D. Rieländer, A. Lenhard, O. J. Farìas, A. Máttar, et al.: *Frequency-bin entanglement of ultra-narrow band non-degenerate photon pairs*, Quantum Science and Technology **3**, 014007 (2017). 104, 114, 120

[197] L. Olislager, J. Cussey, A. T. Nguyen, P. Emplit, et al.: *Frequency-bin entangled photons*, Phys. Rev. A **82**, 013804 (2010). 104

[198] J. M. Lukens and P. Lougovski: *Frequency-encoded photonic qubits for scalable quantum information processing*, Optica **4**, 8 (2017). 104

[199] M. Kues, C. Reimer, P. Roztocki, L. R. Cortés, et al.: *On-chip generation of high-dimensional entangled quantum states and their coherent control*, Nature **546**, 622 (2017). 104

[200] H.-H. Lu, J. M. Lukens, N. A. Peters, B. P. Williams, et al.: *Quantum interference and correlation control of frequency-bin qubits*, Optica **5**, 1455 (2018). 104

[201] M. Grimau Puigibert, G. H. Aguilar, Q. Zhou, F. Marsili, et al.: *Heralded Single Photons Based on Spectral Multiplexing and Feed-Forward Control*, Phys. Rev. Lett. **119**, 083601 (2017). 114

[202] D. M. S. Johnson, J. M. Hogan, S. w. Chiow, and M. A. Kasevich: *Broadband optical serrodyne frequency shifting*, Opt. Lett. **35**, 745 (2010). 115

[203] A. Crespi, R. Osellame, R. Ramponi, M. Bentivegna, et al.: *Suppression law of quantum states in a 3D photonic fast Fourier transform chip*, Nature Communications **7**, 10469 (2016). 115, 119

[204] Y. Chen, J. Gao, Z.-Q. Jiao, K. Sun, et al.: *Mapping Twisted Light into and out of a Photonic Chip*, Phys. Rev. Lett. **121**, 233602 (2018). 115, 152

[205] F. Dell'Anno, S. De Siena, and F. Illuminati: *Multiphoton quantum optics and quantum state engineering*, Physics reports **428**, 53 (2006). 120

[206] M. A. Nielsen: *Cluster-state quantum computation*, Reports on Mathematical Physics **57**, 147 (2006). 120

[207] C. Abellán, A. Acín, A. Alarcón, O. Alibart, et al.: *Challenging local realism with human choices*, Nature **557**, 212 (2018). 120

[208] L. Rippe, M. Nilsson, S. Kroll, R. Klieber, et al.: *Experimental demonstration of efficient and selective population transfer and qubit distillation in a rare-earth-metal-ion-doped crystal*, Phys. Rev. A **71**, 62312 (2005). 123

[209] J. Minář, N. Sangouard, M. Afzelius, H. de Riedmatten, et al.: *Spin-wave storage using chirped control fields in atomic frequency comb-based quantum memory*, Phys. Rev. A **82**, 042309 (2010). 123

[210] S. Richter, S. Döring, F. Burmeister, F. Zimmermann, et al.: *Formation of periodic disruptions induced by heat accumulation of femtosecond laser pulses*, Optics express **21**, 15452 (2013). 127